# DEVELOPMENT OF ORGANIC THERMOELECTRIC MATERIALS AND DEVICES FOR ENERGY HARVESTING

A Dissertation
Presented to
The Academic Faculty

by

Akanksha Krishnakumar Menon

In Partial Fulfillment
of the Requirements for the Degree
of Doctor of Philosophy in the
George W. Woodruff School of Mechanical Engineering

Georgia Institute of Technology
May 2018

# DEVELOPMENT OF ORGANIC THERMOELECTRIC MATERIALS AND DEVICES FOR ENERGY HARVESTING

Approved by:


Dr. Shannon Yee, Advisor
George W. Woodruff School of Mechanical Engineering
*Georgia Institute of Technology*

Dr. John Reynolds
School of Chemistry & Biochemistry
*Georgia Institute of Technology*

Dr. Samuel Graham
George W. Woodruff School of Mechanical Engineering
*Georgia Institute of Technology*

Dr. Bernard Kippelen
School of Electrical and Computer Engineering
*Georgia Institute of Technology*

Dr. Asegun Henry
George W. Woodruff School of Mechanical Engineering
*Georgia Institute of Technology*


Date Approved: March 26, 2018

To my family, advisor and friends

# ACKNOWLEDGEMENTS

I am very grateful to my research advisor, Prof. Shannon Yee, for accepting me as his first graduate student and radiating an infectious enthusiasm for science. I am glad that he convinced me to stay on for the PhD and challenged me in a way that helped me grow professionally. Beyond research, he encouraged me to get involved with the Energy Club @ Georgia Tech, ARPA-E and C3E; these extra-curricular experiences were pivotal in making me well-rounded. I am also thankful for Shannon's incredible academic network that served me well as I interviewed for postdoc positions, and for the opportunity to present my work at prestigious conferences, in Japan and Spain, no less.

Next, I would like to thank my thesis committee for providing valuable feedback on my work. Specifically, I would like to thank Dr. John Reynolds for his patience with a mechanical engineer trying to learn chemistry, Dr. Samuel Graham and Dr. Asegun Henry for the tough research questions and invaluable career advice, and to Dr. Bernard Kippelen for a memorable class on organic electronics that gave me the opportunity to develop and deliver lectures. Apart from my committee, I want to acknowledge Dr. Seth Marder and Dr. Jeff Roberts for their mentorship and career advice, and Dr. Nesrin Ozalp for serving as my undergraduate advisor and exposing me to the world of research.

I want to thank my fellow graduate students in Yeelab, with whom I've experienced the love-hate relationship that is grad school. I am grateful to Sampath Kommandur and Misha Rodin for sharing long work weeks as we built our lab from scratch (and for the conversations over pizza and beer at Rocky's that followed), and for the numerous gold depositions in the cleanroom over the years. I also want to thank Rylan Wolfe as I couldn't

have asked for a better organic chemist to work with, and my other lab mates Alex Limia, Aravindh Rajan, Patrick Creamer, Jong Ha and Shawn Gregory for all the friendly banter and endless hours of conversations on life. I'm reluctant about admitting that we've gone from being colleagues to friends, even though our social coordinator was not very competent! Thanks are also due to the to the other graduate students and scientists that I've worked with, especially Kiarash Gordiz, Erdal Uzunlar, James Ponder, Carolyn Buckley, Thomas Bougher, Hend Elmoughni, Andrey Gunawan, Simon King and Thomas Fletcher. I also want to acknowledge my undergrads, (Arnold Eng, Olivia Meek and Jade Marcus) and my high school interns from GSMST (Ju Kim, Kyra Solomon, Karthik Yadavalli); I've enjoyed the privilege of mentoring them and seeing them embark on their scientific careers.

Next, I gratefully acknowledge the Qatar Foundation for my graduate school funding, as well as Georgia Tech's Center for the Science and Technology of Advanced Materials and Interfaces (STAMI) and the Center for Teaching and Learning (CTL) for additional fellowships. I also want to thank VentureLab for their innovation competition travel grants, and especially acknowledge Jon Goldman and Paul Freet for piquing my interest in entrepreneurship and letting me dabble in customer discovery.

Most importantly, I want to thank my parents, Kumar and Shobhana for their unwavering love and support over the past five years, and my brother, Atul. They always encouraged me to dream big and to pursue what I wanted without letting me worry about anything else. I also want to thank my Uncle, Dr. Rajesh Bhaskaran for introducing the realities of climate change that inspired me to pursue a career in science. I am also ever grateful to my friends in Atlanta for helping me offset crazy work weeks with relaxing weekends – thank you for making this place feel like home.

# TABLE OF CONTENTS

# LIST OF TABLES

# LIST OF FIGURES

# LIST OF SYMBOLS AND ABBREVIATIONS

| | |
|---|---|
| $A$ | Total plate area |
| $A_{HX,H}$ | Hot-side heat exchanger area |
| $A_{TE}$ | Total thermoelectric material area |
| $E_F$ | Fermi level or chemical potential |
| $F$ | Fill factor |
| $f_0$ | Equilibrium Fermi-Dirac distribution |
| $g$ | Electronic density of states |
| $h$ | Convective heat transfer coefficient |
| $I$ | Electrical current |
| $k$ | Thermal conductivity |
| $k_B$ | Boltzmann's constant |
| $K_C$ | Thermal conductance of cold-side heat exchanger |
| $K_H$ | Thermal conductance of hot-side heat exchanger |
| $K_T$ | Total thermal conductance |
| $K_{TE}$ | Thermal conductance of thermoelectric legs |
| $K_{\|\|}$ | Thermal conductance of parallel path |
| $L$ | Thermoelectric leg length |
| $L_T$ | Characteristic thermal length, ratio of $h/k$ |
| $L_{cr}$ | Leg length for maximum heat flux |
| $L_{match}$ | Leg length for thermal impedance matching |
| $L_{opt}$ | Leg length for maximum power |
| $m$ | Ratio of load resistance to device resistance |

| | |
|---|---|
| $M$ x $N$ | $M$ sub-modules in parallel, each with $N$ legs in series |
| $n$ | Carrier concentration |
| $p$ | Order of the Hilbert curve |
| $P$ | Electric power output of TEG |
| $Q_C$ | Heat transferred though cold-side heat exchanger |
| $Q_H$ | Heat transferred though hot-side heat exchanger |
| $Q_{\|\|}$ | Heat transferred though substrate |
| $Q_{TE}$ | Heat transferred though thermoelectric legs |
| $r_{in}$ | Inner radius of radial thermoelectric device |
| $r_{out}$ | Outer radius of radial thermoelectric device |
| $R$ | Electrical resistance |
| $R_L$ | Electrical load resistance |
| $R_T$ | Total electrical resistance |
| $R_{TE}$ | Electrical resistance of thermoelectric legs |
| $S$ | Seebeck coefficient |
| $S_{p\text{-}n}$ | Difference in Seebeck coefficients of p- and n-type legs |
| $t$ | Thickness of thermoelectric legs |
| $t_{sub}$ | Thickness of substrate |
| $T$ | Temperature |
| $T_C$ | Cold-side temperature |
| $T_H$ | Hot-side temperature |
| $T_m$ | Mean junction temperature |
| $T_1$ | Hot junction temperature |
| $T_2$ | Cold junction temperature |
| $\Delta T$ | Junction temperature difference |

| | |
|---|---|
| $v$ | Charge carrier velocity |
| $zT$ | Material figure-of-merit |
| $ZT$ | Module figure-of-merit |
| $\eta$ | Efficiency |
| $\sigma$ | Electrical conductivity |
| $\mu$ | Charge carrier mobility |
| $\tau$ | Scattering time |
| TEG | Thermoelectric generator |
| ETT | Ethenetetrathiolate polymer |
| NNH | Nearest neighbor hopping |
| VRH | Variable range hopping |
| TGA-MS | Thermogravimetric analysis with tandem mass spectrometry |
| XPS | X-ray photoelectron spectroscopy |
| PP | Pristine powder of ETT |
| AP | Annealed powder of ETT |
| PF | Pristine film of ETT/PVDF |
| AF | Annealed film of ETT/PVDF |
| TTO | Tetrathiooxalate polymer |

# SUMMARY

There is an abundance of heat that is rejected to the environment owing to efficiency limitations of existing heat engines. Thermoelectric generators, comprising p- and n-type semiconductors, can recover this waste heat and convert it directly into electricity. Given that over 60% of available waste heat is at temperatures below 250 °C, low cost and large scale thermoelectric devices are required to economically capture the heat. In this regard, conducting polymers constitute a suitable class of materials for low grade thermal energy harvesting as they can be synthesized from abundant elements and can be processed from solution using low cost fabrication techniques. Furthermore, their low thermal conductivity and flexible nature enable new device architectures and applications.

Despite these advantages, polymer-based thermoelectric devices have not made an impact. This is largely attributed to two factors: *(i)* the lack of high performance n-type polymers (power factor > 10 μW/m-K$^2$), and *(ii)* low power outputs (nW - μW) owing to impractical device design. In the past decade, significant progress has been made with p-type materials, but n-type polymers have lagged behind due to their propensity to react in air. To address this, I have investigated metallo-organic polymers as a suitable class of n-type polymers that are electrically conducting and maintain their stability in air. This is one focus of my dissertation that discusses the synthesis, characterization and thermoelectric properties of n-type poly(nickel-ethenetetrathiolate) or NiETT. By modifying the reaction conditions and film post-treatment by annealing, the thermoelectric properties can be enhanced to obtain a high performing n-type polymer that is air stable. As a parallel effort

to developing materials, there is a need for new device designs that leverage the benefits of conducting polymers, *i.e.*, their low thermal conductivity and solution processability. This is the other focus of my dissertation, which is the development of two new device architectures tailored for polymers. The first is a radial design based on characteristic thermal length scales for polymers that enables a 10x improvement in power density compared to conventional flat plate devices. This architecture uses heat spreading that eliminates the need for active cooling, while also reducing electrical contact resistance thereby enabling higher power densities. The second design is a close-packed layout for printing high fill factor devices. By using fractal space-filling curves as interconnect patterns, the thermoelectric device can be tessellated into sub-modules for load matching to a variety of applications, thus eliminating the need for power convertors for wearable electronics.

Overall, this dissertation marks the progress in developing an n-type polymer and printable composite with a power factor larger than 10 $\mu W/m\text{-}K^2$ that is stable in ambient conditions, as well as two new device designs tailored to polymers for applications such as waste heat recovery from pipes using a radial architecture, and body heat harvesting using high fill factor devices with fractal interconnect patterns.

# CHAPTER 1. INTRODUCTION TO THERMOELECTRICS

Thermoelectric generators (TEG) are solid-state devices that convert heat directly into electricity.[1,2] These devices consist of p- and n-type semiconductors (referred to as thermoelectric legs) connected electrically in series and thermally in parallel, sandwiched between a heat source and heat sink. Under an applied temperature difference, charge carriers in these semiconductors diffuse from the hot to the cold side to generate a voltage in accordance with the Seebeck effect (see Figure 1). These devices can also be operated in reverse where electricity is supplied to provide heating or cooling via the Peltier effect. Thermoelectric (TE) devices are attractive because they have no moving parts and are projected to have long lifetimes. Despite these advantages, the technology has been limited to niche applications in satellites,[3] car seat heaters, small-scale refrigeration,[1] and in solar applications.[4,5] However, there is unexplored potential for this technology given that waste heat is abundant; over 60% of this heat is at temperatures lower than 250 $^{0}$C and cannot be cost-effectively utilized in traditional heat engines.[6]

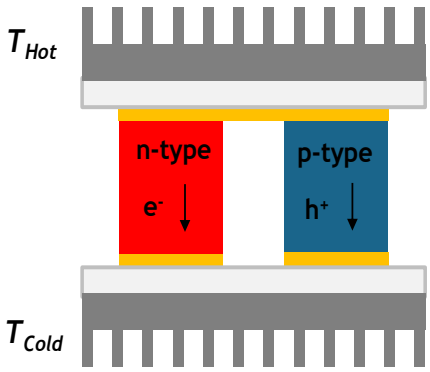


**Figure 1 – Schematic of a conventional flat-plate thermoelectric device consisting of a p-n leg pair sandwiched between heat exchangers. In the presence of a temperature difference ($\Delta T = T_{Hot} - T_{Cold}$), charge carriers ($e^-$ for electrons and $h^+$ for holes) diffuse through the device and create a voltage.**

## 1.1 Fundamentals of Thermoelectric Materials

The energy conversion efficiency of a thermoelectric material depends on its electrical and thermal transport properties. Specifically, it should be a good electrical conductor to transport charge carriers effectively, and a good thermal insulator to maintain a large temperature difference between the hot and cold side, resulting in a class of materials called phonon-glass, electron-crystal.[7-10] This is governed by three transport properties: $S$ is the Seebeck coefficient or thermopower (μV/K), $\sigma$ is the electrical conductivity (S/cm), $k$ is the thermal conductivity (W/m-K), and $T$ is the absolute temperature (K). Together, these properties form the dimensionless material figure-of-merit, $zT = S^2\sigma T/k$, where the numerator $S^2\sigma$ is commonly referred to as the power factor (μW/m-K$^2$). The electrical conductivity results from the distribution and mobility of electrons in the material, the Seebeck coefficient results from the asymmetry in the distribution of electrons around the Fermi level or chemical potential, and the thermal conductivity results from the distribution and mobility of electrons and phonons in the material. The sign of the Seebeck coefficient is indicative of the dominant charge carrier, *i.e.,* electron transport in n-type materials yields a negative $S$ and hole transport in p-type materials results in a positive $S$.

To improve thermoelectric performance, the electrical conductivity can be enhanced by increasing the carrier concentration, $n$, via doping. This is commonly described using the Drude model for an electron gas: $\sigma = ne\mu$, where $e$ is the elementary charge and $\mu$ is the charge mobility. However, doping is accompanied by a decrease in the Seebeck coefficient (this will be explained in the following section) and an increase in the thermal conductivity. This is because the thermal conductivity is comprised of a

contribution from both electrons ($k_e$) and phonons or the lattice ($k_L$). The electronic contribution is related to the electrical conductivity through the Wiedemann-Franz law: $k_e = \sigma LT$, where $L$ is the Lorenz number. Upon increasing the carrier concentration, $k_e$ increases as $\sigma$ increases, and this results in an enhancement of the overall thermal conductivity. This inherent coupling between the thermoelectric properties is illustrated in Figure 2 and results in an optimum carrier concentration that maximizes $zT$. This optimum occurs at carrier concentrations between $10^{19}$ and $10^{21}$ per $cm^3$, thereby making heavily doped semiconductors the preferred class of thermoelectric materials.[8]

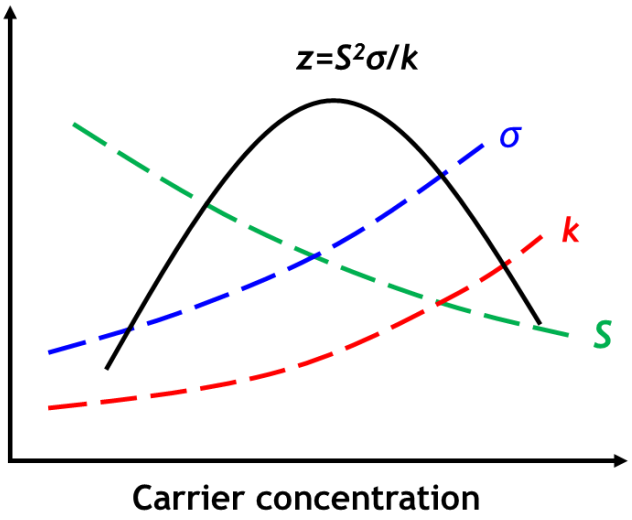


**Figure 2 – Thermoelectric properties are anti-correlated and show competing trends with doping. Increasing the carrier concentration results in an increase in electrical conductivity accompanied by a reduction in the Seebeck coefficient. Thermal conductivity increases with carrier concentration as electrons transport heat in addition to charge.**

Thermoelectric conversion has been studied since the 1950s with the discovery of $Bi_2Te_3$ which can be doped to obtain high power factors ~4000 μW/m-$K^2$ while maintaining a thermal conductivity of ~1.2 W/m-K, yielding a $ZT$ of ~1 at room temperature. This translates into a conversion efficiency ~5% for a $\Delta T$=100K and $T_C$ =300 K. This low

efficiency limits the widespread adoption of this material and thermoelectric technology have been relegated to niche applications. Over the past two decades, thermoelectric conversion has garnered renewed scientific interest owing to thermal conductivity reduction via nanostructuring. These nanostructures have characteristic lengths that scatter phonons without affecting the electronic transport given the large mismatch in mean free paths. These strategies reduce the phononic contribution to thermal conductivity without scattering electrons that would reduce the electrical conductivity.[2,11] Notable advancements in thermoelectric materials include a $zT$ of 2.2 for PbTe at 900 K via nanostructuring, and a $zT$ of 2.6 at 923 K for SnSe single crystals along a specific crystal plane.[11,12]

## 1.2 Charge Transport in Inorganic Semiconductors

Conventional thermoelectric materials are inorganic semiconductors, and charge conduction is well-described by band-like transport derived from the Boltzmann transport theory. In these systems, the electrical conductivity is expressed as:

$$\sigma_B = -\frac{e^2}{3}\int \tau v^2 g \frac{\partial f_0}{\partial E} dE = -\frac{e^2}{3}\int \sigma(E) dE \tag{1}$$

where $v$ is the carrier velocity, $\tau$ is the scattering time, $g$ is the electronic density of states and $f_0$ is the equilibrium Fermi-Dirac distribution. The energy dependent parameters can be grouped into one term called the differential electrical conductivity, $\sigma(E)$. This term is also present in the expression for the Seebeck coefficient:

$$S_B = -\frac{1}{eT}\frac{\int \tau v^2 g\left(E - E_F\right)\frac{\partial f_0}{\partial E}dE}{\int \tau v^2 g \frac{\partial f_0}{\partial E}dE} = -\frac{1}{eT}\frac{\int \sigma(E)\left(E - E_F\right)dE}{\sigma} \quad (2)$$

where $E_F$ is the Fermi level or chemical potential that can be tuned via doping. This expression provides a physical interpretation of the Seebeck coefficient, *i.e.*, it is a measure of the asymmetry in the distribution of electrons with energy greater than $E_F$ (hot electrons) and those with lower energy (cold electrons). The expression also shows the inverse relationship between $S$ and $\sigma$, and this coupling makes it challenging to obtain high power factors in most thermoelectric materials. $S$ can be enhanced by moving the Fermi level far from the conduction band to increase asymmetry, however this results in a decrease in $\sigma$ as fewer carriers are available for transport. This also explains why metals have a low thermopower and high electrical conductivity while insulators have a high thermopower and low conductivity, thereby making doped semiconductors an ideal class of thermoelectric materials.

Strategies to decouple $S$ and $\sigma$ have been investigated in inorganic semiconductors, and these typically exploit different scattering mechanisms.[10,13] One such approach relies on energy-dependent scattering using interfaces that selectively scatters cold electrons while allowing hot electrons to pass through. This is referred to as energy filtering and increases the asymmetry about the chemical potential to yield a high $S$ without a significant reduction in $\sigma$. Another approach is the reduction of energy-independent scattering such as boundary or impurity scattering that results in a high $\sigma$ without affecting $S$. These energy-independent scattering events are captured in the mobility and can be tuned by controlling

the material microstructure without impacting the thermopower. Thus, the main strategy for developing high performance thermoelectric materials is by doping inorganic semiconductors to obtain high power factors, which when coupled with reductions in the lattice thermal conductivity through nanostructuring has resulted in significant advances in material properties over the last 20 years. While this is promising for high temperature applications, most of these materials exhibit a $zT$ below 0.1 at room temperature,[4] and the large material and manufacturing cost render them unsuitable for low grade waste heat recovery applications.

## 1.3 Towards Organic Thermoelectrics

An alternate approach to thermoelectric materials design is to start with a low thermal conductivity system and optimize the power factor. In this regard, organic materials constitute a largely underexplored class of thermoelectric materials for low grade heat recovery. In addition to being potentially abundant, these materials have significant advantages over their inorganic counterparts such as being low cost, lightweight, and poor thermal conductors. The latter is due to their disordered and amorphous nature, which results in a significant reduction in the thermal conductivity (one order of magnitude lower than $Bi_2Te_3$), which is beneficial for thermoelectric applications. Polymers are unique because the inherent tunability in their structure and processing can enable thermoelectric property optimization that is not achievable with traditional inorganic semiconductors. Furthermore, these materials can be synthesized and processed from solution that enables new manufacturing techniques (such as printing) with high throughput and at a low cost. The film forming nature of organic materials also affords new application spaces such as flexible and wearable electronics.

### *1.3.1 Conducting Polymers*

Conjugated polymers constitute a special class of organic materials comprising $sp^2$-hybridized carbon atoms with delocalized π-orbitals that participate in charge transport. Contrary to typical polymers that are insulators, these materials have alternating single and double bonds that result in small band gaps (1-3 eV) and renders them conducting. A conjugated polymer chain typically has numerous repeating units or monomers, and the polymer is made soluble by introducing side-chain substituents (typically linear or branched alkyl groups). These materials have been extensively studied for organic transistors (OFET) and photovoltaics (OPV), and their thermoelectric performance has been heavily investigated over the last 5 years.[14] Conjugated polymers for thermoelectric applications require higher electrical conductivities than those designed for OPV or OFET applications. As a result, doping is frequently used to increase the charge carrier concentration. It is important to clarify here that doping conducting polymers is significantly different from inorganics, and the main difference lies in the doping level; inorganic semiconductors are doped on the order of <1% while polymers are doped to a much larger extent (~35%) by weight.

Polymer doping typically occurs via a redox reaction between the polymer and dopant. For p-doping, this is done by exposing the polymer to a gas or by dipping in a solution containing an oxidizing agent. The reduced dopant transforms into a negative counterion (iodine $I_2$ becomes $I_3^-$) that neutralizes the positive charge on the polymer backbone.[36] Alternately, conducting polymers can directly be synthesized in their oxidized form by chemical polymerization.[40] In this case, the oxidation level is tuned during the chemical reaction using a reducing agent to obtain a p-doped polymer.[41] Furthermore, there

are strategies such as secondary doping where thermoelectric properties can be simultaneously improved via morphological changes;[14-18] this provides an additional level of tuning that is not available to inorganic materials. Conducting polymers such as polyaniline (PANI), poly(3,4-ethylenedioxythiophene): poly(styrenesulfonate) and :tosylate (PEDOT:PSS and PEDOT-Tos), polyacetylene (PA), as well as derivatives of polypyrrole (PPY), and polyphenylenevinylene (PPV) have shown promise as thermoelectric materials.[16] Among these, the best performing materials are PEDOT:Tos[18] with a $zT$ of 0.25 and DMSO-doped PEDOT:PSS[19] with a $zT$ of 0.42 which makes them comparable to some inorganic materials near room temperature. However, these are p-type and progress in n-type polymers has been much slower owing to limited n-dopants and the propensity of doped polymers to degrade in air. Figure 3 shows improvements in thermoelectric performance of organic materials over the past decade.[18,20-25]

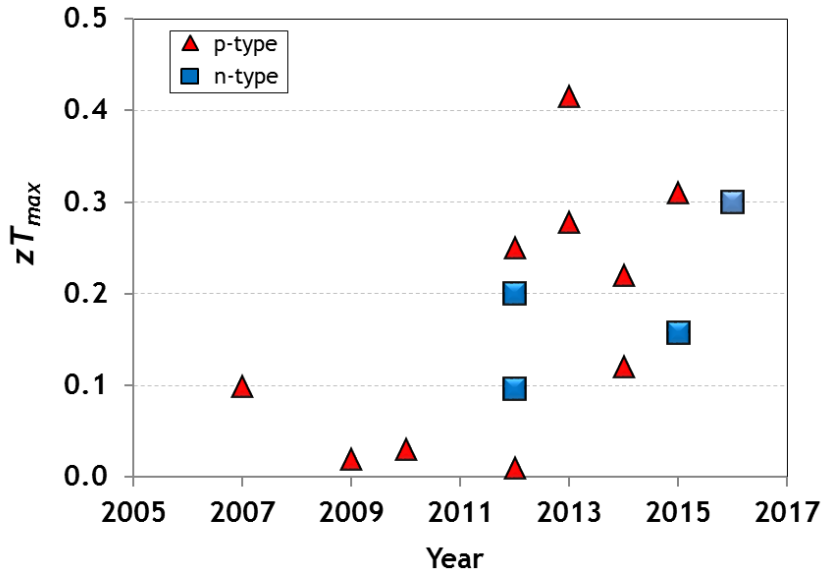


**Figure 3 – Thermoelectric figure-of-merit for organic materials reported in literature. Rapid progress has been made in p-type materials but high performing n-type polymers have lagged behind.**

The best performing n-type materials are based on coordination polymers or metallo-organic polymers that consist of a central metal atom coordinated with an organic ligand. This material system offers significant tunability that warrants further investigation; this is the focus of the dissertation and will be discussed in subsequent chapters.

### *1.3.2 Charge Transport in Organic Semiconductors*

Conducting polymers have both energetic and spatial disorder that causes the localization of charge carriers. The presence of these localized states precludes the application of the free-electron approximation that describes electronic transport in inorganic semiconductors. This is because the disordered nature of polymers makes it challenging to clearly define a free-carrier concentration and mobility, thus requiring a different transport framework. In this case, transport models for disordered systems such as Mott's mobility-edge model for amorphous Silicon and other inorganic alloys are more applicable.[26,27] However, most conducting polymers are heterogeneous owing to the presence of crystalline domains connected by amorphous chains, and this is a key difference from amorphous inorganic materials.[28]

Due to the structural complexity of polymers, thermoelectric properties are described using a myriad of transport models with specific assumptions that limit their applicability to certain transport regimes. Hopping transport has been extensively used to describe charge transport in conducting polymers. This is characterized by an activation which represents the amount of energy required to overcome the energetic or spatial barrier and hop from one localized site to another. Thermal fluctuations can provide this activation

energy, and hence transport in polymers is well-explained by thermally-activated hopping conduction.[26,29-34]

Nearest neighbor hopping (NNH) describes a transport regime in which the hopping rate is limited by spatial tunneling distances such that carriers perform a nearest neighbor hop. This is the case for lightly doped polymers and manifests as an Arrhenius dependence of conductivity on temperature.[32,35] However, at some point the nearest available site might be much higher in energy, that it is more likely for the carrier to perform a hop to a site farther away that has a similar energy. These hops are described by variable range hopping (VRH), where carriers choose a distant site over the nearest neighbor to address the large mismatch in energies; this is the case for highly doped polymers.[26,36] Figure 4 illustrates hopping transport in disordered systems and the resulting temperature dependence on thermoelectric properties.

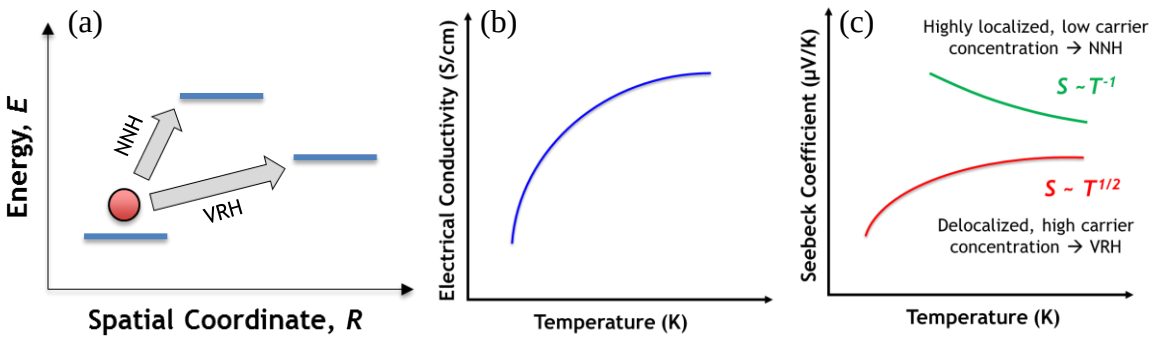


**Figure 4 – Description of hopping transport in polymers. (a) Energetic and spatial disorder results in different hopping regimes - NNH and VRH. (b) Electrical conductivity is thermally activated and increases with temperature for semi-conducting polymers. (c) Seebeck coefficient shows different temperature profiles that are indicative of the degree of disorder in polymers.**

For VRH, the electrical conductivity and thermopower are expressed as:

$$\sigma_{VRH} = \sigma_0 \exp\left(-\frac{T_0}{T}\right)^{1/(\gamma+1)} \tag{3}$$

$$S_{VRH} = \frac{k_B^2}{2e}\left(T_0 T\right)^{1/2} \left.\frac{d\ln(g)}{dE}\right|_{E=E_F} \tag{4}$$

where $\sigma_0$ is the conductivity pre-factor (this is not a function of temperature and depends on scattering), $T_0$ is the characteristic temperature (which is inversely related to the hopping range), and $\gamma$ is the hopping exponent (which depends on the dimensionality of the system, $\gamma$ = 0.5 for a 2D system and 0.25 for a 3D system).[26] At the microscopic scale, transport of carriers in organic materials is related to the electronic coupling between different chains, and at the macroscopic level, transport is dominated by the ability of these carriers to cross domain boundaries. This is well-described within the framework of percolation theory and can be applied to VRH where it manifests as the dimensionality of the system, $\gamma$.[37]

The expressions for hopping conductivity and thermopower are inversely correlated through $T_0$, which can be expressed in terms of the activation energy: $E_A = k_B T_0$. If a carrier can hop farther, *i.e.*, the activation energy is small for a long-range hop (the energy landscape can be tuned via doping), the electrical conductivity increases and is accompanied by a decrease in the Seebeck coefficient. Hence, the same $S$-$\sigma$ coupling that exists in inorganic thermoelectric materials is also prevalent in hopping transport that describes doped polymers. Similar strategies as those discussed in Section 1.2 can be employed to decouple $S$ and $\sigma$ – tuning the morphology of polymers allows for reducing energy independent scattering events that increase conductivity without impacting the

thermopower (only $\sigma_0$ is increased). Another approach is the synthesis of organic-inorganic hybrid materials that can be carefully tuned to invoke energy filtering.[15,38,39]

## 1.4 Thermoelectric Measurements on Thin Films

Given the structural complexity of organic materials and the variability with processing and film fabrication techniques, the measured thermoelectric properties are sample-dependent, and require robust measurements to capture repeatable data. Furthermore, since the thermal conductivity of polymers is low (~0.2 W/m-K), the power factor ($S^2\sigma$) is widely used to compare different materials in literature. Details on thermal conductivity measurements using 3ω, time domain thermoreflectance (TDTR) and frequency domain thermoreflectance (FDTR) are reported elsewhere.[40-47]

Electrical conductivity of thin films is measured using the standard four-probe technique based on the Van der Pauw method.[48] Four probes are placed around the periphery of the sample such that two contact pads are used to source a current, $I$ while the voltage, $V$ is measured across the other two pads. The resistance is obtained as $R = V/I$; this is done in eight configurations (two horizontal and two vertical, followed by reversing the direction of current and obtaining four more $R$ values) and appropriately averaged before solving the Van der Pauw equation for sheet resistance, $R_s$. Once the film thickness, $t$ is known (typically measured using profilometry), the in-plane electrical conductivity can be obtained as $\sigma = 1/R_s t$ for these thin-films.[49]

In order to measure the in-plane Seebeck coefficient of a thin film, the same sample used for electrical conductivity measurements can be used. The Seebeck coefficient is a measure of the voltage induced in response to a temperature gradient. For this, Peltier units

connected to temperature controllers apply a temperature gradient, $\Delta T$ across the sample and the induced voltage, $\Delta T$ is measured across two contact pads.[49] By plotting the measured voltage against the applied temperature gradient, the Seebeck coefficient is obtained as the slope of the curve, $S = -\Delta V/\Delta T$. Figure 5 shows a schematic of the in-plane electrical conductivity and thermopower measurements used for thin films.

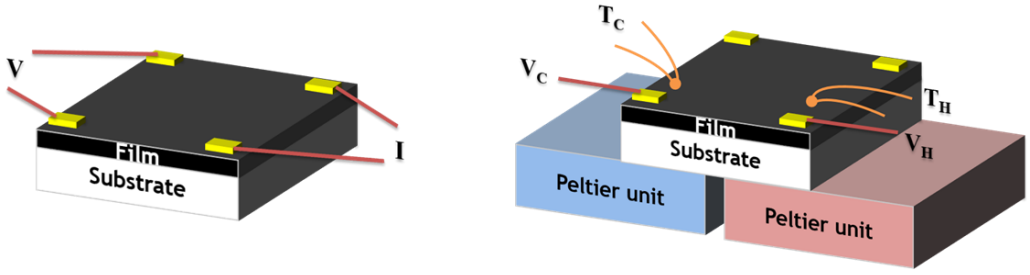


**Figure 5 – Thin film thermoelectric measurement setup. (a) The Van der Pauw technique is used to measure in-plane electrical conductivity by sourcing a current and measuring a voltage across adjacent contact pads. (b) In-plane thermopower measurements are based on the suspended Seebeck technique. Thermocouples in close proximity to voltage probes measure the temperature and induced voltage.**

## 1.5 Dissertation Outline

This dissertation consists of five chapters following this introduction, and the objectives are two-fold: the first goal is to develop n-type polymers with positively correlated transport properties that break the limitations of inorganic thermoelectrics. The second thrust is to design new device architectures tailored for polymers that leverages their lower thermal conductivity and solution processability. While $zT$ and efficiency are important, for energy harvesting, power density is the defining metric since heat is abundant and often free. A summary of the chapters is provided here: this **first chapter** provided motivation and background on thermoelectrics, as well as an understanding of the material properties and charge transport theories. It also emphasized the need to look

beyond existing materials that show the $S$-$\sigma$ tradeoff with doping, specifically in n-type polymers. The **second chapter** introduces metallo-organic polymers as viable n-type materials that do not require extrinsic doping. This chapter discusses modifications to the synthesis of Poly(Ni-ethenetetrathiolate) or NiETT, which enables an enhancement in the electrical conductivity without impacting the thermopower. The **third chapter** is devoted to addressing challenges with the reproducibility of air-oxidized NiETTs by using a chemical oxidant, as well as systematically tuning the properties by optimizing the reaction conditions. By performing post-treatment of films, the thermoelectric properties are simultaneously enhanced. This shows that the $S$ and $\sigma$ can be decoupled in these metallo-organic polymers, making them a class of materials worth investigating for organic thermoelectrics. The development of these air stable and high performing n-type materials motivates the **fourth chapter**. In this chapter, the basics of module design and thermoelectric device physics are introduced, and a new device based on a radial architecture is presented. This leverages the inherent advantages of polymers, namely the low thermal conductivity and solution processability, by redesigning the leg length and fill factor. The **fifth chapter** extends this device-level framework to designs for wearable thermoelectrics. In particular, a close-packed layout is discussed that maximizes fill factor, and a new interconnect pattern based on the Hilbert curve is presented. These concepts are demonstrated with prototype devices for waste heat recovery from pipes, and for wearable electronics or body heat harvesting. Overall, these improvements in material properties and device performance culminate in low cost and large-scale thermoelectric applications for energy harvesting, and **chapter 6** summarizes my research contributions in this field.

# CHAPTER 2. METALLO-ORGANIC POLYMERS AS N-TYPE THERMOELECTRICS

A practical organic thermoelectric device requires both a p-type and an n-type material with reasonably large power factors. Although the performance of p-type organic materials is progressing rapidly,[14,16-19] their n-type counterparts have not benefitted from the same level of development. This is largely due to challenges with performing n-doping that is resistant to oxygen and moisture as most organic semiconductors have small electron affinities (3 - 4 eV). Some of the highest performing n-type polymers reported thus far include metallo-organic poly(Ni-ethenetetrathiolate) (NiETT),[23,50] cobaltocene encapsulated carbon nanotubes[51] and vapor-doped fullerenes.[52-54] However, these materials are processed by pressing powders into pellets, filter-cake collection, and sublimation which makes it difficult to employ large-area manufacturing methods.

Some effort has been made towards developing solution processable n-type materials such as poly[N,N′-bis(2-octyl-dodecyl)-1,4,5,8-napthalenedicarboximide-2,6-diyl]-alt-5,5′-(2,2′-bithiophene)] (P(NDIOD-T2) doped with dihydro-1H-benzoimidazol-2-yl (N-DBI) derivatives,[55] and self-doped perylene diimides (PDI).[56] However, the power factor values for these materials is ~ 1 μW/m-K$^2$, which is at least an order-of-magnitude lower than p-type materials. Recently, Shi *et al.* reported a high conductivity of 14 S/cm for a solution processed n-type material[57] by modifying the backbone of BDPPV doped with (4-(1,3-dimethyl-2,3-dihydro-1*H*-benzoimidazol-2-yl)phenyl)dimethylamine (N-DMBI), and the same group has also demonstrated promising n-type small molecules[58-60]

that can be doped to attain power factors over 10 μW/m-K$^2$. The progress in solution-processed n-type organic thermoelectric materials is shown in Figure 6.[54-63]

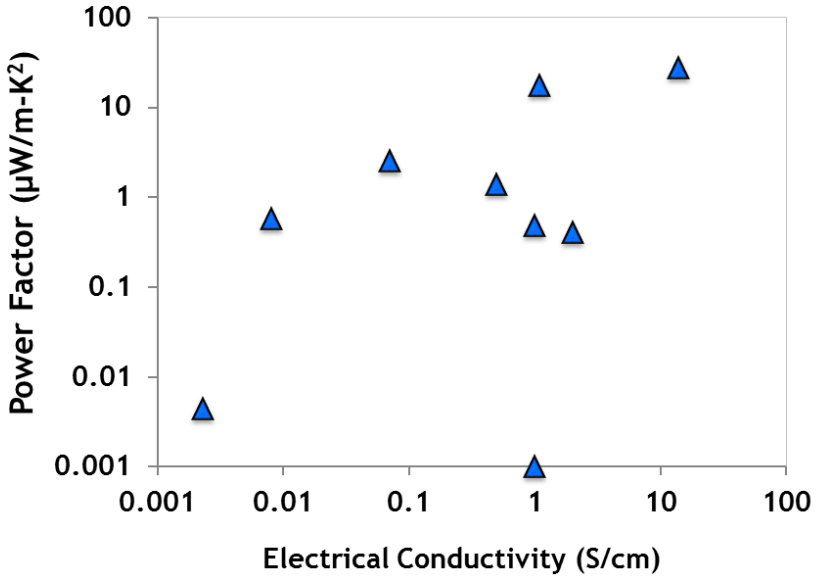


**Figure 6 – Thermoelectric properties of solution-processed n-type organic materials. The low electrical conductivity values necessitate the use of doping.**

Most of these materials have low power factors due to their low electrical conductivities, and require careful doping strategies which may cause them to de-dope in air over extended periods of time, thereby impacting device performance. In contrast, transition metal coordination complexes (metallo-organic polymers) have facile syntheses, relatively high electrical conductivities, and have been shown to be stable in ambient conditions. Of particular interest are polymers based on the ethenetetrathiolate (ETT) ligand coordinated to nickel due to their n-type nature, which is the focus of this chapter.

## 2.1 Metal-Ethenetetrathiolate (M-ETT) Polymers

Metal-ethenetetrathiolates are known to have high electrical conductivity and have been consistently researched for the last ~30 years[64-68] but their thermoelectric potential

was reported in 2012 for the first time.[23] The coordination environment between the ETT ligand and the metal center results in a coordination complex with significant electron delocalization along the backbone through ligand π-orbital and metal *d*-orbital overlap. This structure, combined with the observed non-integral oxidation state, gives rise to a conducting polymer.[69] It has been empirically observed that ETTs can show both p-type and n-type behavior; the metal center determines the sign of the Seebeck coefficient of the resulting polymer (NiETT and $Ni^0$ are negative; CuETT and $Cu^0$ are positive).[23,70] NiETTs offer advantages in that they: *(i)* have tunable electronic properties through multiple oxidation states on both the ligand and metal center, *(ii)* exhibit n-type behavior as evidenced by their negative Seebeck coefficients, and *(iii)* are stable to ambient conditions without special exclusion of moisture or oxygen. This has resulted in NiETTs exhibiting one of the highest organic n-type power factors (66 μW/m-$K^2$) as a pressed pellet.[23] Although this is promising, the *(i)* poorly understood synthetic pathway leads to irreproducible syntheses, *(ii)* insoluble nature of the final material limits traditional structural characterization, and *(iii)* fabrication via solution-based techniques requires the use of an insulating matrix that adversely affects performance. These challenges have resulted in a limited investigation and understanding of this metallo-organic polymer, as well as property variations across different groups.[23,63,71]

Given the insoluble nature of the NiETT polymer, it can be processed from solution by dispersing in an inert matrix. Specifically, poly[K(NiETT)] was dispersed in a poly(vinylidene fluoride) (PVDF) matrix using dimethyl sulfoxide (DMSO) to form a composite.[63] However, this resulted in a significant reduction in the power factor from 66 to 0.43 μW/m-$K^2$. To enhance the power factor, various blends have been investigated.

Toshima *et al.* studied ternary blends of NiETT nanoparticles, carbon nanotubes (CNTs), and poly(vinyl chloride) - adding NiETT to CNT/PVC blends had minimal effect on the Seebeck coefficient while increasing conductivity significantly for this p-type blend, giving a *zT* of ~0.3.[72,73] Additional studies utilized NiETT/CNT/cellulose acetate blends that increased the electrical conductivity by a factor of two relative to CNT sheets to form a p-type composite.[74] This indicates that blending NiETT with CNTs is an effective strategy to improve conductivity, however, the resulting blend is no longer n-type. Thus, other strategies are required to enhance the performance of this n-type polymer while making it solution processable. This has been the focus of my research and the subsequent sections present the property improvements that I have achieved.

## 2.2 Methodology for Investigation of NiETTs

Generally, ethenetetrathiolate polymers are synthesized by reacting 1,3,4,6-tetrathiapentalene-2,5-dione (TPD) with excess alkali base in an alcohol solvent with the goal of producing the ethylene tetrathiolate anion ($C_2S_4^{4-}$) under an inert environment. Although there is some contradictory evidence[66,67] on whether both carbonyl groups are cleaved simultaneously upon reacting the TPD with an alkoxide, it is well-understood that the addition of one molar equivalent of transition metal salts and subsequent oxidation results in the formation of the polymer. It has also been reported that the central metal, counter cation and oxidation state can all have significant effects on the electrical conductivity exhibited by these polymers.[23,66,67,75] Herein, the effects of oxidation on the n-type NiETT are investigated. In particular, the goal was to adapt literature reports for the synthesis of poly[K(NiETT)] and define an oxidation time that maximizes the electrical conductivity. This is motivated by a lack of consistency about the optimum oxidation

conditions for synthesizing this n-type polymer, as well as establishing processing conditions for ETT/PVDF composite films.

### *2.2.1 Synthesis of Poly[K(NiETT)]*

Poly[K(NiETT)] was synthesized following a reported procedure[23,63] with some modifications outlined here;[76] potassium was used as the counterion as previous literature reports have shown this to be the best performing polymer in the series.[23,63] The reaction was performed in a 250 mL, 24/40, 3-neck round bottom flask with attached condenser. Stirring was maintained throughout the procedure with a ½" Teflon-coated stir bar at 300 rpm. The reaction was not run under inert atmosphere, but open joints were sealed with septa. A solution of potassium methoxide (1.50 g, 22.2 mmol, Alfa Aesar) in methanol (45 mL, BDH) was prepared. The monomer, 1,3,4,6-Tetrathiapentalene-2,5-dione (1.0 g, 4.8 mmol, TCI America) was added in one portion, and the resulting solution was heated at 75 °C in an oil bath for 24 hours. Initially, this solution was yellow and darkened to brown-black after several minutes. Separately, a solution of nickel(II) chloride hexahydrate was prepared from nickel(II) chloride (0.63g, 4.8 mmol, Sigma Aldrich) and water (300 µL, deionized). This solution was diluted in 25 mL of methanol before addition to the reaction in one portion. The reaction was heated to reflux for an additional 24 hours. Heating was stopped, and the solution was immediately exposed to air for a specified time by removing the condenser and septa from all three necks, while stirring was continued at 300 rpm. During exposure, a black precipitate formed due to oxidation with air. The solids were collected by vacuum filtration onto a grade 40 filter paper and washed three times with 40 mL of deionized water then methanol. The resulting black solid was dried under vacuum

for 24 hours at room temperature and ground to a fine powder using a pestle and mortar. The synthesis scheme is shown in Figure 7.

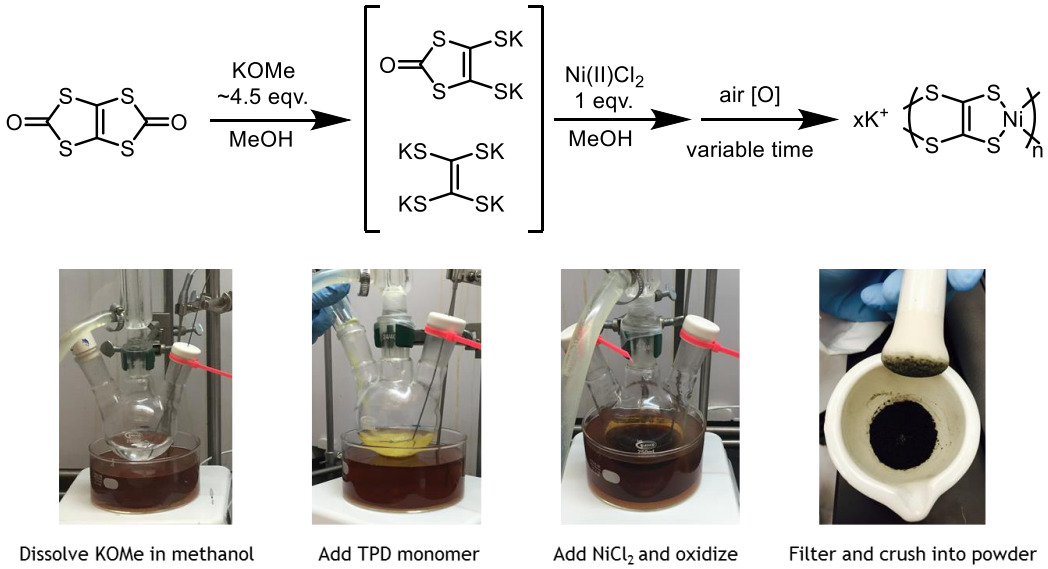


**Figure 7 – Synthesis of poly[K(NiETT)] showing half-ring or full-ring opening of the monomer, followed by complexing with Ni(II) and oxidation by exposing to air for a given amount of time to precipitate the polymer.**

It is noted here that this synthesis was not performed under inert conditions as was previously reported.[64,66] To facilitate a comparison with literature, an additional synthesis was performed in which all solvents were degassed with nitrogen and the reaction was performed under air-free conditions. It has been observed that the polymer precipitates immediately upon oxidation by air or a chemical oxidant, indicating that a short exposure time may be sufficient. However, the oxidation time used in literature varies from a few minutes to several hours, with 12-24 hours being used in recent reports.[21,61,62,65] To investigate and better understand the effects of oxidation on the electrical conductivity of K(NiETT), a systematic study was performed by varying the air exposure time. This was done by taking aliquots from the same synthesis batch at air exposure times of 20, 40, 60,

80 and 100 minutes. In addition, a separate batch of material was synthesized with an exposure time of 24 hours for comparison with literature.[76]

### *2.2.2 Polymer Characterization*

As these ETT-based polymers are insoluble in common solvents, the characterization techniques that can be employed are limited. Elemental analysis was employed to obtain the content of carbon, hydrogen, sulfur and chlorine by CHNS analysis and flask combustion (2400 II analyzer, PerkinElmer for CH, 1108 analyzer, Carlo Erba for S, and 790 IC, Metrohm Peak for Cl). The analysis of nickel and potassium was carried out on an inductively coupled plasma optical emission spectrometer, ICP-OES (OPTIMA 7300 DV, PerkinElmer). Each sample was dissolved in concentrated nitric acid and diluted with deionized water prior to analysis. XPS was performed to investigate the binding environment of the powder samples (Thermo K-Alpha XPS tool, Thermo Fisher Scientific Inc.). The operating pressure in the analysis chamber during data acquisition was $10^{-7}$ mBar and the X-ray spot size was adjusted to 200 μm. A built-in flood gun was used to eliminate the surface charging effects. To improve the signal-to-noise ratio, five consecutive scans were performed for the survey spectra (1 eV energy steps and 200 eV pass energy), and ten consecutive scans were performed for the elemental survey (0.1 eV energy steps and 50 eV pass energy). The survey scans were analyzed using Avantage software v5.959 (Thermo Scientific) in which the kinetic energy correction was made using $KE^{0.6}$, and Shirley or linear-type backgrounds were employed.[25] The chemical shift of the survey spectra was done using C1s peak referenced at 285 eV. The relative sensitivity factors referenced to C1s peak (Scofield sensitivity factors, 1 for C1s) were as follows: 1.67 for S2p, 22.18 for Ni2p, 3.97 for K2p, 2.285 for Cl2p, 2.93 for O1s.[77] The elemental scans

were chemically shifted with respect to K2$p_{3/2}$ peak at 293.2 eV (rather than C1s peak which had low signal-to-noise ratio in short air exposure samples) with Shirley-type backgrounds. Deconvolution of the peaks was carried out to investigate different functionalities in the elemental scans by minimizing the residual in the fit. The full-width at half-maximum (FWHM) values for all deconvoluted peaks were constrained to be the same in a single elemental scan, and curve fitting was performed using mixed Gaussian-Lorentzian line shapes, *i.e.*, GL(30) (GL(100) is pure Lorentzian and GL(0) is pure Gaussian). The molar percentages (which correspond to area percentages) of the doublets in Ni 2p, S 2p and K 2p peaks were analyzed for expected degeneracy due to spin-orbit coupling (~ 2:1 in $2p_{3/2}$:$2p_{1/2}$). The area percentages and binding energy positions of the deconvoluted peaks were not constrained in the deconvolution procedure, but obtained as a result of the analysis. Thermogravimetric analysis (TGA) was performed using Pyris 1 Thermogravimetric Analyzer (PerkinElmer) under argon. For these experiments, 6-10 mg of ETT powder was loaded into a platinum pan. The TGA program consisted of two steps: a 5 minute isothermal hold at 50 °C, followed by a 10 °C/min ramp rate up to 600 °C.

### *2.2.3 Thin Film Fabrication*

Given that NiETT is insoluble in common solvents, a composite film was prepared by ball-milling the ETT powder with a polymer matrix to form a dispersion. First, PVDF (Sigma Aldrich, MW ~180,000) was dissolved in DMSO (Amresco) at 80 °C for 4 hours under continuous stirring in an Erlenmeyer flask to form a 20 mg/mL solution. Next, 40 mg of ETT powder was added to 1 mL of the PVDF/DMSO solution with 10 zirconia beads (diameter = 1 mm) in a micro-vibration mill for 30 minutes (MSK-SFM-12M, MTI Corporation). Other electrically inert polymers such as PMMA, PVA and PVP were also

tested as binders, but films with PVDF had the best quality and resulted in the highest thermoelectric properties (see Appendix A.1). Thus, this was chosen as the binder for all studies reported in this dissertation. Films were prepared by drop-casting 35 µL of the composite on 1cm × 1cm pre-treated glass substrates and drying in a vacuum oven at 50 °C for 30 minutes (pre-treatment of glass substrates involves sequential cleaning with deionized water, acetone and isopropyl alcohol for 3 minutes each and placement in oxygen-plasma for 5 minutes). Four gold contact pads (1mm × 1mm, ~ 100 nm thick) were then deposited on the prepared films using a shadow mask in an e-beam evaporator. All films were 5-10 µm thick as measured with a profilometer (Dektak XT, Bruker).[76]

### *2.2.4 Thermoelectric Property Measurements*

For the composite films, transport measurements were performed as previously reported[15,38] using an in-house measurement setup. Micromanipulators with tungsten tips were used to make electrical contact to the gold contact pads, and sheet resistance was acquired based on the four-probe Van der Pauw technique. For Seebeck coefficient measurements, the film was suspended between two temperature-controlled Peltier stages (separated ~3 mm), and a series of temperature differences up to $\Delta T$ = 10 °C were applied between the stages. The thermoelectric voltage was measured between two contact pads on separate stages using the probe tips, while the temperature of each stage was measured with a K-type thermocouple in close proximity to the probe tips. Voltage and temperature data were acquired using a Keithley 2700 DMM with a 7708 Mux card via a LabVIEW interface. The Seebeck coefficient was extracted as the slope of the $V$ - $\Delta T$ plot. In order to obtain temperature-dependent properties, the Peltier stage temperature was changed from

20 – 100 °C using temperature controllers (Model LFI-3751). In all cases, thermal grease was applied on the backside of the substrate to ensure good thermal contact with the Peltier stage. Five films were measured to capture sample-to-sample variations; this is reported as the standard deviation and represented by error bars around the average value.

## 2.3 Results and Discussion

The electrical conductivity of K(NiETT) varies as a function of the extent of oxidation in air. As shown in Figure 8, there is an optimum exposure time between 20 and 40 minutes that maximizes the electrical conductivity. To ensure the results were reproducible, additional syntheses were performed with an exposure time of 30 minutes as well as with an exposure times of 24 hours for comparison with literature. The in-depth analysis and thermoelectric measurements for these two syntheses are presented herein.

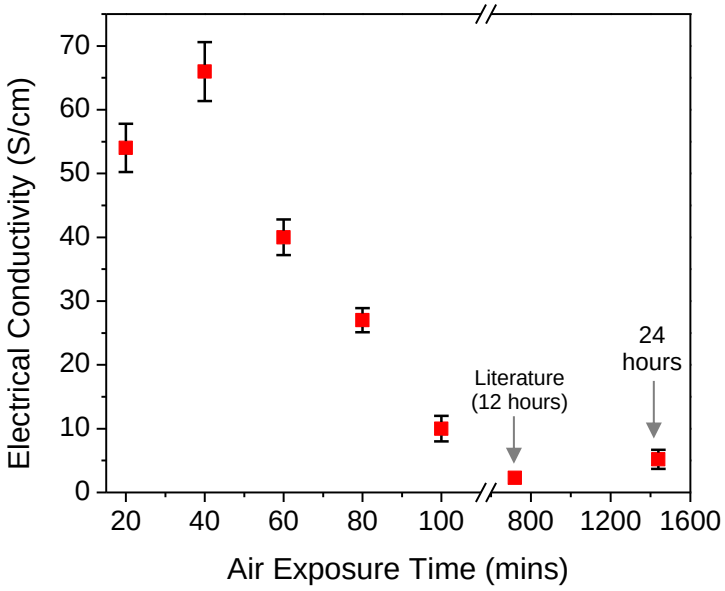


**Figure 8 – The electrical conductivity of K(NiETT)/PVDF composite films changes as a function of the extent of oxidation (exposure to air). A maximum is attained ~ 30 minutes, after which conductivity decreases down to literature values of 2 S/cm.[63]**

### *2.3.1 Elemental Composition of K(NiETT)*

The empirical formula for ETTs was first reported by Poleschner *et al.* to fit $A_x(MC_2S_4)$, where *A* represents the counterion (potassium in this case) and *M* is the central metal (nickel in this case).[68] Recent literature reports show deviations from this idealized structure, but the limited characterization techniques available to this material make it challenging to predict the actual structure.[23,50] Table 1 shows the elemental composition of the 30-minute and 24-hour K(NiETT) powder samples, and atomic ratios are provided to facilitate a comparison with the proposed structure. Although the oxygen content could not be measured directly from the elemental analysis methods employed, XPS survey scans clearly indicate the presence of oxygen in these materials, and hence, the oxygen content is calculated as the remainder in summing to 100%.

**Table 1 – Elemental composition of poly[$K_x$(Ni-ETT)] obtained from combustion analysis[a] and ICP-OES[b] for 30-minute and 24-hour samples. Atomic ratios are provided to compare with the expected empirical formula [$A_x(MC_2S_4)$].**

Elemental Analysis - Weight %

| | C[a] | H[a] | S[a] | Ni[b] | K[b] | Cl[a] | O |
|---|---|---|---|---|---|---|---|
| 30 mins | 9.08 | 0.78 | 47.31 | 22.06 | 8.71 | 2.13 | 9.93 |
| 24 hours | 8.36 | 1.58 | 35.65 | 21.32 | 3.52 | 1.98 | 27.62 |

Atomic Ratios

| | Theoretical | 30 mins | 24 hours |
|---|---|---|---|
| Ni : C | 0.50 | 0.50 | 0.52 |
| S : C | 2.00 | 1.95 | 1.60 |
| Ni : S | 0.25 | 0.25 | 0.33 |
| K : Ni | - | 0.59 | 0.25 |

Deviations from the ideal composition along with unexpected elements (H, Cl, O) are observed in both the 30-minute and 24-hour samples. Several factors contribute to these deviations - chain ends give potential sites for incorporation of H, Cl, and O and the low degree of polymerization expected for this polymer gives terminal groups a larger impact on overall composition. Additional purification and isolation of the target material is precluded due to its insolubility. The presence of hydrogen and oxygen in these polymers may be attributed to solvent or water molecules associated with the counterion, or with different terminal groups.[23,66,67] TGA analysis for both samples (30 minutes and 24 hours) shows a weight loss of about 2% at 50 °C which is expected to be contact moisture, and over 5% around 175 °C, above which the polymer decomposes (see Appendix A.2). Cl may be from $NiCl_2$ used in the synthesis that exists as an impurity and is difficult to remove.

The 30-minute sample is in good agreement with the expected formula of $A_x(MC_2S_4)$, indicating that this smaller exposure time is sufficient for precipitating the polymer. The 24-hour sample has a smaller amount of sulfur than expected, which suggests that there may be some decomposition of the polymer through an extended oxidation process, or other factors that are discussed subsequently. The K:Ni ratio is an indirect indication of the degree of oxidation in the polymer, *i.e.* the smaller the ratio, the higher the degree of oxidation,[66] which is the case for the 24-hour sample from Table 1. This is expected since the 24-hour sample is more oxidized than the 30-minute sample, thereby requiring less $K^+$ couterions for charge neutrality. The nature and concentration of the counterion play an important role in influencing the electrical properties as it may facilitate chain stacking which provides additional conduction pathways (inter-chain transport);[67] this is explored in greater detail in Chapter 3. The atomic % of potassium in the 24-hour

sample is identical to that reported by Vogt *et al.*, however Sun *et al.* report negligibe amounts of potassium in their synthesis.[23,65] Futhermore, there is no data provided on the sulfur composition which makes a direct comparison on material composition with literature challenging.

### *2.3.2 XPS Analysis of NiETT Powders*

Due to the small signal-to-noise ratio in the 30-minute sample, deconvolution in a meaningful manner is challenging. Furthermore, XPS is a surface characterization tool so the Ni, K and C signals may not be representative of the bulk material in the 30-minute sample due to the poor signal intensity. Acknowledging this limitation, attempts were made to compare S signals between the 24-hour and 30-minute samples as these deconvolutions are statistically valid. First, the C1s and K2p elemental scans were deconvoluted for the 24-hour sample, as shown in Figure 9. The K2p peak is deconvoluted into $K2p_{3/2}$ peak at 293.20 eV and $K2p_{1/2}$ peak at 295.94 eV with an area ratio of about 2:1 and a peak separation of 2.74 eV, in agreement with literature.[78,79] This indicates a single binding environment for K, as expected given that potassium acts only as a cation for charge neutrality in the polymer. The deconvolution of C peak resulted in five statistically valid sub-peaks. Given the limited number of applicable characterization methods for this insoluble material, the assignment of binding environments to these sub-peaks is challenging, especially at the lower binding energy side (peaks A and B). Peak A at 283.86 eV and peak B at 284.94 eV might occur due to different oxidation states of S in the C-S-Ni binding environment. This has been observed for Ni-DMID and CuETT samples where the oxidation is a ligand-centered process taking place at S, and may be extended to the NiETT as well.[75,80]

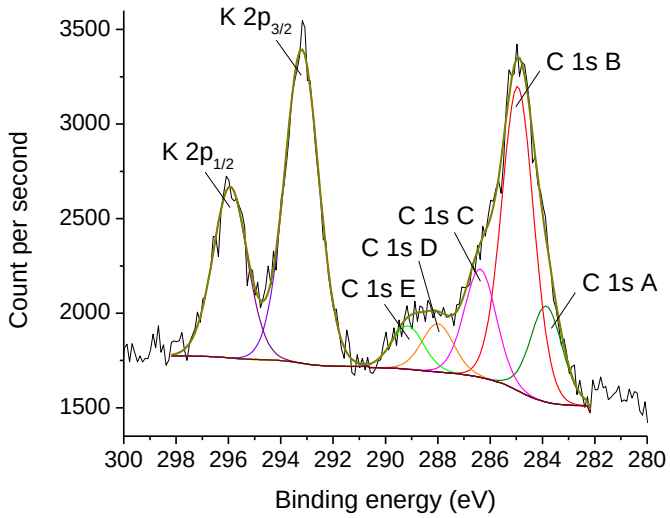


**Figure 9 – C1s and K2p spectra and associated deconvolution for the 24-hour NiETT powder sample obtained from XPS**

Other peaks in the C1s scan at 286.38 eV (peak C) and 288 eV (peak D) may indicate the presence of hydroxyl end groups (C-OH) and a carbonyl (C=O) functionality, respectively.[67,81,82] Vicente *et al.* attributed the presence of carbonyl in ETT polymers to a half-ring opening of TPD in the synthesis.[66] The peak at 289.15 eV (peak E) likely indicates a shake-up process due to π-π* transition in C=C bond showing a degree of aromaticity in the molecule or an ester functionality (O-C=O), albeit the latter is less likely.[81,83,84]

Next, for the 24-hour sample, the Ni2p$_{3/2}$ peak was deconvoluted into two sub-peaks with binding energies of 853.90 eV (sub-peak A) and 856.06 eV (sub-peak B) with an area ratio of 2.05:1, as shown in Figure 10. The peak separation and the calculated area ratio agree well with values reported in literature, indicating an identical Ni environment.[63] Previous reports on poly[Na(NiETT)] suggest that peaks A and B correspond to Ni in the polymer backbone and Ni acting as counterion, respectively. This is investigated in detail in Chapter 3.

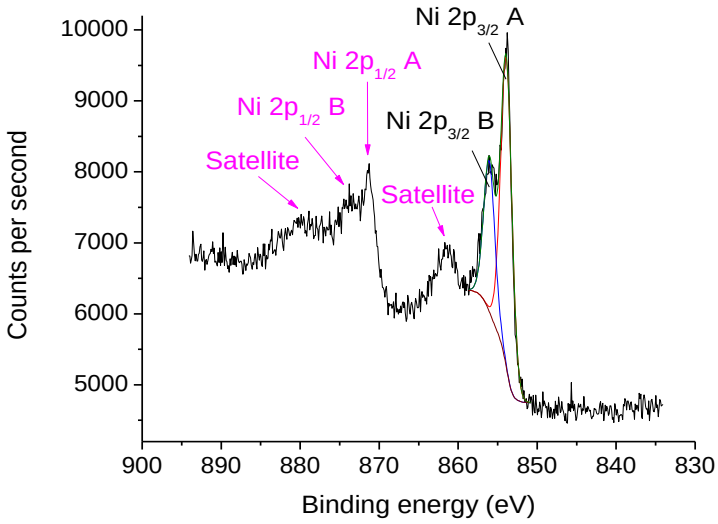


**Figure 10 – Ni2p spectra and associated deconvolution for the 24-hour NiETT powder sample obtained from XPS**

Finally, the S2p scan and deconvolution for the 24-hour sample was performed and is presented in Figure 11. There are two regions in the S2p peak: the main region between 159.8-166.5 eV, and an additional region between 166.5-172.1 eV. The S2p peaks found in the main region (peak A and peak B) are attributed to the S bridging with Ni in the polymer backbone indicating two distinct binding environments for S;[75,84] this might occur due to variations in the oxidation states of S and/or Ni.[80,84] The peak separation in both peak A and peak B doublets is about 1.2 eV, in agreement with literature values.[78,85] The degeneracy ratio of peak B shows the expected value of 2:1, whereas peak A deviates and is about 1:1. In comparison, for the S2p scan of the 30-minute sample, the degeneracy ratio holds for both the A and B peaks along with expected peak positions and separations.

One possible explanation for the area ratio deviation in the 24-hour sample is the presence of an additional functionality, which is likely from disulfides owing to prolonged oxidation (*i*.e., longer oxidation times form more disulfides).[86,87] A possible presence of disulfides in the polymer backbone might adversely affect the electrical conductivity by

destroying conjugation, as depicted in the lower electrical conductivity of the 24-hour sample compared to that of the 30-minute sample. The peaks in the other S2p region (peaks C, D, and E) might point to the presence of oxides of sulfur and/or shake-ups indicating conjugation in the molecule.[80,85,88] The stark difference in the S2p peak shapes between 24-hour and 30-minute samples is interesting and found to be repeatable in the other short exposure time samples (*i.e.*, 20-minute through 80-minute samples).

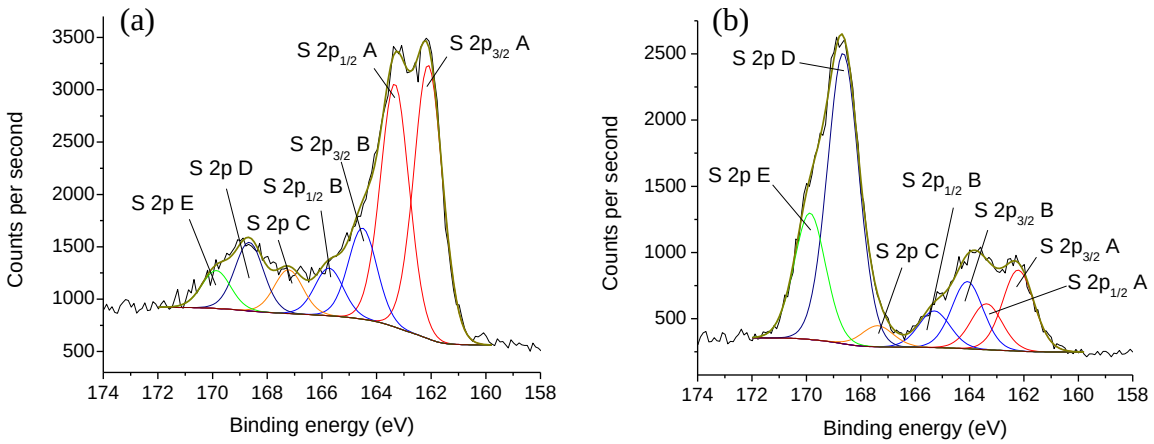


**Figure 11 – S2p spectrum and deconvolution for: (a) 24-hour sample and (b) 30-minute NiETT sample from XPS. Both samples show the presence of different binding environments for sulfur in the polymer.**

The variation of oxygen content across all samples as well as the differences in XPS surface composition compared to bulk elemental analysis indicates that air oxidation may not be the best approach for reproducible syntheses.

### *2.3.3 Thermoelectric Properties of NiETT/PVDF Composite Films*

By shortening the air exposure time from 24-hours to 30-minutes, the electrical conductivity of K(NiETT) is enhanced by a factor of eight. In fact, this value is twenty times higher than that reported in the literature.[63] Comparing the 24-hour sample to previous work with long exposure times,[63] the conductivity is over two times higher. This

may be attributed to using a 4:1 ETT/PVDF ratio compared to 2:1 used in literature, as shown in Table 2. The thermoelectric properties for the air-free syntheses are also tabulated, as these materials provide an experimental control and direct comparison with literature. The negative Seebeck values are indicative of n-type behavior with electrons as primary charge carriers in the NiETT polymer.

**Table 2 – Thermoelectric properties of composite films of Poly[K(NiETT)] with PVDF/DMSO (4:1 w/w ratio) at $T$ = 298 K**

| Exposure Time | $\sigma$ (S/cm) | $S$ (μV/K) | $S^2\sigma$ (μW/m-K$^2$) |
|---|---|---|---|
| 12 hours (2:1 ratio) [63] | 2.1 | - 45* | 0.43 |
| 24 hours | 5.2 ± 0.1 | -27 ± 3 | 0.38 ± 0.06 |
| 30 minutes | 43 ± 4 | -33 ± 1 | 4.68 ± 0.48 |
| Air-free 24 hours | 0.5 ± 0.2 | -27 ± 3 | 0.04 ± 0.02 |
| Air-free 30 minutes | 1.8 ± 0.1 | -26 ± 1 | 0.12 ± 0.01 |

* There is a discrepancy in the value reported in the main manuscript (-45 μV/K) and in the supplemental information (-28 μV/K).[63]

One possible explanation for the variation in observed properties could be the extent of partial oxidation, defined as the molar ratio of counterion to central metal. This relationship between the partial oxidation and electrical conductivity in materials with similar structures to NiETT has been observed previously. For example, Holdcroft *et al.* measured the electrical conductivities of p-type poly[Cu(CuETT)] by varying the degree of partial oxidation (DPO) using oxidants such as air, hydrogen peroxide, chlorine and iodine prior to addition of the metal salt.[67] Compared to an unoxidized polymer, small increases in DPO was observed to increase the electrical conductivity by a factor of ten. Larger DPO values, however, decreased the electrical conductivity back to that of the

unoxidized polymer. Vicente *et al.* studied the effect of partial oxidation on poly[TBA(NiETT)] (TBA: tetrabutylammonium) and observed two orders-of-magnitude electrical conductivity increase in partially oxidized samples compared to unoxidized polymers by exposing the material in open atmosphere.[66] Extending these observations to poly[K(NiETT)], the 30-minute sample shows a larger degree of partial oxidation and a corresponding high value of electrical conductivity compared to the 24-hour sample. Liu *et al.* made similar observations in [TBA][Ni(DMID)$_2$] (DMID=1,3-dithiole-2-one-4,5-dithiolate) based on XPS that showed an intensification in the satellite peak at 168.7 eV in the S2p scan with an increase in the DPO, which agrees with the XPS scans shown in Figure 11. They attributed this to a ligand-centered oxidation occurring at sulfur in DMID moieties that resulted in an improvement in conjugation.[88] The effects of partial oxidation on NiETT have not been reported before and will be explored further in chapter 3.

Figure 12 shows how thermoelectric properties change with increasing the content of ETT powders in the PVDF/DMSO composite films. The electrical conductivity increases with increase in the NiETT amount as expected, while the Seebeck coefficient is almost constant within experimental error limits. This is expected as a larger amount of conducting material would increase $\sigma$ but the thermopower would not vary beyond the percolation threshold. The 4:1 w/w mass ratio (*i.e.*, 40 mg NiETT in a 10 mg/mL solution of PVDF/DMSO) was chosen for all measurements reported herein as it resulted in a uniform film quality and consistent thermoelectric properties across all syntheses batches performed on the same scale (1 g). However, upon scaling up the reaction, inconsistencies in air oxidation result in lower $\sigma$ values.

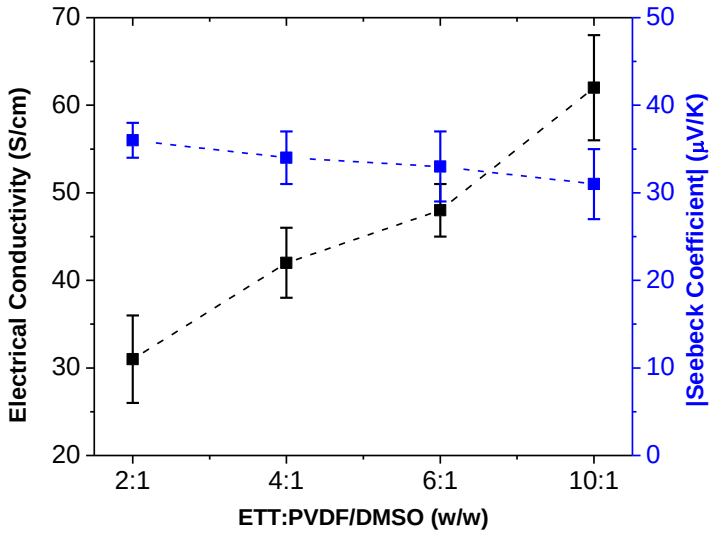


**Figure 12 – Electrical conductivity of composite films increases with increasing loading of NiETT particles in the inert binder. The Seebeck coefficient remains around -30 μV/K for all ratios studied.**

To test the stability of K(NiETT) films blended with PVDF/DMSO in air, samples were stored in ambient conditions (room temperature and ambient humidity), and properties were measured over time, as shown in Table 3. No significant differences in the properties were observed over a one-year period, confirming that unlike common n-doped polymers that tend to de-dope in the presence of oxygen and/or water, NiETT is a viable material for practical thermoelectric devices.[76] Note here that these $\sigma$ values are lower than 40 S/cm as the ETT reaction was scaled up to a 5 g synthesis.

**Table 3 – Air stability of films of Poly[K(NiETT)] with PVDF/DMSO over time**

| Time | $\sigma$ (S/cm) | $S$ (μV/K) |
|---|---|---|
| Initial Value | 13 ± 1 | -33 ± 1 |
| After 6 months | 13 ± 2 | -30 ± 2 |
| After 1 year | 12 ± 1 | -32 ± 1 |

### *2.3.4 Charge Transport in K(NiETT)*

As a final step, the temperature dependent thermoelectric properties for the 30-minute sample were measured to provide insight on the charge transport mechanism, as shown in Figure 13. The electrical conductivity was found to increase with temperature to give a negative temperature coefficient of resistance. This suggests that transport is thermally activated, and that these polymers are semiconducting in nature. This is as expected for disordered materials and fits within the framework of hopping conduction. In this temperature range, the Seebeck coefficient increases slowly and its magnitude is in the expected range for hopping conduction (tens of μV/K).

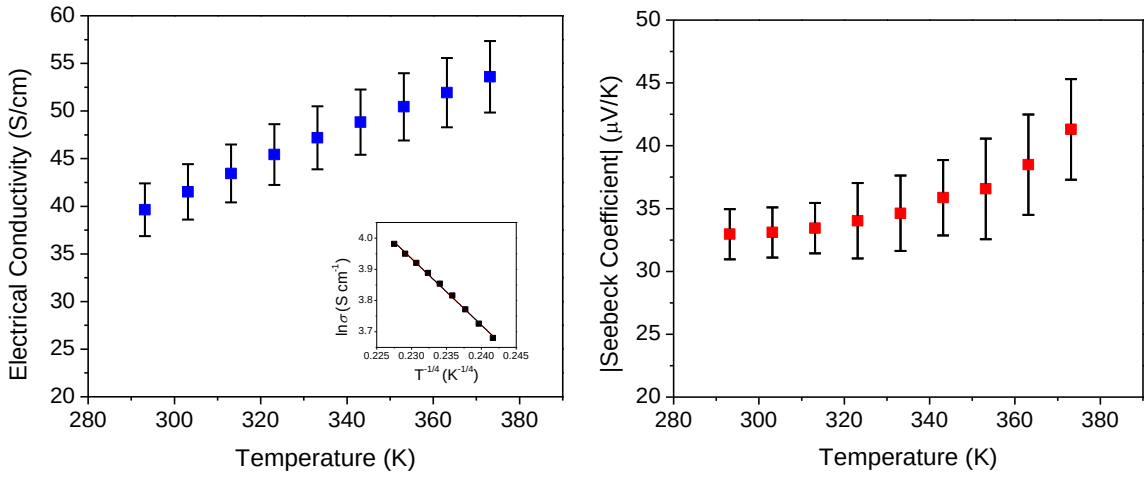


**Figure 13 – Temperature dependent thermoelectric properties of K(NiETT)/PVDF composite films with 30-minute air exposure. (a) Electrical conductivity and (b) Seebeck coefficient increase with temperature which is indicative of hopping conduction.**

The plot of ln($\sigma$) as a function of $T^{-1/4}$ (see inset, Figure 13) yields a linear fit which indicates that charge transport follows Mott's variable range hopping in three dimensions.[27,36]

## 2.4 Conclusions

Metallo-organic complexes with nickel as the metal center exhibit high electrical conductivities and n-type behavior, thereby warranting investigation and optimization of their thermoelectric properties. In this chapter, I have demonstrated the tunability of poly[K(NiETT)] composite films with PVDF/DMSO. By reducing the air exposure time (thereby tuning the extent of oxidation) during the synthesis from 24-hours to 30-minutes, electrical conductivity was increased by a factor of eight while the Seebeck coefficient remained unchanged. This result suggests that tuning the synthesis conditions is a viable strategy to decouple $S$ and $\sigma$, and is a key result of this chapter. It was observed, for the first time that extended oxidation leads to inferior thermoelectric properties, potentially due to a break in conjugation and formation of undesirable functionalities, as evidenced from the XPS results. Similar oxidation studies on PEDOT:Tos and CuETT have shown that there is indeed an optimum oxidation level that maximizes electrical conductivity.[18,75] XPS characterization also suggested that differences across samples may be attributed to inconsistencies with air oxidation at different reaction scales. These observations motivate further investigation of these polymers through systematic synthesis optimization, as well as strategies to improve the thermopower; this is the focus of the following chapter.

# CHAPTER 3. SYSTEMATIC ENHANCEMENT OF ETT/PVDF COMPOSITE FILMS

Metallo-organic polymers based on the ethenetetrathiolate ligand coordinated to nickel were previously discussed (Chapter 2) and shown to be promising n-type thermoelectric materials. It is well-known that the counterion, central metal and oxidation state can impact the electrical conductivity exhibited by these metallo-organic polymers.[23,66,67,75] The latter was investigated for K(NiETT), where it was found that the extent of oxidation could be controlled by varying the air exposure time to maximize electrical conductivity.[76] However, reproducibility was a challenge for larger reaction scales, and differences were observed between the surface and bulk material. This suggests the need for a robust oxidation procedure beyond air exposure, as well as a systematic study of the other synthesis parameters to further enhance the thermoelectric performance of NiETTs. In this chapter, drawbacks are addressed to provide a deeper understanding of the material, and an optimized synthesis is developed that is reproducible and scalable. Furthermore, post-treatment of films is performed and is found to increase the Seebeck coefficient of NiETT polymers.

## 3.1 Methodology for Investigation of NiETTs

The poorly understood reaction mechanism in the formation of NiETT and lack of characterization techniques to study the structures of these insoluble complexes make synthetic optimizations difficult. To better understand how changes to the reaction conditions affect thermoelectric performance, the reaction is sub-divided into three major

steps as shown in Figure 14. Systematic variations across individual steps, while keeping all other reaction conditions constant, create families of materials for direct comparison.

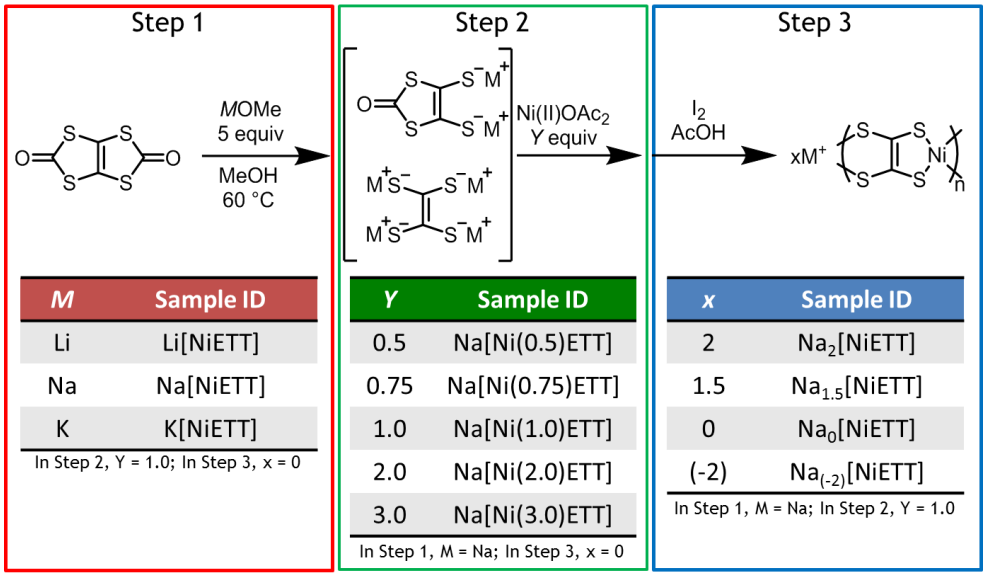


| M | Sample ID |
|---|---|
| Li | Li[NiETT] |
| Na | Na[NiETT] |
| K | K[NiETT] |

In Step 2, Y = 1.0; In Step 3, x = 0

| Y | Sample ID |
|---|---|
| 0.5 | Na[Ni(0.5)ETT] |
| 0.75 | Na[Ni(0.75)ETT] |
| 1.0 | Na[Ni(1.0)ETT] |
| 2.0 | Na[Ni(2.0)ETT] |
| 3.0 | Na[Ni(3.0)ETT] |

In Step 1, M = Na; In Step 3, x = 0

| x | Sample ID |
|---|---|
| 2 | $Na_2$[NiETT] |
| 1.5 | $Na_{1.5}$[NiETT] |
| 0 | $Na_0$[NiETT] |
| (-2) | $Na_{(-2)}$[NiETT] |

In Step 1, M = Na; In Step 2, Y = 1.0

**Figure 14 – The synthesis of NiETT is sub-divided into three modifiable steps for thermoelectric property optimization.**

In Step 1, to isolate the effect of the counterion on the reaction and final material, three methoxide species were used: lithium methoxide, sodium methoxide, and potassium methoxide. The three otherwise identical reactions yield Li[NiETT], Na[NiETT], and K[NiETT]. In Step 2, to isolate the effect of nickel deficiency or excess, five NiETTs with different stoichiometric equivalents of nickel(II) acetate were synthesized while keeping the counterion fixed using sodium methoxide: Na[Ni(0.5)ETT], Na[Ni(0.75)ETT], Na[Ni(1.0)ETT], Na[Ni(2.0)ETT], and Na[Ni(3.0)ETT]. Finally in Step 3, to isolate the effect of oxidation extent, four reactions using one equivalent of nickel(II) acetate and sodium methoxide were synthesized: no chemical oxidation, $Na_2$[NiETT]; partial chemical oxidation, $Na_{1.5}$[NiETT]; full oxidation to the neutral polymer, $Na_0$[NiETT]; and over-oxidation, $Na_{-2}$[NiETT]. Here, the sodium subscript indicates the expected number of

counterions per repeat unit, and therefore the expected negative charge on the backbone per repeat unit of the polymer (subscripts do not indicate the actual amount of sodium counterions per repeat unit). A negative subscript indicates a stoichiometric excess of oxidant was used for that sample. It has been previously shown (see chapter 2) that the extent of oxidation from exposure to air drastically affects thermoelectric performance;[76] this is addressed by using a chemical oxidant, *i.e.,* iodine, as control over atmospheric oxidation is challenging and results in property variations at different reaction scales.

### *3.1.1 Synthesis of Poly[Na(NiETT)]*

In a 100 mL round bottom flask with magnetic stir bar, thiapendione or TPD was added (500 mg, 2.4 mmol, 1.0 equiv) against a positive flow of argon. Anhydrous, degassed MeOH (15 mL) was added by syringe, and the reaction was heated to 60 °C. Separately, freshly prepared NaOMe (648 mg, 12 mmol, 5.0 equiv) was dissolved in MeOH (15 mL) and added to the reaction. The reaction immediately turns a light yellow color that becomes darker (brown to black) over time. Separately, anhydrous Ni(II)$OAc_2$ (424 mg, 2.4 mmol, 1.0 equiv) was dissolved in anhydrous MeOH (20 mL). At the 24 hour reaction mark, the addition of the Ni(II) solution was started at a rate of 20 mL/hour, such that the Ni(II) solution is added over 1 hour. The reaction becomes a "sol-gel" during the addition, such that stirring was significantly impeded. The reaction was stirred at 60 °C for an additional 23 hours, to give a total active reaction time of 48 hours. Glacial acetic acid (1 mL in 10 mL MeOH) was added rapidly by syringe to quench any remaining base before addition of the oxidant. Next, iodine (609 mg, 2.4 mmol, 2.0 equiv of oxidant) in MeOH (10 mL) was added in one portion. The reaction was allowed to stir for several hours at 60 °C, at which point the iodine color had faded from the solution, the "sol-gel" had become a fine

suspension, and the reaction suspension settles upon removal of stirring. The solids were collected on a 0.45 μm nylon filter. Without allowing the slurry to filter completely between washes, the product was washed three times each with methanol, distilled water, methanol again, and finally ether. The resulting lustrous grey-blue material was allowed to dry on the filter. After crushing in an agate mortar and pestle, the powder was dried again under high vacuum to remove any trapped solvent.

### *3.1.2 Polymer Characterization*

The content of carbon, hydrogen and sulfur were obtained by combustion analysis (2400 II analyzer, PerkinElmer for CH, 1108 analyzer, Carlo Erba for S). The analysis of nickel and sodium was carried out on an inductively coupled plasma optical emission spectrometer, ICP-OES (OPTIMA 7300 DV, PerkinElmer). Each sample was dissolved in concentrated nitric acid and diluted with deionized water prior to analysis. XPS was performed on the powder samples using a Thermo K-Alpha XPS (Thermo Fisher Scientific Inc.). Survey scans as well as elemental scans for C, Na, S, O, Ni, and $I_2$ were done at two depth levels: a surface level and a depth level of ~20 nm using an Ar-ion beam for etching. Herein, data is presented from the depth analysis to eliminate surface contamination from adventitious C and O. Although XPS is a surface characterization tool, the atomic % at the surface and depth for iodine-oxidized Na(NiETT) agree reasonably well (within 15%) indicating that the material composition is homogeneous and representative of the bulk. Thermogravimetric analysis coupled with mass spectrometry was performed on a NETZSCH STA 449F1 Jupiter coupled with a NETZSCH QMS 403 Aeolos mass spectrometer via a transfer line kept at 300 °C. Samples were run in a 25 μL aluminum crucible under a constant flow of argon (70 mL/min). The heating profile was 40 to 160 °C

at 10 K/min, isothermal at 160 °C for 60 minutes, and 160 to 600 °C at 10 K/min. SEM images were obtained using the SU-8230 tool (Hitachi).

### 3.2 Results and Discussion

Two distinct qualitative forms of NiETT are observed across all syntheses: amorphous black powders and blue-gray lustrous powders, indicating the formation of a poly-crystalline or heterogeneous material in contrast to the completely amorphous polymer reported in literature.[23] The elemental composition of both forms are identical, indicating that the effect is morphological and can be attributed to different crystallite sizes or packing differences, as shown in Figure 15. In order to measure the thermoelectric properties of ETT materials, a composite film was fabricated by ball-milling ETT powder with a PVDF matrix to form a dispersion in DMSO. Binder selection and ETT/PVDF ratios were discussed in chapter 2 and omitted here for sake of brevity.[76]

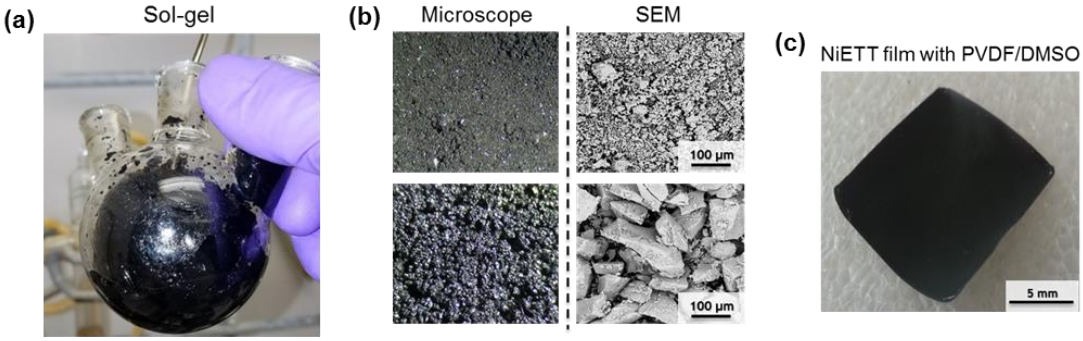


**Figure 15 – (a) A 100 mL flask containing oxidized Na[NiETT]; (b) Optical microscope (left column) and SEM images (right column) of the two observed forms of NiETT powders: black and amorphous (top row), blue-gray and poly-crystalline (bottom row); (c) Image of fabricated NiETT/PVDF composite film for thermoelectric property measurements.**

Performance enhancements and thermoelectric property optimization can be achieved by tuning the synthesis as well as performing film post-treatment via annealing.

### *3.2.1 Film Post-Treatment by Annealing*

As-cast films were prepared as follows: NiETT powder was dried for 24 hours under vacuum at room temperature and then dispersed in the PVDF/DMSO solution. This mixture was drop cast on a glass substrate and dried under vacuum for 30 minutes at 50 $^{0}$C to remove solvent and yield films that are 5-10 µm thick. As a first step, the films were annealed to investigate the effect of film post-treatment on the resulting thermoelectric properties. To establish annealing conditions, the temperature was varied for NiETT/PVDF films and the resulting thermoelectric properties were recorded as shown in Figure 16.

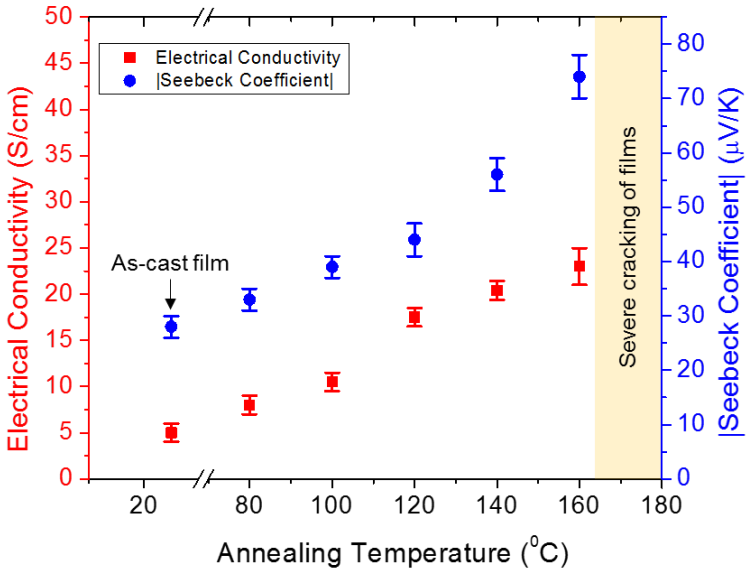


**Figure 16 – Electrical conductivity and Seebeck coefficient (magnitude) of NiETT/PVDF composite films as a function of annealing temperature. All films are annealed in air for one hour on a hot-plate prior to making thermoelectric measurements.**

The electrical conductivity and thermopower of composite films increase simultaneously with increasing annealing temperature and are maximized at 160 $^{0}$C. Annealing at higher temperatures resulted in severe cracking of films and complete delamination from the substrate in some cases. The binder and film forming polymer,

PVDF, melts at 169 $^0$C; near and above this temperature, phase separation occurs between NiETT and PVDF causing film cracking. Upon annealing at 160 $^0$C, conductivity increases from 6 ± 2 S/cm for an as-cast film to 23 ± 3 S/cm; this is accompanied by an increase in the Seebeck coefficient from -28 ± 3 µV/K to -74 ± 4 µV/K, to yield a power factor over 10 µW/m-K$^2$ for this n-type film. These properties are repeatable across multiple syntheses at different scales, as shown in Figure 17, indicating that annealing is instrumental in enhancing properties.

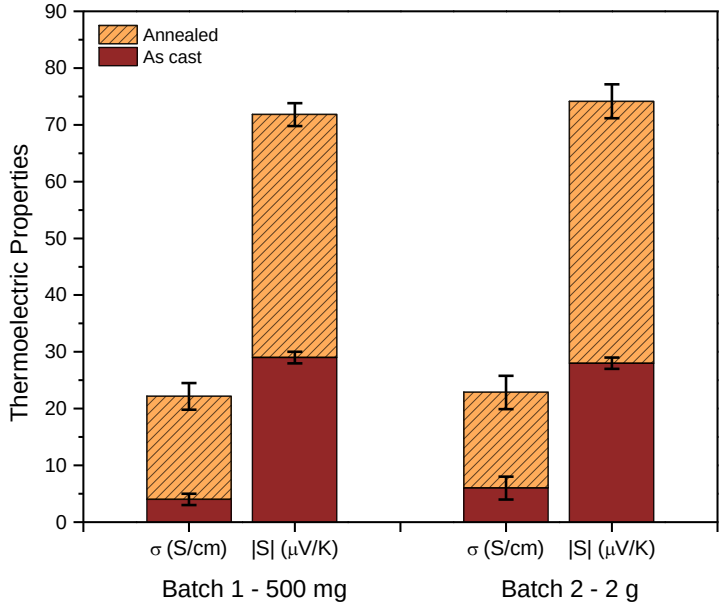


**Figure 17 – Thermoelectric performance of two batches of $Na_0$[Ni(1.0)ETT] showing consistent performance both before and after film annealing at 160 °C. The Seebeck coefficients of all NiETTs are negative, but the absolute value is shown for simplicity.**

To test for air stability during annealing, additional films were annealed at 160 $^0$C in a vacuum and under nitrogen for one hour – the resulting thermoelectric properties were identical to air annealed samples, indicating that there is no degradation during the annealing process. Furthermore, XPS elemental scans of Ni2p and S2p before and after annealing remain unchanged, which confirms there is no redox activity due to annealing.

While the improvement in the electrical conductivity with annealing can be attributed to morphological changes, the simultaneous enhancement in thermopower was surprising. Thermogravimetric analysis shows that annealing results in a 5% mass loss of the NiETT powder and a 7% mass loss in the NiETT/PVDF/DMSO film, indicating that different species may be evolved during the annealing process. To isolate compositional changes in NiETT powders from morphological changes in NiETT/PVDF composite films upon annealing, the NiETT powder was first annealed at 160 $^{0}$C for one hour in air and then cast as a NiETT/PVDF thin film from DMSO that yielded a thermopower of -45 μV/K. This is an improvement compared to the control sample (-28 μV/K) indicating that there is a change occurring in the NiETT powder when annealed. Upon annealing films prepared with annealed powders at 160 $^{0}$C for one hour in air, the thermopower increases to -80 μV/K. This reveals that the underlying mechanism involves changes in the NiETT powder alone, as well as changes due to the combination of NiETT/PVDF/DMSO. Spectroscopic and microscopic characterization were employed to gain insight into these changes.

#### 3.2.1.1 Morphological Changes during Annealing

It is known that favourable interaction between the binder and solvent can significantly impact the residual solvent in the film. Furthermore, given that DMSO is a low vapor pressure solvent and hygroscopic in nature, vacuum drying for 30 minutes is not sufficient to remove all the solvent. During the annealing post-treatment process, some of this residual solvent is removed which causes a densification of the film that brings domains closer together and closes existing cracks (from thermal stresses during vacuum drying) in the center of the film. This in turn leads to new cracks forming at the edges of the film, as shown in Figure 18.

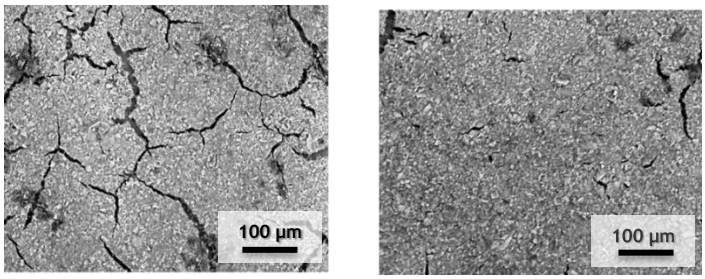


**Figure 18 – SEM images of NiETT/PVDF composite films before annealing (left) and after annealing (right) for one hour in air at 160 $^{0}$C.**

Annealing just below the melting temperature of PVDF (*i.e.*, annealing at 160 °C) allows NiETT to reorganize into better connected domains which improves carrier mobility. Similar observations have been made with carbon nanotubes in an inert matrix, where the filler reorganizes into more conducting pathways upon annealing.[89,90] This morphological effect is reflected in a higher $\sigma$ for annealed NiETT/PVDF films compared to as-cast films. However, an increase in the thermopower is also observed which cannot be explained by improved mobility alone; this indicates that an additional factor is at play during the annealing process. This is hypothesized to be the removal of impurities in addition to the above-mentioned morphological effects. Tandem thermogravimetric analysis – mass spectrometry (TGA-MS) was employed to gain insight into the species evolved during the annealing process.

#### 3.2.1.2 Compositional Changes during Annealing

Thermogravimetric analysis indicates four mass loss events occur in the NiETT powder and in the NiETT/PVDF composite films during heating to 600 °C; these are indicated as Events A-D. Event A, mimicking the annealing conditions, occurs upon heating to and holding at the annealing temperature of 160 °C for one hour. Event B begins at ~190 °C and shows a peak mass loss rate at ~235 °C, indicating significant

decomposition of the polymer at these temperatures. Event C (peak loss rate at 385 °C) and Event D (peak loss rate at 595 °C in powders, 470 °C in films) are attributed to continued decomposition of NiETT and PVDF. Mass loss Event A is critical to understanding the effect of annealing on NiETT powders and NiETT/PVDF composites, and is discussed here in greater detail. First, the powder samples are considered: NiETT powder in its original state (Pristine Powder, **PP**) and NiETT powder after annealing at 160 °C for one hour in air (Annealed Powder, **AP**); Figure 19 shows the TGA data and mass loss events for these samples.

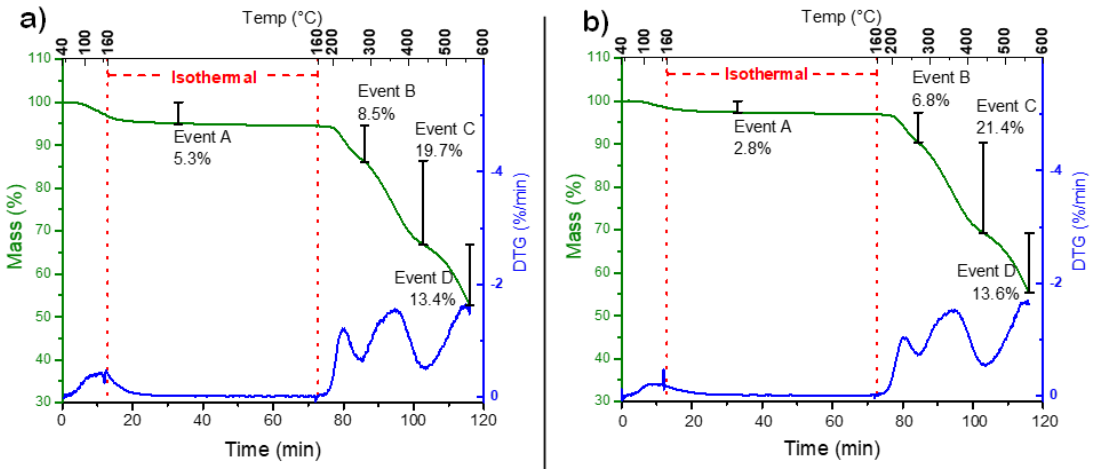


**Figure 19 – NiETT thermogravimetric analysis with plotted differential (DTG) for (a) Pristine Powder or PP samples and (b) Annealed Powder or AP samples.**

In both the pristine and annealed powders, Event A is a broad, shallow loss (5.3% and 2.8% in PP and AP, respectively) that begins at 70 °C and ends during the isothermal hold, and ion traces from mass spec reveal that two components are evolved – water and carbonyl sulfide – that contribute to the total mass loss. The presence of water is expected as it has been previously observed in literature for NiETT.[66] The water evolved at these temperatures is hypothesized to be contact moisture; the heating rate (10 K/min) prevents differentiation between water removed at or below the boiling point (surface or contact

moisture) and water removed above the boiling point (incorporated water, such as $NiSO_4 \bullet 6H_2O$ or $Ni(OH)_2$ or coordinated to the polymer backbone).[91,92] The other signal, carbonyl sulfide, is an unexpected impurity when considering the ideal atomic composition $Na[Ni(C_2S_4)]_n$ for these polymers. The source of this signal is potentially from unreacted carbonyl end groups or sulfonyl irregularities in the polymer backbone, as was discussed in chapter 2.[93] Even in carefully controlled syntheses, impurities and deviations from the idealized structure have been shown in these ETT polymers.[23,66,67,76] The key difference between the two samples is that the signal from carbonyl sulfide is significantly reduced in the annealed powder when compared to the pristine material, such that contact moisture is the major contributor to the 2.8% mass loss in the annealed powder sample. This highlights the importance of proper reaction and work-up conditions as well as material post-treatment as removing a small amount of impurity (carbonyl sulfide) increases the thermopower from –28 to –42 μV/K.

Event B in both **PP** and **AP**, begins the irreversible and destructive decomposition of the NiETT polymer. The onset temperature (180 °C) is recommended as the maximum safe temperature for any processing method (*e.g.* annealing, printing, extruding) for the NiETT. Event B evolves additional water (likely incorporated water) and carbonyl sulfide, and begins the release of sulfur dioxide and carbon disulfide. The presence of sulfur dioxide provides additional evidence of sulfonyl groups in the backbone, as it is evolved at a lower temperature (200 °C) than sulfur dioxide from $NiSO_4$ decomposition.[94] The start of evolution of carbon disulfide indicates that the main backbone of NiETT is decomposing at these elevated temperatures. Event C is a continuation of Event B, and releases additional carbon disulfide, hydrogen sulfide, and sulfur dioxide. The final decomposition, Event D,

continues to the end of the run at 600 $^{0}$C releasing carbon disulfide, sulfur dioxide, hydrogen sulfide and water. Based on these observations from TGA-MS, it is clear that annealing causes a change in the chemical composition of the polymer, which manifests as an enhancement in the thermoelectric properties.

Extending the analysis to films, Figure 20 shows the TGA curves for two film samples: a NiETT/PVDF film cast from DMSO (Pristine Film, **PF**) and a NiETT/PVDF film cast from DMSO that is annealed at 160 °C in air for one hour (Annealed Film, **AF**). As in the powder samples, the films show four mass loss events, denoted Events A-D.

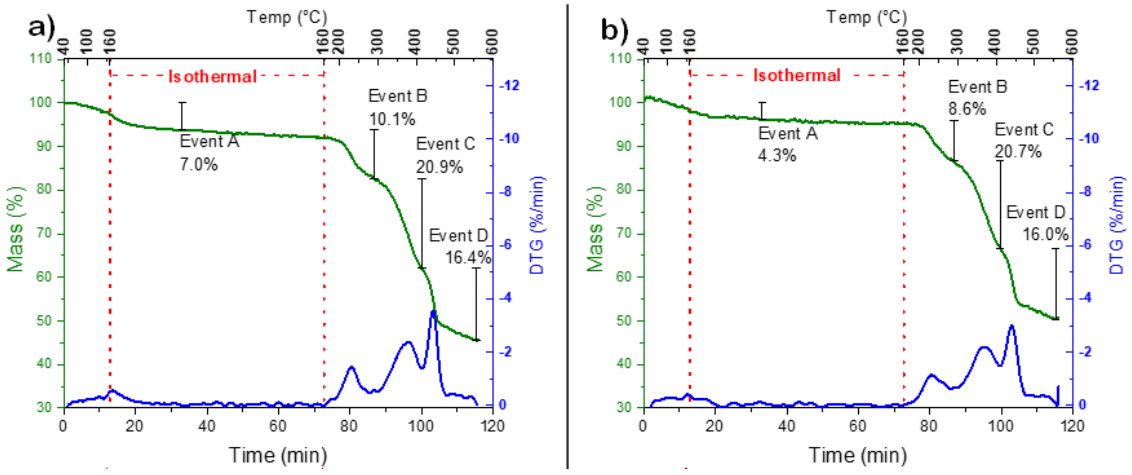


**Figure 20 – Thermogravimetric analysis with plotted differential (DTG) for NiETT/PVDF/DMSO composite films (a) Pristine Film or PF samples and (b) Annealed Film or AF samples.**

For both film samples, Event A represents the annealing process, and is crucial for understanding the origin of enhanced thermoelectric properties. Event B (206 – 266 °C) and Event C (346 – 438 °C) are the major NiETT decomposition events that occur after annealing that are similar to the powder samples, confirming that this is the NiETT polymer backbone decomposition. Event D (440 – 487 °C) occurs at a lower temperature in the films that is consistent with the decomposition onset of PVDF.

In the pristine film or PF, the mass loss in Event A totals 7.0% and shows a very weak signal of water and almost no signal of carbonyl sulfide when compared to the powder samples. The most prominent mass loss signal during this step is from DMSO, which is the solvent that the films are cast from. In contrast, in the annealed film or AF, the mass loss is smaller (4.3%), with no discernable water or carbonyl sulfide signals and a reduced signal coming from DMSO. Less surface moisture is expected to return to film samples compared to the powder samples upon exposure to atmosphere as the hydrophobic PVDF surrounding the NiETT particles in the films prevents reabsorption of water. Although vacuum drying films at 50 °C for 30 minutes, and annealing for one hour at 160 °C does not fully remove DMSO from the composite films, the changes are sufficient to enhance thermoelectric performance. This suggests that the process of removing DMSO from the film helps drive the film reorganization, which manifests as a boost in electrical conductivity. Thus, by annealing NiETT/PVDF composite films at 160 $^{0}$C, impurities such as water and carbonyl sulfide are removed from the polymer backbone, and DMSO removal densifies the film. These synergistic effects manifest as a simultaneous enhancement in the conductivity and thermopower of ETT films, while also providing insight into the chemical composition of this polymer. Thermoelectric data presented in the remainder of this chapter is for films that are annealed at 160 $^{0}$C in air for one hour. In-depth analysis of the effects of annealing are reported in a recently submitted manuscript.[95]

### *3.2.2 Synthesis Modifications for Optimized Reactions*

In addition to post-treatment processes such as annealing, the synthesis of NiETT can also be tuned (see Figure 14) to create further enhancements in the thermoelectric properties. One such effort was presented in chapter 2 (changing the extent of oxidation by

controlling the air exposure time), and the following sections outline a comprehensive investigation of each sub-step in the reaction scheme.

#### 3.2.2.1 Changing the Counterion

The choice of (*i*) alkali counterion, (*ii*) nickel stoichiometric equivalents, and the (*iii*) extent of oxidation all impact thermoelectric performance. First, we examine the effect of changing the counterion; it is well-known that bulky counterions such as tetraethylammounium can reside between polymer chains and impede charge transport. Alkali counterions are preferred as their small size allows for close-packing of the polymer chains, thereby facilitating inter-chain interactions.[23,66] The thermoelectric properties of NiETT can be tuned by changing the counterion, as shown in Figure 21. The thermopower of all three variants is negative, confirming that n-type electrical transport is dominant. Interestingly, the electrical conductivity increases and the thermopower decreases with decreasing counterion size; Li[NiETT] with the smallest counterion has the highest conductivity at 37 ± 1 S/cm, while K[NiETT] has the highest thermopower at -99 ± 8 μV/K. The power factor is highest for Na[NiETT] films at a value of 13 ± 2 μW/m-K$^2$ due to the combination of a moderate conductivity and Seebeck coefficient (23 ± 1 S/cm and -74 ± 3 μV/K). This is in contrast to what has been reported for ETT pellets where K[NiETT] showed superior thermoelectric properties.[23] These differences can be attributed to the fact that the reactions conditions as well as reactant purity in each step dictate the final material performance. The alkali ion composition is consistent across all syntheses at 0.6-0.8 at. % or one counterion per 10-15 nickel centers.

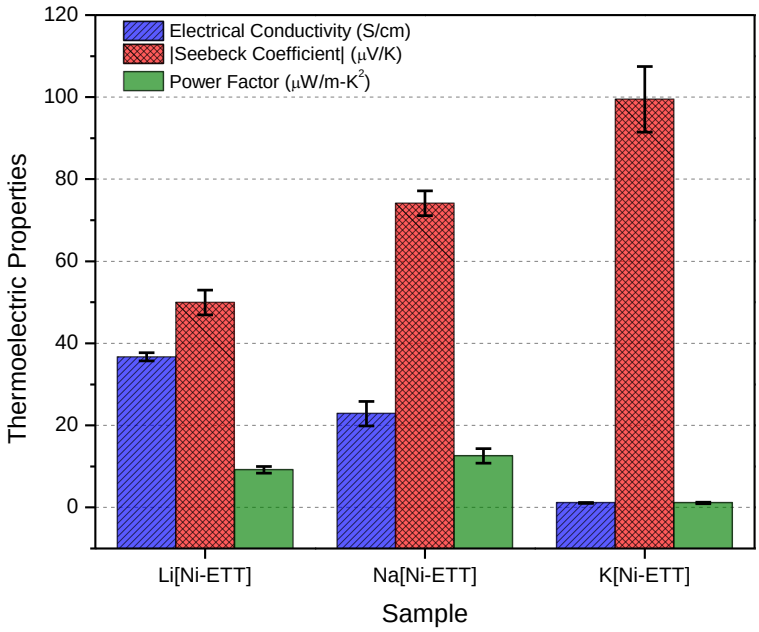


**Figure 21 – Thermoelectric performance of NiETT with different alkali metal counterions. Na[NiETT] shows the highest thermoelectric properties with a power factor of 13 μW/m-K$^2$.**

The marked difference in thermoelectric performance, despite similar composition and oxidation extent, supports two hypotheses: (*i*) the counterion affects the reaction pathway and produces a different final material beyond simply exchanging the counterion; and/or, (*ii*) a property of the counterion, even at one counterion per 10-15 nickel centers, directly affects NiETT's intra- and inter-chain interactions. XPS analysis of sulfur in the three polymers shows different binding environments across the samples; the S2p peak can be deconvoluted into two main binding environments at 161.5 eV and 163.5 eV (see Appendix A.3) and the ratio of these peaks differs across all three samples. These differences in the sulfur atoms may affect charge delocalization along the polymer backbone and indicate that the identity of the counterion plays a role in changing the thermoelectric properties. From the S2p scan, the presence of oxidized sulfur compounds for Li[NiETT] is observed at higher binding energies (~168 eV), that corresponds with an

increase in the amount of oxygen in its elemental composition. The Ni2p peaks remain unchanged through varying the counterion, and this may be indicative of a ligand-centered oxidation for these complexes.[96]

#### 3.2.2.2 Changing the Equivalents of Ni(II)

In step 2, the stoichiometric equivalents of the nickel(II) salt are varied using $Na_0$[Ni(1.0)ETT] as the control material to identify the optimum equivalence under these reaction conditions. It has been claimed that excess nickel can produce Ni[NiETT] where it co-acts as a counterion with alkali metals;[23] an alternative hypothesis is that excess nickel acts as a detrimental impurity in the final material. Using anhydrous nickel(II) acetate, which was chosen due to the ease of obtaining the anhydrous salt and its solubility in methanol, removes any uncertainty around the molar mass of the hydrate and the effect on the reaction from hydrated nickel(II) species. The resulting thermoelectric properties are shown in Figure 22, and this indicates that a power factor enhancement up to 23 μW/m-$K^2$ is achieved by lowering the amount of nickel(II) to 0.75 equivalents. To understand the effect of changing the amount of Ni, the % Ni incorporation is calculated in these polymers to quantify how much of the $Ni(OAc)_2$ is present in the NiETT backbone (see Appendix A.4). The higher percent incorporation is found in the sub-stoichiometric nickel equivalents, with 80% incorporation for Ni(0.75) compared with 40% incorporation for Ni(2.0). Impurities in the TPD monomer (depending on the source) or degradation during reaction Step 1 is hypothesized to result in less than 100% nickel incorporation, with the optimum level of nickel therefore being sub-stoichiometric. Furthermore, XPS analysis of the Na[NiETT] powders reveal that excess nickel(II), as in the case of Na[Ni(2.0)ETT],

forms secondary products, as observed in the Ni and S elemental scans. These impurities are present in lower amounts in the stoichiometric and sub-stoichiometric equivalents.

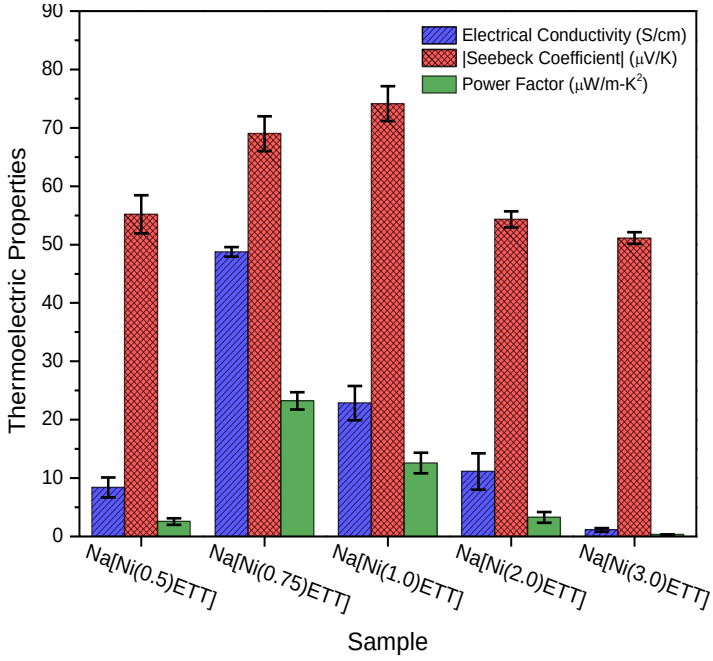


**Figure 22 – Thermoelectric performance of NiETT with stoichiometric variants of nickel(II) acetate. A sub-stoichiometric amount of Ni, *i.e.*, 0.75 equivalents, yields a power factor of 23 μW/m-K² for Na[NiETT].**

Given that the overall XPS signal may originate from multiple Ni species in a small binding energy range, the identification of specific compounds is not straightforward. Nonetheless, it is clear that $Ni^{2+}$ is the formal oxidation state across all samples with the peak at 853.4 eV corresponding to the primary Ni-S binding environment. At 855.5 eV, Ni is coordinated with oxygen; the full-width at half-maximum is broad and is attributed to a composite peak of $Ni(OH)_2$ and $NiSO_4$ or other oxidized sulfur species coordinated to nickel (secondary products).[93,97] This also explains the presence of hydrogen and oxygen in the elemental analysis despite using anhydrous starting materials and working under inert conditions. This is contrary to what has been speculated previously about the peak at 855 eV corresponding to excess nickel acting as a counterion.[23] Doubling the equivalents

of nickel does not lead to the formation of Ni[NiETT] as there is the same atom percent of sodium counterion present in both Na[Ni(1.0)ETT] and Na[Ni(2.0)ETT]. This may be in part due to the controlled iodine oxidation during reaction Step 3, thereby eliminating any nickel acting as a counterion. A low intensity satellite peak ~6 eV to the right of the main peak (~ 860 eV) confirms that the nickel center exists in a square-planar coordination environment[98] (see Appendix A.4). The ratio of the two Ni peaks changes across the samples – as the equivalents of nickel increases, the peak at 855 eV is intensified, indicating the formation of more secondary products that is consistent with the nickel incorporation amounts discussed earlier.

The S2p spectra reveals sulfur in two chemical environments instead of the single Ni-S-C binding environments that is expected for an infinitely long chain of NiETT. Deconvolution results in peaks at 162 eV and 163.5 eV with the former corresponding to the expected polymer backbone and the latter reflects the influence of ligand acting as end groups.[99] This however suggests a low value for the degree of polymerization for end groups to have this pronounced effect. An alternate explanation for the presence of different sulfur binding environments is the existence of ligand in two different oxidation states, as has been reported for $Ni(dmit)_2$.[100] By changing the nickel(II) equivalents added in the synthesis, the ratio of ligand in these two oxidation states is varied as shown in Figure 23 and in Table 4, which in turn affects the thermoelectric properties. A similar observation has been made for p-type CuETTs and confirms a ligand-based oxidation mechanism in these metal-organic complexes.[70] At higher binding energies ~168 eV, there is an additional peak in the S2p spectra which corresponds to oxidized sulfur species such as $SO_x$. This suggests that upon exposure to air before chemical oxidation, some of the Ni-S

is oxidized to an oxy-sulfur species in the material as evidenced by the presence of $NiSO_4$ in the Ni2p spectra for all samples.

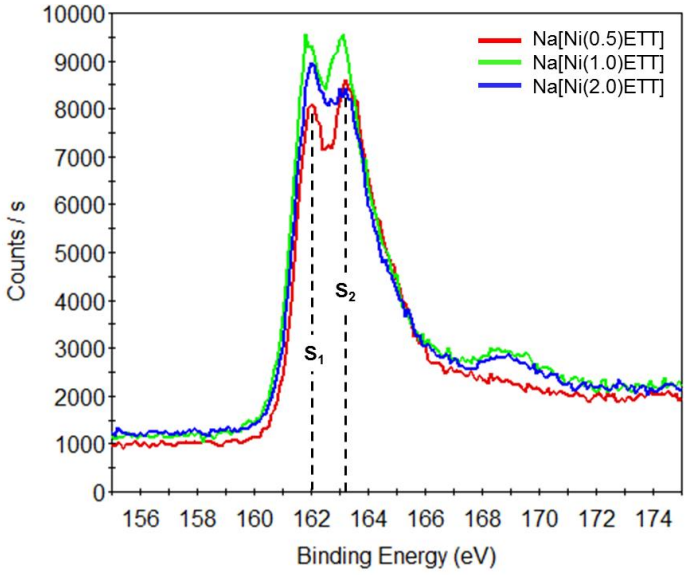


**Figure 23 – XPS analysis of Na[Ni(Y)ETT] based on different nickel equivalents (Y) showing the presence of three different binding environments for sulfur across all samples.**

**Table 4 – S2p main peak deconvolution into two sub-peaks for different nickel equivalents**

| Sample | $S_1$ (162 eV) [Atomic %] | $S_2$ (163.5 eV) [Atomic %] | $S_2/S_1$ |
|---|---|---|---|
| Na[Ni(0.5)ETT] | 51.8 | 37.4 | 0.72 |
| Na[Ni(1.0)ETT] | 54.3 | 33.5 | 0.62 |
| Na[Ni(2.0)ETT] | 57.9 | 29.7 | 0.51 |

### 3.2.2.3 Changing the Extent of Oxidation

As a final step, the effect of oxidation with iodine was investigated to understand the extent to which thermoelectric properties could be tuned by controlling the oxidation state and thus doping level of the polymer. For this, every attempt was made to prevent the

ligand, prepared in situ, from being oxidized until the iodine addition step by handling under an inert atmosphere (argon) using standard Schlenk techniques. Most previous literature reports[23,66] claim the polymer does not precipitate until air is introduced as an oxidant. However, one previous report[67] shows that the polymer precipitates upon addition of the metal salt without any external oxidant. It has also been claimed that even by working under careful anaerobic conditions, there is some unintended oxidation that causes the polymer to precipitate.[64] The observations made herein are contradictory to these previous reports, as the reaction intermediately forms a sol-gel (see Figure 15) during Step 2 of the reaction. Furthermore, the rigorous air-free reaction conditions used, the observable consumption of iodine during reaction Step 3, and limited oxidized S2p species indicate that unintended oxidation is not the cause of the precipitate or sol-gel formation prior to oxidation. Rather, higher molecular weight species (either branched or linear) are possibly forming in reaction Step 2 and increasing the reaction viscosity.

Even without the addition of any iodine, the "unoxidized" polymer is unobtainable as it oxidizes on exposure to air during work-up (filtering and drying) and film fabrication. These workup conditions make $Na_2$[NiETT] an analog to an air-oxidized species moreso than a truly unoxidized sample. Under these conditions, the electrical conductivity for $Na_2$[NiETT] is 37 ± 3 S/cm while the thermopower shows the lowest value for this family at –36 ± 2 μV/K. The elemental composition shows approximately two sodium atoms per five nickel atoms, indicating a more negative charge on the backbone compared to one sodium atom per ten nickel atoms in the fully oxidized $Na_0$[NiETT]. Upon addition of iodine in Step 3 of the reaction, electrons are extracted from the polymer backbone, which leads to a reduction in electrical conductivity and a simultaneous improvement in the

thermopower as shown in Figure 24. This *S*-$\sigma$ tradeoff is analogous to extrinsically doping a polymer and shows that NiETTs can have their oxidation level tuned during synthesis to give desired values for *S* and $\sigma$.

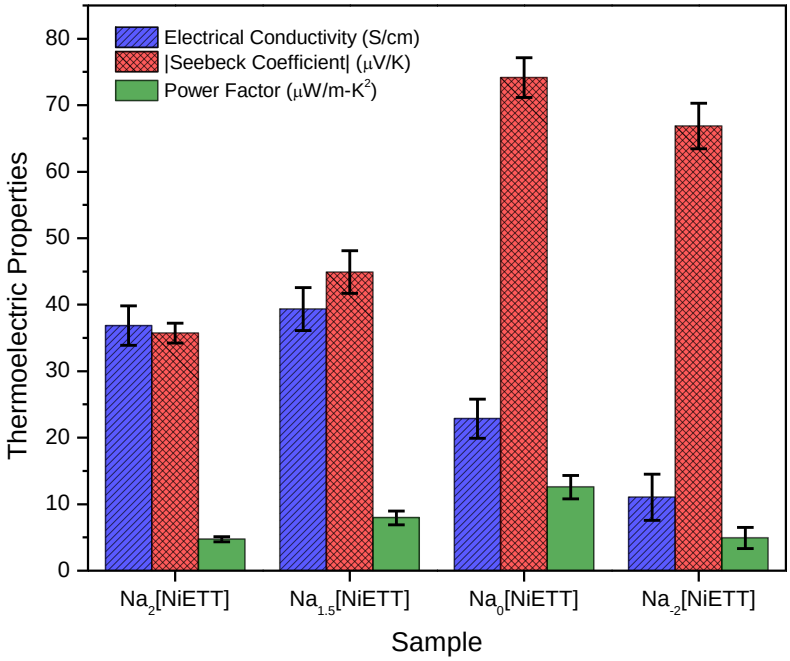


**Figure 24 – Thermoelectric performance of NiETTs as a function of chemical oxidation equivalents using iodine.**

Given the poor XPS signal-to-noise ratio for $Na_2$[NiETT], it is challenging to extract any noticeable changes in the Ni binding environment. However, a striking difference appears in the S2p spectra between this sample and one that is fully oxidized with iodine (Appendix A.3). For this "unoxidized" sample, the $SO_x$ peak is more prominent than the main Ni-S peak, which may indicate the formation of more side products. This is also consistent with the results in chapter 2 on air-oxidized ETTs at short exposure times that yield similar thermoelectric properties.[76] The use of air as an oxidant results in thermoelectric properties of NiETT that vary significantly and this may explain challenges with material reproducibility in the literature. The use of iodine provides greater control of

the oxidation step; other oxidizing agents in future studies may enable greater tunability of $S$ and $\sigma$ and a deeper insight into the charge transport in these materials. This iterative refinement avoids batch-to-batch variations and results in a high n-type power factor (> 20 μW/m-K$^2$) for NiETT/PVDF composites that can be printed into devices that are stable in ambient conditions.[101]

### *3.2.3 Charge Transport in NiETT/PVDF Films*

Temperature dependent $S$ and $\sigma$ measurements were performed to elucidate the charge transport mechanism in Na(NiETT), as shown in Figure 25. Fitting the temperature dependent data to Mott's variable range hopping model yields a linear fit for a 3D system, as was seen for K(NiETT)/PVDF films (see Figure 13). However, this fit is not unique to VRH; percolation mechanisms also show a similar power law conductivity dependence, which may be a more accurate description of charge transport in NiETTs due to sample inhomogeneity.

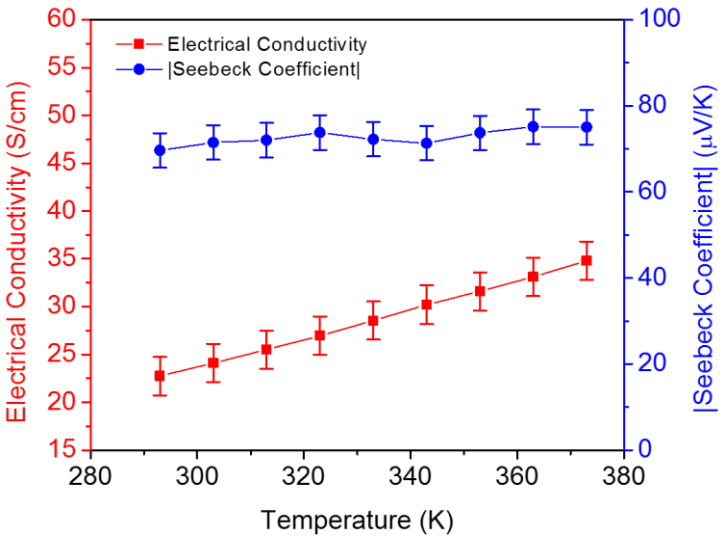


**Figure 25 – Temperature dependent thermoelectric properties of Na(NiETT) films are indicative of thermally-activated hopping transport.**

### *3.2.4 Enabling N-Type Organic-Inorganic Composites*

The development of an n-type polymer that is stable in ambient conditions and has a high electrical conductivity (> 20 S/cm) opens avenues to investigate organic-inorganic composites. These materials are interesting as they leverage the low thermal conductivity of the organic constituent and the high Seebeck coefficient of the inorganic material. This results in a high-performance composite material that maintains its solution processability and can be printed into low cost devices for energy harvesting. While this has been accomplished with p-type polymers,[15,39] n-type composites have remained largely unexplored due to the lack of n-type polymers that are moderately electrically conducting (> 10 S/cm).

Given the performance enhancement achieved with NiETT/PVDF films, a preliminary effort was undertaken to evaluate adding ball-milled bismuth telluride to these composite films. First, a commercially available n-type $Bi_2Te_3$ ingot was ball-milled for four hours into micron-sized particles and rinsed with 5 wt.% hydrochloric acid to remove the native oxide layer on the surface of the particles as ball-milling was not performed in an inert environment. $Bi_2Te_3$ was then dispersed in PVDF/DMSO and cast into a film showing a conductivity 0.2 S/cm and a thermopower of -230 μV/K. The low electrical conductivity of the $Bi_2Te_3$ film can be attributed to incomplete removal of the oxide layer; however, this is not a concern given that the goal of forming composites was to leverage the thermopower of the inorganic constituent. To enhance the electrical conductivity, increasing amounts of NiETT powder were added to the dispersion and the resulting films were annealed at 160 °C in air for an hour. Figure 26 shows the thermoelectric properties of NiETT/$Bi_2Te_3$ composite films in PVDF/DMSO.

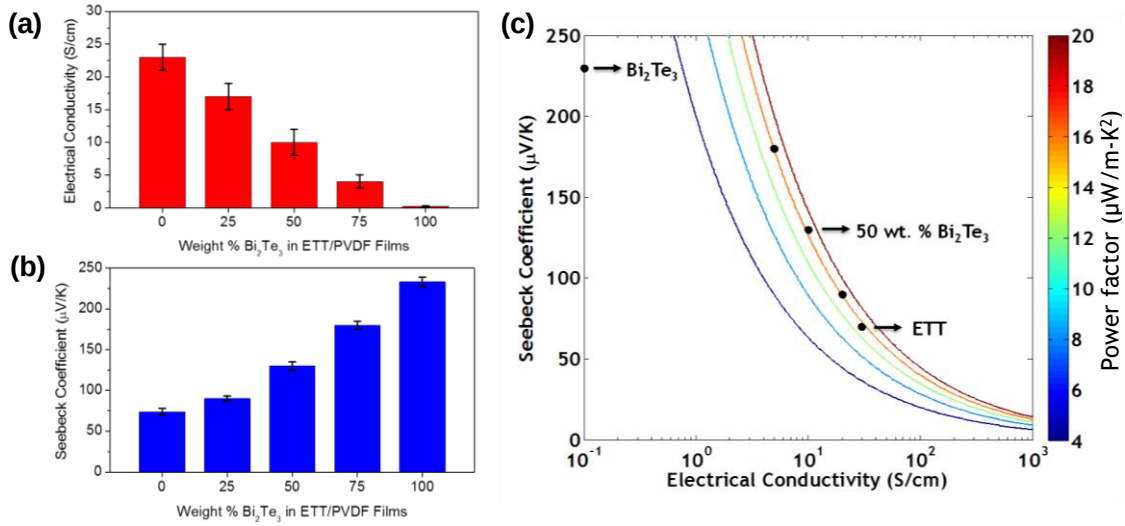


**Figure 26 – (a) Electrical conductivity, (b) Seebeck coefficient, and (c) power factor contours (see color bar) on an *S*-$\sigma$ plot for $Bi_2Te_3$/NiETT/PVDF composite films.**

It is evident that as more $Bi_2Te_3$ is present in the film, the Seebeck coefficient increases, albeit at the cost of a lower electrical conductivity in these organic-inorganic composites. Surprisingly, the composite film maintains a high electrical conductivity of 10 S/cm and a Seebeck coefficient of -130 μV/K when equal amounts of NiETT and $Bi_2Te_3$ are present. This is primarily attributed to the conducting nature of the NiETT polymer which forms a percolation network, and this shows that the organic component is critical in achieving high electrical conductivity in printable n-type composites. The power factors for all cases remain the same, indicating that these films form simple composites that follow Effective Medium Theory.[102]

## 3.3 Conclusions

Difficulties in the synthesis, purification, and characterization of NiETT due to its insolubility have resulted in challenges with repeatable thermoelectric properties. In this chapter, I have shown that by undertaking a systematic investigation of the reaction sub-

steps, the properties can be enhanced and measured reproducibly. First, I showed that the annealing can be used as a post-treatment process to simultaneously enhance the electrical conductivity and thermopower of NiETT/PVDF composite films. Spectroscopic characterization reveals that the underlying mechanism involves removal of residual solvent and impurities (specifically water and carbonyl sulfide) from NiETT/PVDF films. Additionally, microscopic characterization reveals morphological changes caused by a densification of the film that improves chain packing. These effects resulted in a 25x improvement in power factor of NiETT/PVDF films compared to literature, while also providing insight on the composition of the ETT.

Next, synthetic modifications were made to further improve the thermoelectric performance. It was demonstrated that the choice of counterion, even within the alkali metals, affects the polymer conductivity and thermopower. By varying the equivalents of nickel, impurities and unintended oxidation processes associated with excess nickel were identified, with sub-stoichiometric nickel equivalents (0.75 equivalents) providing the highest performance materials. XPS provides strong evidence, for the first time, that the oxidation process in NiETTs is ligand-centered. By performing the synthesis with a controlled, measurable chemical oxidant (*i.e.*, iodine) uncertainties and impurities caused by air oxidation were eliminated, which addresses a concern raised in chapter 2. Overall, this has enabled a systematic understanding of the synthesis steps and its effects on $\sigma$ and $S$, resulting in a thermoelectric power factor of 23 $\mu W/m\text{-}K^2$ for n-type, air-stable NiETT/PVDF films. Furthermore, a preliminary investigation of n-type organic-inorganic composite films was presented for the first time yielding a printable NiETT/$Bi_2Te_3$ ink with a conductivity of 10 S/cm and a thermopower of -130 µV/K.

# CHAPTER 4. THERMOELECTRIC DEVICE DESIGN: RADIAL TEG FOR POLYMERS

The progress in high performance polymer-based materials motivates the development of thermoelectric devices for energy harvesting applications. While power factor (and consequently *zT*) is important to quantify material performance, for waste-heat recovery applications, power density is crucial rather than efficiency since heat is abundant and often free. Furthermore, high power density at a low cost is the defining metric since polymers are widely available and can be processed from solution for large-scale applications. Despite these advantages, organic TEGs have not had significant impact owing to relatively low power densities ($nW/cm^2$ - $\mu W/cm^2$) for device architectures reported in literature.[14,16,23,63,103] Furthermore, the use of heat exchangers to actively cool the device on the cold-side increases the cost significantly and offsets the benefits of the low material and manufacturing cost offered by polymers.[23,73,104] This necessitates the design of new device architectures that are tailored for polymers.

In this chapter, a novel radial thermoelectric generator is presented that leverages the inherent advantages offered by polymers. In this geometry, disks are stacked co-axially such that heat transfer is radial through the active material. A theoretical framework is presented that yields the first closed-form analytical expressions for *(i)* the leg length that maximizes power density, and *(ii)* a geometry matching condition that reflects the inherent relationship between device geometry and material properties.[105] These simple analytical expressions are accurate in the limit of small *zT*, where the Peltier effect is small and the device can be modeled from a thermal perspective alone (this approximation is reasonable

for polymers demonstrated in literature with $zT < 0.5$). Another major advantage of the radial geometry for polymers is that these devices can be operated under natural convection alone due to heat spreading. This is primarily because of the low thermal conductivity of polymers that results in a characteristic thermal length ($L_T$) of a few centimeters. The numerical model predicts a power density of ~1 mW/cm$^2$ using state-of-the-art polymer materials; this is three orders-of-magnitude higher than current polymer prototypes based on the conventional flat-plate geometry. Furthermore, electrical interconnect and contact resistances are minimized because of the large cross-sectional area on the face of the disk, which addresses a major drawback with existing polymer prototypes. As a proof-of-concept, a radial prototype is also presented, with NiETT as the n-type material and hybrid Te nanowires in PEDOT:PSS as the p-type material.[106] This polymer-based radial device has applications in heat recovery from hot water pipes at potentially lower $/W costs.

### 4.1 Limitations of Existing Polymer Prototypes

Most TEGs have been designed with the traditional flat-plate geometry; with leg length $L$ and fill factor $F$ being dominant design parameters. Fill factor is the ratio of the area covered by the active thermoelectric material to the hot-side heat exchanger area, $A$ (this is often the area of the ceramic plate), as illustrated in Figure 27. For high power densities, legs should be close-packed and the cross-sectional area of each leg should be decreased, which is ultimately limited by manufacturing processes. The leg length must then be reduced to keep Joule heating to manageable levels, forcing $L$ to approach the thin-film limit (<50 μm). In this situation, it is difficult to maintain a large temperature difference across the device, which then reduces the power density. Active cooling (*e.g.*, using a fan) can increase the power output but also contributes to increased device cost and

a parasitic reduction in power density of the system, resulting in a trade-off between the thermal-electrical performance and cost. Furthermore, at this thin-film limit, the electrical interconnect and contact resistances become a significant portion of the total resistance, which has been another factor for the low power density in previous polymer TEG prototypes.[14,23,63,103]

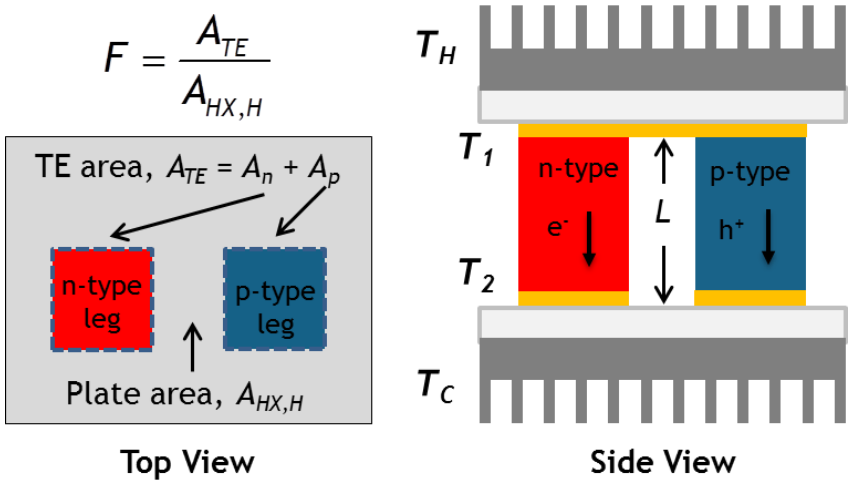


**Figure 27 – Schematic of a conventional flat-plate TE device showing the fill factor, *F*. The n- and p-type materials (shown in red and blue respectively) are connected electrically in series with a metal (shown in orange) and thermally in parallel between electrically insulating ceramic plates (shown in off-white). $T_H$ and $T_C$ correspond to the fixed hot-side and cold-side temperatures; $T_1$ and $T_2$ represent the junction temperatures. *L* is the thermoelectric leg length.**

Several organic TE prototypes have been demonstrated; Bubnova *et al.* demonstrated a 54-couple (comprising one p- and n-type leg) device consisting of p-type PEDOT-Tos and a blend of tetrathiafulvalene-tetracyanoquinodimethane (TTF-TCNQ) with polyvinylchloride as the n-type material.[18] Photolithography was used to create cavities for the active material, resulting in a power density of 24 nW/cm$^2$ at $\Delta T$ = 10 K. Another prototype consisted of 35-couples of poly[Cu(CuETT)] and poly[Na(NiETT)] pressed into pellets as the p-type and n-type materials respectively. With active cooling,

this device generated a power density of 1.2 μW/cm$^2$ at $\Delta T$ = 30 K; however, this does not account for the power input used for active cooling, which is likely more than the output of the device.[23] More recently, Toshima *et al.* demonstrated a 5-couple device composed of a hybrid of poly[K(NiETT)] with carbon nanotubes and polyvinyl chloride on polyimide. With active cooling, a maximum power of 3.88 μW was obtained at $\Delta T$ = 100 K;[73] the power density is estimated to be ~400 μW/cm$^2$ without considering the penalty for active cooling. For these devices reported in literature, drawbacks include the use of: microfabrication techniques which are expensive and time-consuming, active cooling, which may consume more power than is generated, and infusible materials that are not amenable to solution processing. Thus, the major challenge has been the development of high power density polymer-based devices that can fabricated at a low cost and on a large-scale. This has been the other focus area of my research, and the subsequent sections present the new devices that I have designed.

## 4.2 Towards a Radial Architecture

To determine a new architecture appropriate for polymers, the design variables, $F$ and $L$ are considered. It has been shown that the optimum fill factor from a $/W minimization standpoint is $F > 1$ for polymer devices that are cooled by natural convection, indicating that heat spreading is important.[107] One embodiment of this is a flat-plate device with tapered legs where the cross-sectional increases from the hot-side to the cold-side, and another manifestation is a cylinder where the hot-side is a line source (of finite radius) along the central axis and the cold-side is the outer surface of the cylinder at a larger radius. Figure 28 facilitates the comparison of flat-plate and radial fill factors.

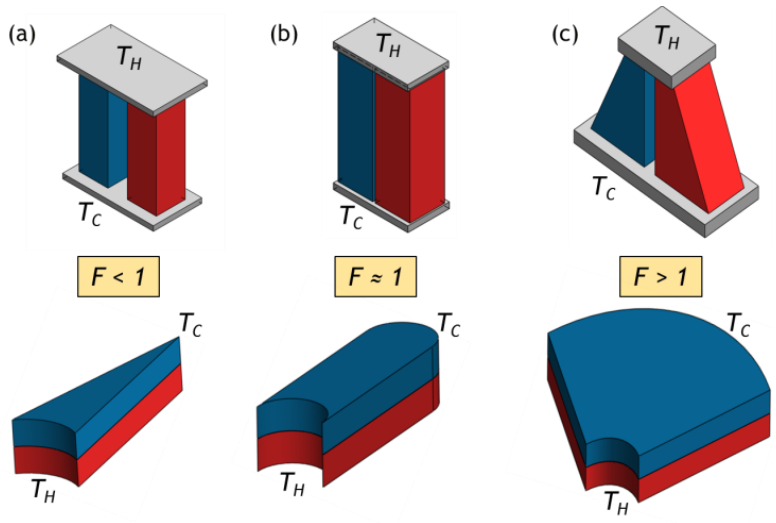


**Figure 28 – Representation of different fill factors, $F = A_{TE}/A_{HX,H}$ for flat-plate and radial devices. The n- and p-type material are shown in red and blue. (a) Heat is concentrated when the area of the thermoelectric material is less than the hot-side resulting in $F < 1$, (b) The fill factor is unity when the areas of the thermoelectric material and hot-side are matched, and (c) Heat spreading occurs when the area of the thermoelectric material is more than the hot-side area with $F > 1$.**

Radial thermoelectric devices have been explored previously, such as a ring-structured module with p- and n-type $Bi_2Te_3$ alloys.[108] The tube-shaped device produced a power output of 33 mW at $\Delta T$ = 70 K maintained across the inner and outer surfaces,[108] with an estimated power density of ~10 mW/cm$^2$. Another demonstration was a TEG based on radially patterned gold and nickel legs, where a power output of 0.8 μW was obtained using a 470 K hot gas stream,[109] with an estimated power density of ~5 μW/cm$^2$. These devices highlight the advantages of a different geometry but may not be practical for large-scale applications owing to material and manufacturing costs associated with inorganic materials and their processing limitations. In contrast, the solution processability of polymers enables their application in the radial architecture. The radial design consists of p- and n-type polymers on a thermally insulating substrate, co-axially stacked around a hot pipe to realize a cylindrical geometry. Separators are added to electrically isolate adjacent

disks and vias provide current pathways (radially through the p- and n-type and axially through the substrates and separators) for electrical series connections, as illustrated in Figure 29. In this configuration, the inner pipe serves as the hot-side heat exchanger while the outer surface of the stacked disks is the cold-side heat exchanger resulting in $F = r_{out}/r_{in} > 1$. As a result, heat is spread radially outward allowing for natural convection to cool the device because the heat flux on the outer surface is lower than that on the inner surface. This thereby eliminates the need for active cooling and can result in higher power densities and lower manufacturing costs.

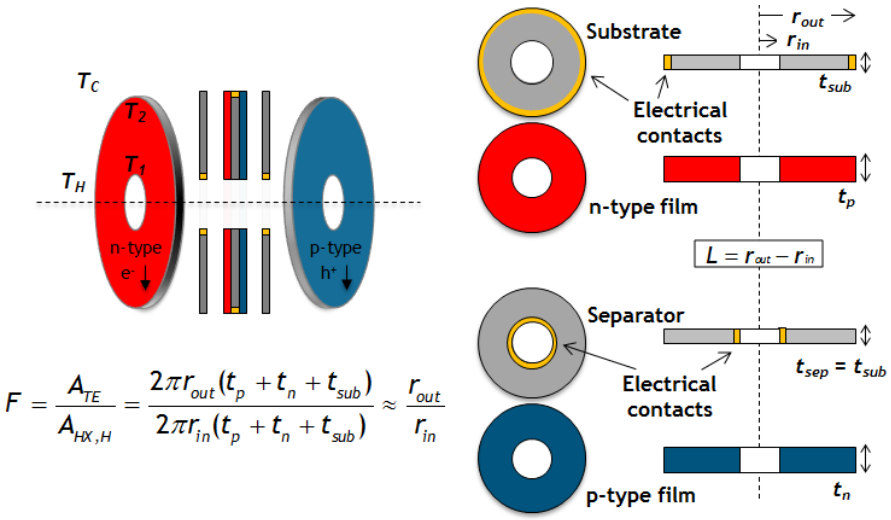


**Figure 29 – Schematic of radial TEG device. The n- and p-type polymers are printed onto circular disks such that they are connected electrically in series and thermally in parallel. $T_H$ and $T_C$ correspond to fixed hot-side and cold-side temperatures. $T_1$ and $T_2$ represent junction temperatures, and $L$ is the leg length (difference between the outer and inner radii). The fill factor is approximated in the limit where the substrate is absent or has a negligible thickness compared to the thermoelectric material.**

### 4.3 Radial TEG Analytical Heat Transfer Model

In the subsequent sections, I have derived closed-form analytical expressions for different leg lengths ($L = r_{out} - r_{in}$) that maximize heat flux and power density for a high-performance device by considering heat exchanger contributions. The performance-

optimization in this chapter provides the first analytical design framework for a radial TEG operating under natural convection.

### *4.3.1 Analytical Model – Device Physics*

To obtain the optimized performance for a radial TEG, the device physics of a flat-plate generator was investigated using existing heat transfer models. Figure 30 shows the equivalent thermal circuit of a conventional flat-plate TEG, where $T_H$ represents the temperature of the hot-side heat exchanger, $T_1$ and $T_2$ are the thermoelectric junction temperatures, and $T_C$ is the temperature of the cold-side heat exchanger.[107,110-112] The thermal conductance through the active material, $K_{TE}$, and that of the hot- and cold-side heat exchangers, $K_H$ and $K_C$, respectively, strongly influence the device performance. Performing an energy balance at each junction, heat flowing through the hot-side is:[3]

$$Q_H = K_T\left(T_1 - T_2\right) + \left(S_p - S_n\right) I T_1 - I^2 R_T / 2 = K_H\left(T_H - T_1\right) \tag{5}$$

where $K_T$ is the sum of $K_{TE}$ and a parallel thermal leakage conductance $K_{||}$ (consists primarily of conduction losses through the substrate and separator, but can also include convection and/or radiation contributions between the hot-side and cold-side heat exchanges if they exist), $S_p$ and $S_n$ are the Seebeck coefficients of the p- and n-type material, $I$ is the electric current, and $R_T$ is the internal electrical resistance of the module (including the contact and interconnect resistances). Similarly, heat flowing out of the cold-side is:

$$Q_C = K_T\left(T_1 - T_2\right) + \left(S_p - S_n\right) I T_2 - I^2 R_T / 2 = K_C\left(T_2 - T_C\right) \tag{6}$$

where the first, second, and third terms in the summation represent Fourier heat conduction, the Peltier effect, and Joule heating, respectively. This thermal circuit is also applicable for a radial TEG with a modification of the thermal conductance and electrical resistance terms for the active thermoelectric material.

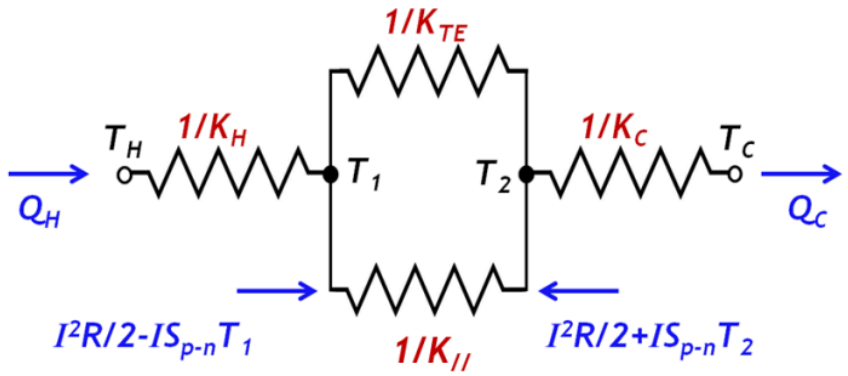


**Figure 30 – Thermal circuit representation of a thermoelectric device. The analysis is conducted for constant hot- and cold-side temperatures, $T_H$ and $T_C$ with corresponding heat exchanger conductance $K_H$ and $K_C$. There are two thermal conductance terms between the junction temperatures $T_1$ and $T_2$ representing heat transfer through the legs ($K_{TE}$) and a parallel leakage ($K_{||}$). The internal heat generation term, $I^2R/2$, is the Joule heating component; the Peltier term is $IS_{p\text{-}n}T$.**

To proceed with the analytical model, the following simplifying assumptions are made that are also common to other TEG analyses[107,110,113]: *(i)* electrical and thermal contact resistances, and interconnect resistances from the substrate and separator are negligible, *(ii)* $K_{||}$ is small as substrate and separator contributions are negligible and operating temperatures are very close to ambient, which reduces the effects of radiative transfer, and *(iii)* the temperature dependence of $S$, $\sigma$ and $k$ is neglected and all properties are evaluated at a mean temperature (*i.e.*, $T_m = (T_H + T_C)/2$). These approximations are valid in most applications and are useful algebraic simplifications that give $R_T \approx R_{TE}$ and $K_T \approx K_{TE}$ in the preceding two equations. Under these approximations, the power generated by a radial TEG is given by:[3]

$$P = \left( \frac{m}{(1+m)^2} \right) \frac{(S_p - S_n)^2 (T_1 - T_2)^2}{R_{TE}} \tag{7}$$

where $m$ is the ratio of load resistance, $R_L$, to the internal resistance of the TE device, $R_T \approx R_{TE}$. Here $m = \sqrt{1 + zT_{avg}} \approx 1$ because $zT$ values of polymers demonstrated in literature are << 1.[111] The power density is obtained by normalizing with respect to the hot-side heat exchanger area, $A_{HX,\,H}$. The efficiency of the radial TEG is given by:[3]

$$\eta = \frac{P}{Q_H} = \frac{ZT_1}{ZT_m + ZT_1 + 4} \left( \frac{T_1 - T_2}{T_1} \right) \tag{8}$$

The preceding two equations for a radial device are identical to that of a flat-plate TEG, and $ZT$ is introduced as the *module* figure-of-merit given by:[114]

$$ZT = \frac{S_{p-n}^2 T}{K_{TE} R_{TE}} \tag{9}$$

where $S_{p\text{-}n} = S_p - S_n$ is the difference in thermopower of the two thermoelectric legs.

### *4.3.2 Maximizing ZT – Geometry Matching Condition*

To maximize the module figure-of-merit $ZT$, the denominator is minimized with respect to the device geometry. This minimum value of the $R_{TE}K_{TE}$ product yields the geometry matching condition for a TEG and maximizes the device efficiency. For a radial architecture, the geometry matching condition is given by:

$$\frac{t_n \ln\left(r_{out,p} / r_{in,p}\right)}{t_p \ln\left(r_{out,n} / r_{in,n}\right)} = \sqrt{\frac{k_p \sigma_p}{k_n \sigma_n}} \tag{10}$$

where $r_{out,p}$ and $r_{out,n}$ are the outer radii of the p- and n-type TE material, $r_{in,p}$ and $r_{in,n}$ are the fixed inner radii of the TE material. $\sigma_p$ and $\sigma_n$ are the electrical conductivities, $k_p$ and $k_n$ are the thermal conductivities, and $t_p$ and $t_n$ represent the thickness of the p- and n-type TE materials on each disk. The geometry matching condition provides an optimization between n- and p-type material properties and device parameters for a radial architecture; this is summarized in Table 5 for the flat-plat geometry as well.

**Table 5 – Summary of thermal and electric equations for a flat-plate and radial thermoelectric device as well as the derived geometry matching condition.**

| | *Flat-Plate* | *Radial* |
|---|---|---|
| Electrical Resistance, $R_{TE}$ | $\frac{L_p}{\sigma_p A_p} + \frac{L_n}{\sigma_n A_n}$ | $\frac{\ln\left(r_{out,p} / r_{in,p}\right)}{2\pi \sigma_p t_p} + \frac{\ln\left(r_{out,n} / r_{in,n}\right)}{2\pi \sigma_n t_n}$ |
| Thermal Conductance, $K_{TE}$ | $\frac{k_p A_p}{L_p} + \frac{k_n A_n}{L_n}$ | $\frac{2\pi k_p t_p}{\ln\left(r_{out,p} / r_{in,p}\right)} + \frac{2\pi k_n t_n}{\ln\left(r_{out,n} / r_{in,n}\right)}$ |
| Geometry Matching Condition | $\frac{A_n l_p}{A_p l_n} = \sqrt{\frac{k_p \sigma_p}{k_n \sigma_n}}$ | $\frac{t_n \ln\left(r_{out,p} / r_{in,p}\right)}{t_p \ln\left(r_{out,n} / r_{in,n}\right)} = \sqrt{\frac{k_p \sigma_p}{k_n \sigma_n}}$ |

The *module ZT* simplifies to the *material zT* under the assumption that the n- and p-type legs have the same magnitude of thermopower, electrical conductivity, and thermal conductivity (see Appendix B.1). A reasonable constraint is to allow the outer and inner radii of the p- and n-type legs to be the same ($r_{out,p} = r_{out,n} = r_{out}$ and $r_{in,p} = r_{in,n} = r_{in}$) which

leaves thickness as the tunable geometric parameter in the geometry matching condition equation.

### *4.3.3 Maximizing Heat Flux – Critical Radius*

To understand different length scales for a radial device, a characteristic thermal length is defined:

$$L_T = \frac{k}{h} \tag{11}$$

where $k$ is the effective thermal conductivity of the TE device and $h$ is the convective heat transfer coefficient of the cold-side heat exchanger. This definition is motivated by performing the routinely solved critical insulation thickness[115] analysis that maximizes heat transfer in a radial system (see Appendix B.2). In this case, upon addition of insulation (*i.e.,* increasing $r_{out}$ for the radial TEG), the conduction resistance increases while the convection resistance decreases due to a larger available surface area; this results in a critical radius that maximizes the heat flux from the inner surface.

In most radial systems, the effects of a critical radius are neglected as $L_T << r_{in}$ owing to the low thermal conductivity of common insulation materials. For inorganic TEs with $k \sim 1$ W/m-K, $L_T$ is large and impractical to design around. Polymers, however, have a thermal conductivity that is typically an order-of-magnitude smaller than inorganic TE materials and significantly higher than insulation. This thermal conductivity allows polymer TEGs to rely on natural convection alone, which potentially reduces device cost (by lack of infrastructure), if designed properly. By selecting the material (*i.e.*, polymers $k \approx 0.2$ W/m-K) and the type of cooling (*i.e.,* natural convection $h \approx 5$ W/m$^2$-K), $L_T$ is on the

order of several centimeters making the manufacturing impractical for polymer-based flat-plate devices. However, this leg length is realizable in a radial geometry as polymers can be solution-processed, *i.e.*, by screen-printing into thin-films extending for several centimeters in the in-plane direction. Designing a radial TEG with a leg length $L_{cr} = r_{out} - r_{in} = L_T - r_{in}$ maximizes heat flux through the device. As an example, for nominal values of $k$ = 0.2 W/m-K, $h$ = 5 W/m$^2$-K, and setting $r_{in}$ = 6.4 mm (0.5 inch diameter heat pipe), the characteristic thermal length is $L_T$ = 4 cm and $L_{cr}$ = 3.4 cm.

### *4.3.4 Thermal Impedance Matching – Heat Exchanger Design*

For a holistic optimization of the TEG performance, it is important to consider the heat exchangers and how the temperature difference is distributed through the device. If the leg length is too short, maintaining a temperature difference is difficult and thus the power output will be small. If the leg length is too long, then the electrical resistance will be large and thus the power output will again be small. Hence, there exists an intermediate length that optimizes this trade-off, and this is referred to as the thermal impedance matching condition.[107,113,116] For flat-plate TEGs, the thermal impedance matching condition has been derived as $L = 2FL_T$, where $L$ is the leg length that maximizes power.[107,110,113] At this condition, half of the temperature drop is across the active thermoelectric legs and the other half can be distributed between the hot- and cold-side heat exchangers (typically, with the majority across the cold-side).[117,118]

I performed a similar analysis for the radial device (see Appendix B.3). As a limiting example, a cold-side heat exchanger that operates with natural convection alone and a hot-side heat exchanger consisting of a copper pipe (low thermal resistance) was

considered. In this scenario, the thermal resistor network in Figure 30 can be simplified such that: (i) $R_H = 1/K_H << 1$ so the overall heat exchanger thermal resistance is dominated by the cold-side, (ii) $K_{||}$ is negligible (corresponding to negligible parallel heat flow through the substrate), and (iii) the n- and p-type materials have identical geometries and thermophysical properties (except Seebeck coefficients which are opposite in sign) such that $t_p = t_n = t$, $k_p = k_n = k$, $\sigma_p = \sigma_n = \sigma$, and $S_p = -S_n$. When the conductance of the active thermoelectric elements is matched to that of the cold-side heat exchanger,

$$\ln\left(\frac{r_{out}}{r_{in}}\right) = \left(\frac{1}{r_{out}}\right) L_T \tag{12}$$

where $r_{out}/r_{in}$ can be recast as the fill factor, $F$. The characteristic thermal length, $L_T$ defined previously appears in this expression with a pre-factor less than 1 indicating that thermal impedance matching occurs at a leg length less than $L_T$. At this condition, the temperature drop across the TE material and the cold-side is equal. Solving for $r_{out}$ gives the leg length that corresponds to a thermally impedance matched radial device, $L_{match} = r_{out} - r_{in}$. As an example, setting $r_{in}$ = 6.4 mm (0.5 inch diameter heat pipe) and $L_T$ = 4 cm, results in $r_{out}$ = 2.7 cm and $L_{match}$ = 2.1 cm (subscript denotes matched conductance of the TE and cold-side heat exchanger).

### *4.3.5 Maximizing Power Density – Optimum Leg Length*

In the flat-plat geometry, the thermal impedance matching condition maximizes the power output.[107] For the radial geometry, this is not true and the key difference lies in the unmatched nature of the hot- and cold-side heat exchangers. To derive an analytical expression for the optimum leg length that maximizes power (and power density

normalized to the hot-side area), heat flows $Q_H$, $Q_{TE}$ and $Q_C$ were assumed to be approximately equal as the Peltier effect is negligible for small $zT$. Without this simplification, a numerical optimization would be required to yield a similar result but at the expense of analytical elegance.

$$K_H(T_H - T_1) \approx K_{TE}(T_1 - T_2) \approx K_C(T_2 - T_C) \tag{13}$$

Since $K_H >> K_{TE}$, the temperature drop across the hot-side heat exchanger is negligible (*i.e.*, $T_H \approx T_1$) which simplifies the temperature drop across the module to:

$$T_1 - T_2 \approx \frac{K_C}{K_C + K_{TE}}\left(T_H - T_C\right) \tag{14}$$

This equation is beneficial to obtain closed-form analytical solutions for optimizing the performance of the radial TEG; the preceding two equations are exact under a small $zT$ approximation, which is reasonable for polymer TEs at their current stage of development. For larger $zT$s, the Peltier and Joule heating terms can be accounted for by solving the non-linear system of equations that describe heat flow through the device. Substituting this simplified temperature drop into the power output yields:

$$P \approx \pi\left(t\sigma {S_{p-n}}^2 \left(T_H - T_C\right)^2\right)\left(\frac{m}{(1+m)^2}\right)\left(\frac{\ln(r_{out}/r_{in})}{\left(\ln(r_{out}/r_{in}) + \left(L_T/r_{out}\right)\right)^2}\right) \tag{15}$$

Finally, the outer radius (and hence, leg length) that maximizes power is (see Appendix B.4):

$$\ln\left(\frac{r_{out}}{r_{in}}\right)=\left(\frac{1}{r_{out}-2L_T}\right)L_T \tag{16}$$

Solving for $r_{out}$, the maximum power condition for a radial TEG that corresponds to unmatched conductances is obtained. For the nominal values used earlier, $r_{out}$ = 9.5 cm and $L_{opt} = r_{out} - r_{in}$ = 8.8 cm is the leg length that maximizes power. This value is larger than the leg length corresponding to the thermal impedance matching condition; this is evident by comparing the pre-factor in Equation 12 which is less than that in Equation 16. This indicates that the radial architecture attains a maximum power density when the conductance of the TE module is different from that of the cold-side heat exchanger. This is in contrast to a flat-plate device that requires active cooling in order to match the TE conductance for maximum power. Thus, the radial device benefits from unmatched conductances that enable operation under natural convection alone. The analytical expressions presented herein describe the overall performance-optimization of a radial polymer TEG for the first time.

### 4.4 Radial TEG Numerical Thermoelectric Model

To test the validity of the analytical model, I performed a more rigorous numerical analysis without the simplifying assumptions in the previous section. Dedoped DMSO-mixed PEDOT:PSS ($S_p$ = 72 μV/K, $\sigma_p$ = 890 S/cm, and $k_p$ = 0.33) was chosen as the p-type material as it is the polymer with the highest reported $zT$;[19] a fictitious n-type material was used with identical properties except for the sign of the Seebeck coefficient as a preliminary illustration.

### *4.4.1 Model Input Parameters*

A thermal contact conductance of 0.1 W/K-cm$^2$ (typical value for copper interfaces)[115] and an electrical contact resistance of $10^{-9}$ Ωm$^2$ were assumed.[107] The substrate and separator were modeled as 25 μm-thick polyimide films since the thermal conductivity is comparable to that of thermoelectric polymers. The hot-side heat exchanger was a 0.5 inch diameter copper pipe with a conductance of 10 W/K.[119] For the cold-side heat exchanger, the convective heat transfer coefficient was calculated for different leg lengths using the long horizontal cylinder correlation for natural convection (see Appendix B.5).[115] For fixed hot- and cold-side temperatures $T_H$ = 400 K and $T_C$ = 300 K, the heat flow equations form a system of coupled non-linear equations (including the Peltier effect and Joule heating) that can be solved numerically to obtain exact values for the junction temperatures $T_1$ and $T_2$. Table 6 summarizes the parameters used in the numerical model

**Table 6 – Parameters used to model the polymer-based radial TEG. Dedoped PEDOT:PSS with DMSO is the p-type material and the n-type is identical except for the sign of the Seebeck coefficient.**

| Parameter | Value |
|---|---|
| $T_H$ - $T_C$ [K] | 100 |
| Thermal Contact resistance [cm$^2$-K/W] | 10 |
| Electrical Contact resistance [Ω m$^2$] | $10^{-9}$ |
| Substrate thickness [μm] | 25 |
| Device inner radius [mm] | 6.4 |
| TE material thickness [μm] | 40 |

The device outer radius (and hence, leg length) and active material thickness were the two free design variables to optimize device geometry and performance. The resulting heat flux, power density normalized to the hot-side area) and efficiency are obtained using the equations presented in the previous section.

### *4.4.2 Model Outputs – Power Density and Optimum Leg Length*

A contour plot of the power density in mW/cm$^2$ as a function of dimensionless leg length, $\tilde{L} = L / L_T$ and dimensionless thickness, $\tilde{t} = t / t_{sub}$ is shown in Figure 31.

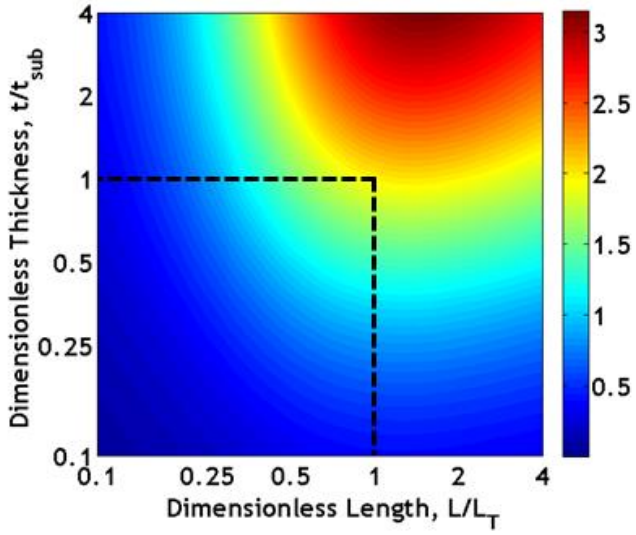


**Figure 31 – Power density contours (mW/cm$^2$) as a function of leg length $L = r_{out} - r_{in}$ and active material thickness. The color bar represents the power density values (normalized to the hot-side area). Dashed lines correspond to a power density of 2 mW/cm$^2$ when the leg length is designed at the characteristic thermal length and the material thickness is identical to that of the substrate.**

For a fixed leg length, the power density increases with active material thickness; the lower limit is determined by the thickness of the substrate and separator which contribute to heat loss. The upper limit is dictated by manufacturing and/or film processing techniques (screen printing, inkjet printing, *etc.*). Since the TE material and substrate have

similar thermal conductivities, the heat flow is predominantly through the active material when $\tilde{t} \geq 1$, and a power density of ~ 2 mW/cm$^2$ is attained when $\tilde{L} = 1$. Instead, if the material thickness is fixed, power density increases with leg length, reaches a maximum at $L_{opt} = r_{out} - r_{in}$, and then decreases. This is expected as the thermal and electrical resistances dominate at large leg lengths, thereby reducing the heat through the device and consequently, the power output. Obtaining a power density of 2 mW/cm$^2$ would represent an improvement of three orders-of-magnitude over the best performing organic prototypes, bringing polymer TEG power densities within a factor of two of the best demonstrated flexible inorganic TEG (made from $Bi_2Te_3$ and $Sb_2Te_3$ pastes).[120]

The heat flux and power density for a radial TEG as a function of leg length for fixed thickness, $t = t_p = t_n = 40$ μm is shown in Figure 32. Both curves increase with leg length and reach a maximum, after which they decrease with increasing leg length. The leg length that maximizes heat flux ($L_{cr}$) is different from the leg length that maximizes the power density ($L_{opt}$) and that of the thermal impedance condition ($L_{match}$). The heat flux has a maximum value of 146 mW/cm$^2$ at a leg length of 3 cm for a realistic device. This leg length is within 11% of the critical radius derived based on Equation 11 that maximizes the heat flux in a radial system. The power density curve follows a similar trend and reaches a maximum of 2.45 mW/cm$^2$ when the leg length is approximately 12 cm. However, this maximum is rather flat for a range of leg lengths between 8 and 20 cm. The lower limit agrees reasonably well (within 12%) with the optimum leg length, $L_{opt}$ obtained from the analytical model predictions in Equation 16 for unmatched heat exchangers. Thus, these simulated leg lengths are well-approximated by the analytical heat transfer framework that was presented earlier in this chapter. Small differences are attributed to including substrate

and separator contributions to the thermal network and contact resistance contributions to the electrical network in the exact numerical analysis compared to the approximate analytical solution.

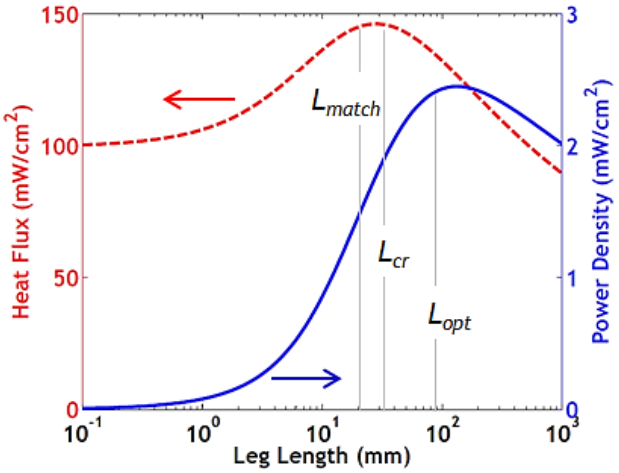


**Figure 32 – Performance of a radial TE generator showing heat flux (in red) and power density (in blue) normalized to the hot-side as a function of leg length, $L = r_{out} - r_{in}$. The leg length that maximizes heat flux is not the same length that maximizes power density. The gray lines correspond to the analytical solutions for leg length for maximum heat flux ($L_{cr}$), thermal impedance matching ($L_{match}$) and power ($L_{opt}$).**

To illustrate the advantages of the radial TE generator, I modeled a flat-plate device under the same conditions; this is shown in Figure 33. The heat flux decreases with increasing leg length owing to a larger conduction resistance, while the power density increases with leg length and reaches a maximum, after which it decreases with increasing leg length. In contrast to the radial device, the leg length that corresponds to a thermal impedance matched device ($L_{match}$) is identical to the optimum leg length that maximizes the power density ($L_{opt}$) for a flat-plate TEG. The heat flux has a maximum value of 50 mW/cm$^2$ at very small leg lengths (< 1 mm) while the power density reaches a maximum of 0.4 mW/cm$^2$ when the leg length is approximately 8 cm. This length is impractical for a

flat-plate device owing to manufacturing constraints. Furthermore, the power density is reduced by a factor of six compared to the radial device for the same material properties.

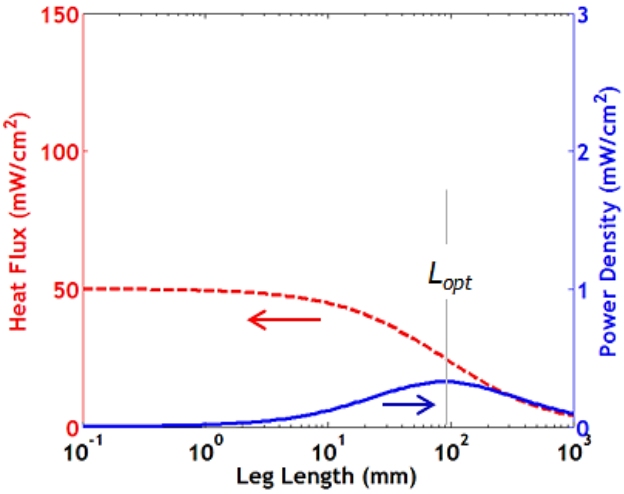


**Figure 33 – Performance of a flat-plate TE generator showing heat flux (in red) and power density (in blue) as a function of leg length, *L*. The gray line is the analytical solution for leg length, $L_{opt}$ for thermal impedance matching and maximum power.**

### *4.4.3 Model Outputs – Electrical Contact Resistance and Efficiency*

A major obstacle towards high performance polymer prototypes has been large contact resistance between the thermoelectric material and the electrodes,[14,23,63] resulting in low power densities in traditional flat-plate devices. A radial architecture overcomes this due to its orthogonal geometry which results in radial transport in the TE material and axial transport in the metal contacts, thereby enabling higher power density devices. Figure 34 shows the efficiency and significance of contact resistance (as a percentage of the internal electrical resistance of the TE module) for the radial device and flat-plate device. At the optimum leg length that maximizes power density, the efficiency approaches 2% for both device architectures. For the radial device, the contact resistance is negligible due to a larger cross-sectional area on the face of the disks. In contrast, polymer flat-plate devices reported in literature are designed with leg lengths on the order of <50 μm where the contact

resistance is no longer negligible (~ 10%), resulting in low power densities. This again highlights the advantages of the radial architecture, thereby enabling high power density polymer thin-film devices for the first time.

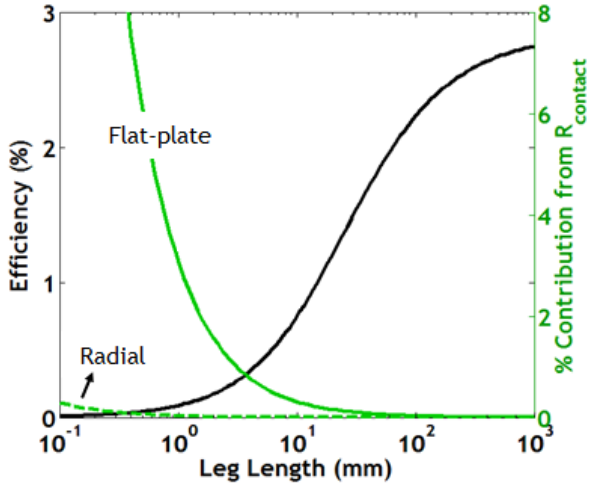


**Figure 34 – Performance comparison of a radial TE generator and flat-plate device showing efficiency (in black) and electrical contact resistance contribution to overall device resistance (in green). The efficiency for a flat-plate and radial device are the same but contact resistances are significantly lowered for a radial device (green dashed line).**

Thus, by designing a device around the characteristic thermal length for polymers, *i.e.*, by moving to a radial geometry, the contact resistance becomes negligible and power density is enhanced, while eliminating the need for a cold-side heat exchanger. These promising outcomes motivated the development of a proof-of-concept radial device that is outlined in the following section.

## 4.5 Radial TEG Prototype Development

To validate the radial TEG model and to demonstrate its advantages, a prototype was designed and demonstrated. PEDOT:PSS with tellurium nanowires was used as the p-type material[15] and poly[K(NiETT)] blended with PVDF/DMSO was the n-type material.[76] These materials were selected because I could replicate these syntheses with confidence in

large volumes. The fabrication involved coating these polymers onto paper disks (substrate) using calligraphy and screen-printing electrical contacts. This facile fabrication and testing of the radial proof-of-concept device is presented herein.

### *4.5.1 Polymer Synthesis*

Hybrid Te nanowires in PEDOT:PSS was synthesized following previously reported procedures.[15,38] For the n-type material, K(NiETT) dispersions in PVDF/DMSO developed in chapter 2 was used, with an air oxidation time of 24 hours.[76] First, thin-films of n-type and p-type materials were prepared on 1cm x 1cm glass substrates to make comparisons with data reported in literature. The p-type samples were placed on a shiny aluminium block (~80 μL of solution was drop cast onto each substrate) and heated under a heat lamp until dry and then annealed at 120 $^{0}$C for 5 minutes. Resultant films were shiny and reflective after drying, and the morphology of the hybrid Te nanowires was characterized using an SEM (Hitachi SU8230). For the n-type samples, ~35 μL of ETT suspended in PVDF/DMSO was drop cast and films were dried in a vacuum oven at 50 $^{0}$C for 30 minutes.

### *4.5.2 Polymer - Paper Composite*

In order to fabricate a proof-of-concept device based on the radial architecture, paper was chosen as the substrate since large area, free-standing films proved to be too challenging to fabricate. Furthermore, a paper-based device is desirable for low cost, light-weight and flexible electronics, and has been used effectively in previous polymer TEG prototypes.[104,121,122] Also, since PEDOT:PSS is water-based, it shows better wettability on paper as compared to other polymer substrates such as polyimide. One additional

advantage of a paper-based device is that the thermal conductivity could be lower than the polymer itself,[121] which would be beneficial for TEGs. Given the porous nature of paper, upon coating polymer solutions, a composite was formed rather than a thin film on a substrate. In order to measure properties of this composite, calligraphy was used to directly coat the p-type and n-type polymer inks onto both sides of 1cm x 1cm paper until it was saturated (for a direct comparison with the films on glass). The samples were then dried in an oven at 60 $^{0}$C for 30 minutes to evaporate excess solvent. The p-type composite was gray and the n-type composite was black, with a thickness of ~80 - 100 μm corresponding to that of paper.[106] Four silver paint contact pads (CB028, DuPont) were added to each composite film for thermoelectric measurements, as shown in Figure 35.

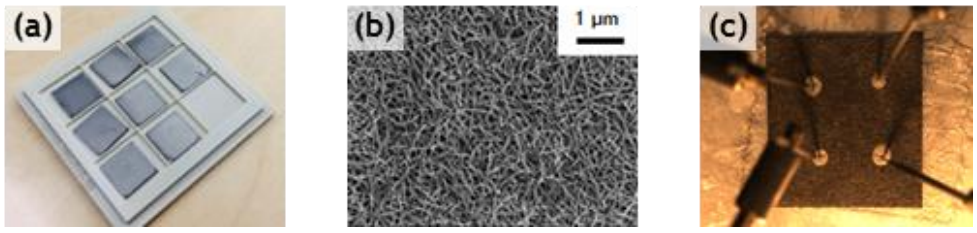


**Figure 35 – (a) P-type hybrid PEDOT:PSS-Te nanowire thin-films on glass, (b) Film morphology of these films characterized using SEM, and (c) Paper composite with silver paint contact pads for thermoelectric property measurements.**

Thermoelectric properties of the p-type and n-type pristine thin-films (on glass) as well as the polymer-paper composite are tabulated in Table 7. The p-type thin-film values agree with previously reported measurements,[15] and n-type properties are in agreement with chapter 2.[76] In contrast, paper composites showed very different thermoelectric properties. The electrical conductivity drops significantly for both the p- and n-type composites as expected, and this is attributed to the electrically insulating nature of paper. It is interesting to note however that the Seebeck coefficient of hybrid Te nanowires in

PEDOT:PSS showed an ~80% increase on paper. Similar observations have been made in PEDOT:PSS/paper composites and in PANI/CNT nanocomposites although the mechanism is not well-understood.[121,123] The reduction in electrical conductivity of the paper composite is expected to significantly reduce power density of the radial prototype.

**Table 7 – Thermoelectric properties of polymer thin films and polymer-paper composites at room temperature (295 K). Electrical conductivity values are determined at a thickness of 80 μm corresponding to paper.**

| | $\sigma$ (S/cm) | $S$ (μV/K) | $S^2\sigma$ (μW/m-K$^2$) |
|---|---|---|---|
| p-type PEDOT:PSS with Te nanowires | | | |
| Pristine Film | 4.2 ± 0.5 | 109.1 ± 8.6 | 4.9 ± 0.6 |
| Paper Composite | (4.9 ± 0.6) x $10^{-3}$ | 204.1 ± 19.8 | (2.1 ± 0.4) x $10^{-2}$ |
| n-type poly[K(NiETT)] with PVDF/DMSO | | | |
| Pristine Film | 12.6 ± 0.7 | -34.7 ± 3.1 | 1.5 ± 0.1 |
| Paper Composite | 0.5 ± 0.06 | -28.3 ± 1.5 | (4.1 ± 0.5) x $10^{-2}$ |

### *4.5.3 Fabrication of Radial TEG Prototype*

For the proof-of-concept radial device, paper disks with $r_{in}$ = 6.5 mm and $r_{out}$ = 35 mm were cut using a Silhouette Portrait to serve as substrates. These dimensions were chosen based on the characteristic thermal length for polymers as discussed earlier in this chapter. Disks were secured on a glass plate in order to prevent wrinkling, and calligraphy was used to coat hybrid Te nanowires in PEDOT:PSS ink and the K(NiETT)/PVDF/DMSO blend onto paper. Disks were dried at 70 $^0$C for 30 minutes in an oven, and once dry, the second side of each disk was coated with the same material and dried as before. As a final step, silver ink (CB028, DuPont) was screen printed onto each disk to serve as electrical contacts, as illustrated in Figure 36. Polyimide sheets ~25 μm in thickness (DuPont, part #100FPC kapton) were cut into disks to electrically isolate the p-type and n-type disks.

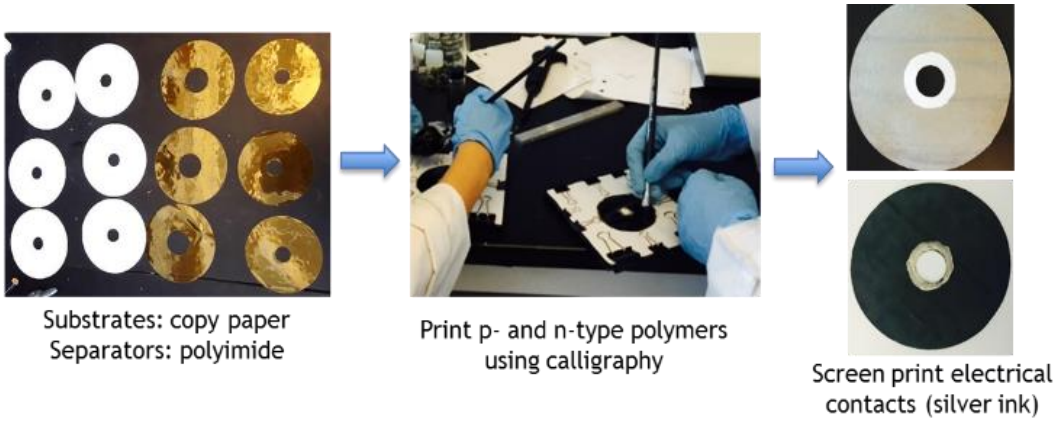


**Figure 36 – Radial TEG step-by-step fabrication process that involves cutting paper disks (substrates) and polyimide disks (separators), coating p- and n-type polymer inks using calligraphy, and screen-printing silver contacts.**

Important parameters that affect the device perfomance include the thickness of the active material and uniformity of the disks. In order to ensure uniformity, both within a disk and between disks, sixty polymer-paper disks were fabricated and their thermoelectric properties were measured. Thirty of the most uniform and consistent disks (*i.e.*, 15 p-n couples) with similar $S$ and $\sigma$ were down-selected for the prototype demonstration.[106]

### *4.5.4 Experimental Testing of Radial TEG*

Alternating p- and n-type polymer-paper disks and separators were stacked on a 0.5 inch diameter copper rod and mechanically pressed using a spring-collar assembly to ensure good electrical contact. A cartridge heater (McMaster Carr, part #3618K416) was inserted in the copper rod to serve as the heat source and was maintained at a constant temperature using a temperature controller (Omega Engineering, part #CNI-CB120SB-K). Natural convection maintained the outer surface of the device at ambient temperature thereby eliminating the need for a separate cold-side heat exchanger. Electrical wires were attached to the disk stack using silver paste to serve as voltage leads, and four K-type

thermocouples were used to measure the hot-side ($T_H$), cold-side ($T_C$) and junction temperatures ($T_1$ and $T_2$). A calibrated heat flux sensor (Omega Engineering, part #HFS-4) was wrapped around the copper rod prior to stacking the disks in order to measure the heat flux and to quantify device efficiency; Figure 37 illustrates the experimental setup.[106]

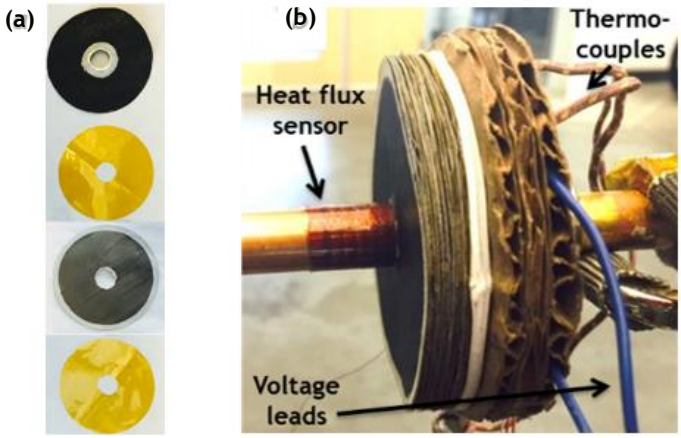


**Figure 37 – (a) A single p-n couple consisting of an n-type disk, inner separator, p-type disk and and outer separator. (b) Radial TEG experimental setup consisting of 15 p-n couples stacked on a copper rod and cooled by natural convection.**

For device testing, temperature gradients were applied across the device, while voltage and resistance values were measured with a Keithley 2700 for power calculations. The heat flux sensor was completely covered for data collection and is exposed in Figure 37 merely as an illustration, and cardboard was used to secure thermocouples and voltage wires in place for all measurements. For a radial TEG consisting of 15 p-n couples, the open circuit voltage and internal resistance as a function of junction $\Delta T$ are shown in Figure 38. As expected, the open circuit voltage increased linearly with temperature; the slope gives a module thermopower of 2.14 mV/K. The internal device resistance decreased with increasing temperature, which is indicative of semi-conducting behavior in both the p- and

n-type polymers.[15,23,76] The open circuit voltage was 85 mV at $\Delta T \approx 45$ K, which is higher than demonstrated devices for the same number of couples.[73,104,122]

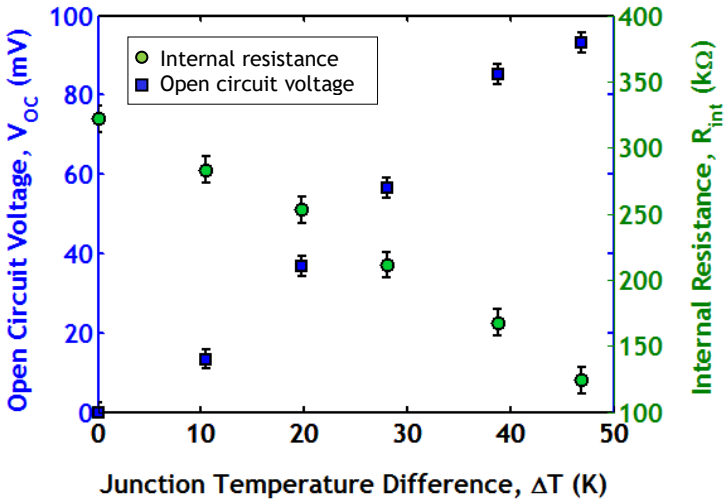


**Figure 38 – Radial TEG open circuit voltage (shown in blue) and internal resistance (shown in green) as a function of temperature for 15 p-n couples.**

The power output and power density normalized to the hot-side area of the radial device for different load resistances at $\Delta T \approx 45$ K (hot-side and cold-side are maintained at 125 °C and 22 °C) is shown in Figure 39.

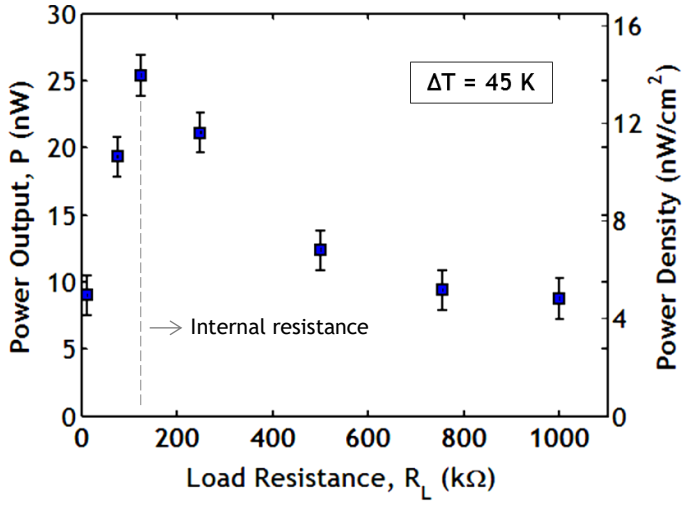


**Figure 39 – Power output and power density of a radial TEG with 15 p-n couples at different load resistances when $\Delta T$ = 45 K. Power peaks at $R_L$ = 125 kΩ corresponding to matched internal resistance, confirming the load matching optimization condition.**

For this radial TEG consisting of 15 p-n couples, a maximum power output of 27 nW was obtained at a load resistance of 125 kΩ, which corresponds to the internal resistance of the module. This is known as the load matching condition, *i.e.*, $m = 1$ that results in maximum power. Under these conditions, the corresponding power density is ~14 nW/cm$^2$, which is comparable to other printed TEGs[63,73,104,122] with the added advantage of a geometry that can couple easily to heat sources *(e.g.* pipes) and requires no active cooling.[106]

As a final step, the device performance was compared to the numerical model described in the previous section.[105] This is illustrated in Figure 40 where the power density (and power output) predicted by the model follows the same trend as the prototype device. However, the model over-predicts the experimental data, which is attributed to using nominal values for thermal and electrical contact resistances, as these could not be independently measured.

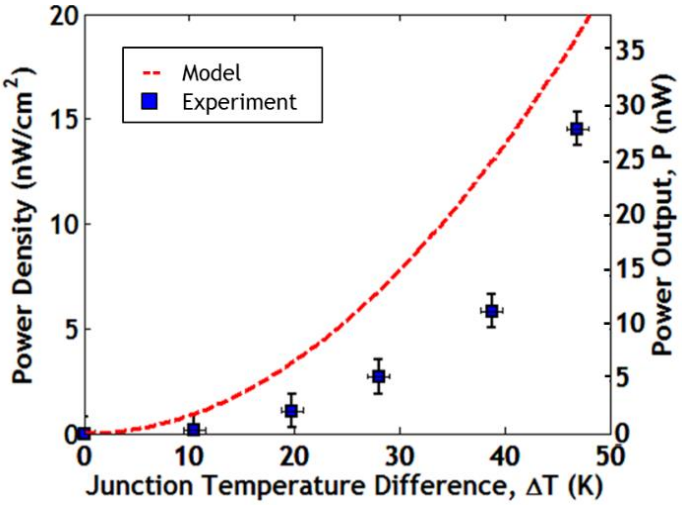


**Figure 40 – Comparison of experimental data (shown in blue) and radial TEG model predictions (shown in red) for power density as a function of junction temperature difference at load matched conditions.**

Uncertainty in estimating the thermal conductivity of the polymer-paper composite, as well as minor property variations across disks may also contribute to differences between the model and experimental results. Another source of error could arise from fixing the natural convection coefficient as 5 $W/m^2$-K in the numerical model, as the real value was not independently measured. The numerical model was also compared to the measured heat flux output from the sensor. At $\Delta T$ = 45 K, the measured heat flux was 97 ± 9.7 $mW/cm^2$, which agrees well with the model prediction of 107.4 $mW/cm^2$.

In order to improve power density and demonstrate a high performance radial TEG, free-standing polymer films are desirable as this would eliminate the paper substrate. As an illustration, for a 25 μm polyimide substrate printed with 40 μm of the same p-type and n-type polymers, the numerical model predicts a power density of ~20 $\mu W/cm^2$ for the same device dimensions subjected to the same fixed hot- and cold-side temperatures. The potentially low-cost fabrication process and device operation under natural convection alone are encouraging for the adoption of polymer-based TEGs based on this new radial device architecture.

## 4.6 Conclusions

With the continued progress in developing organic thermoelectric materials, engineering considerations such as device design become important. Limitations with existing polymer-based prototype devices can be addressed by moving to architectures beyond the conventional flat-plate configuration. In this chapter, I have demonstrated that an optimized geometry for polymers is obtained by incorporating material properties, device physics, and heat exchanger considerations. Specifically, by designing around a

characteristic thermal length of $L_T \sim 4$ cm, a radial design was presented that accommodates a hot fluid as the heat source and utilizes natural convection to cool the device. Furthermore, electrical interconnect and contact resistances are minimized because of the large cross-sectional area in the radial configuration, which addresses a major drawback with existing polymer prototypes.[105,124] As a proof-of-concept, a radial TEG prototype was demonstrated by coating hybrid Te nanowires in PEDOT:PSS as the p-type material and poly[K(NiETT)]/PVDF/DMSO as the n-type material on paper disks. Upon application of a ~45 K temperature difference, a voltage of ~85 mV was generated and a power density of ~15 nW/cm$^2$ was obtained without active cooling.[106] With state-of-the-art polymer TEs, power densities of mW/cm$^2$ are achievable when designed using the radial architecture. The design of devices tailored for polymers has implications beyond waste-heat recovery, towards wearable electronics and self-powered sensors; this is the focus of the following chapter.

# CHAPTER 5. WEARABLE THERMOELECTRICS WITH FRACTAL INTERCONNECT PATTERNS

The solution processability and low thermal conductivity of polymers enables new device architectures, such as the radial TEG that was discussed in the previous chapter. Furthermore, since polymers are light-weight and flexible, they can also be used for body-heat harvesting devices for self-powered sensors.[125-127] These applications require power sources on the order of μW – mW,[125] that are compact and operate with a through-plane $\Delta T$, which makes printed thin-film thermoelectric modules suitable. However, in this thin-film limit, the electrical contact and interconnect resistances can become significant and can lower the overall performance, necessitating careful consideration of device design. Furthermore, fabrication techniques such as screen printing[73,103,104,128-133] and inkjet printing[63,134-140] result in a printed layer thickness that is limited to tens of microns. This makes energy harvesting from a through-plane temperature difference challenging, because only a small portion of the imposed temperature difference occurs across the active TE material, and the majority occurs across the substrate.[103] This drastically reduces the generated voltage from the TE device, resulting in low performance organic prototypes. For this reason, most polymer-based TEGs are designed to use a lateral (in-plane) temperature gradient.[105,106,125,134-139] However, for wearable devices, energy harvesting from a through-plane temperature difference is desirable.

In this chapter, a new device layout is presented for printed polymer-based thermoelectric devices. By positioning TE legs in a hexagonal close-packed layout and

using a new interconnect pattern based on the Hilbert space filling curve, the performance of wearable devices can be enhanced, as outlined in the following sections.[141]

## 5.1 Design Considerations for Polymer Thin-Film Devices

The voltage output of an organic TEG depends on the temperature difference across the thermoelectric legs and the number of legs (for a fixed Seebeck coefficient of the p- and n-type leg pair): $V = N S_{p\text{-}n} \Delta T$. To enhance device performance, one approach is to make the TE legs longer (*i.e.*, the active material thickness should be equal to or larger than substrate thickness), so that a higher portion of the imposed temperature difference is across the active material. Longer leg lengths from organic TE materials can be fabricated using molding[70,142] and lithography.[18,143] However, these techniques require modifications to the substrate, which consequently increases manufacturing costs. Dispense printing is another technique than can be utilized to fabricate longer legs;[134] this technique however requires large amounts of material, and also requires modifications to the material properties to ensure they are in the correct range for dispense printing.[144] To increase leg length and circumvent thermal losses through the substrate, some of the ideas from the radial TEG discussed in chapter 4 can be revisited, such as printing thermoelectric materials on to porous substrates.[105,106] This way, the active material thickness is at least equal to the substrate thickness ensuring that most of the temperature drop occurs across the TE material. The numerical thermoelectric model developed in Section 4.4 can be extended to a flat-plate device to obtain an optimum leg length that maximizes power density.[105,107] For a typical polymer in the flat-plate architecture, this is ~ 100 µm (this was shown in Figure 33, also see Appendix C.1), which makes paper and textiles potential candidate substrates for printing low cost organic TE devices.

The output voltage from a thermoelectric device is also directly proportional to the number of TE legs, so this is another approach to enhance device performance. Assuming $\Delta T$ = 5 K (representing a human touch for wearable electronics) and using the properties of dedoped PEDOT:PSS[19] ($S$ = 72 μV/K) as the p-type material and a fictitious material with identical properties except for the sign of the Seebeck coefficient as the n-type material, a voltage output of 2 V can be generated from 3600 legs as shown in Figure 41. It is worth noting that increasing the number of legs does not necessarily lead to larger device sizes, as printing techniques (such as high-resolution inkjet printing) allow for positioning many TE legs in a small area. Such high packing densities for TE legs are impossible to achieve using the existing fabrication methods for inorganic TEGs that include dicing[145] and pick-and-place techniques.[146]

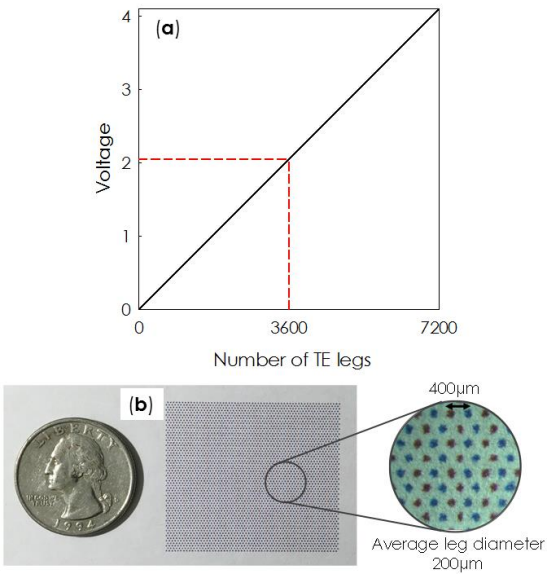


**Figure 41 – (a) Output voltage from a thermoelectric device as a function of number of legs using properties of dedoped PEDOT:PSS.[19] (b) 3600 legs are positioned in an area of 36.0 mm by 31.2 mm using a desktop inkjet printer (EPSON XP860) showing high packing density. Red and blue colors are regular printing inks that represent n- and p-type polymers, respectively, for illustration purposes only.**

While increasing the number of legs seems promising, it has one major drawback: the total interconnect length increases as the p- and n-type materials must be wired in series. This, along with operating in the thin-film limit, ultimately makes interconnects the dominant resistance in the system, and this has resulted in low power outputs for organic TE prototypes.[63,103] To address these challenges, a new device layout for polymer-based wearable thermoelectrics is presented herein.

## 5.2 Close-Packed Layout for High Fill Factors

In a traditional flat-plate inorganic thermoelectric device, the legs are diced to have rectangular cross-sections, are positioned in a square lattice using a pick-and-place machine, and are wired in series using solder interconnects in a serpentine pattern. Typical leg lengths for these modules are 2-5 mm, and the packing density or fill factor, $F$ can be estimated to be ~25%. For polymer-based thermoelectric devices, printing-based fabrication techniques allow for a broader range of geometries and interconnect patterns. Particularly, using high resolution inkjet printing, legs with different cross-sections such as circular legs with smaller diameters can be printed much closer together. This results in a higher $F$ for the module, thereby enabling higher power density for body heat harvesting applications. Taking this further, the legs can be positioned in a hexagonal close-packed layout, which can help achieve a maximum theoretical $F = \pi/2\sqrt{3}$ ~91% for circular legs on a two-dimensional plane (see Appendix C.2). These different design layouts are illustrated in shown in Figure 42. In addition to higher fill factors, by placing thermoelectric legs closer together, the interconnect length also decreases, which in turn lowers the total resistance and results in a higher power output; this is crucial when the TE module includes

a large number of legs (>2000 for organic modules compared to the typical ~250 legs for inorganic modules for the same output voltage).

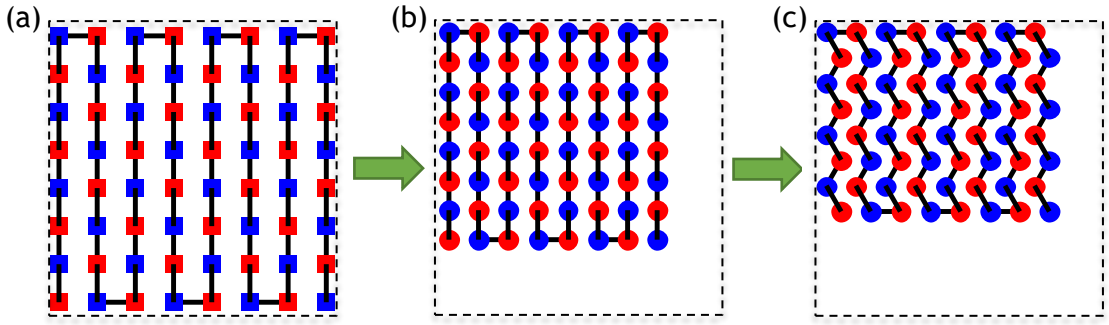


**Figure 42 – (a) Inorganic fabrication techniques typically produce square cross-section TE legs and use serpentine interconnect patterns. (b) Using high resolution printing, circular cross-sections can be fabricated with legs positioned much closer together, resulting in higher fill factors. (c) Even larger fill factors can be achieved by placing the legs in a close-packed structure (hexagonal lattice). The red and blue colors represent p- and n- type materials, respectively.**

To assess the increase in power density that can be obtained using this close-packed layout of legs, the numerical model developed in chapter 4 can be modified to reflect the new device geometry. Again, the input parameters are the material properties of dedoped PEDOT:PSS[19] ($S$ = 72 μV/K, $\sigma$ = 890 S/cm, and $k$ = 0.33) as the p-type material, and a fictitious n-type material with identical properties except for the sign of the Seebeck coefficient. Another input parameter is the use of Kapton films instead of ceramic plates for flexible/wearable devices; all assumptions and input parameters used in this model are listed in Appendix C.1. For fixed hot- and cold-side temperatures of $T_H$ = 400 K and $T_C$ = 300 K (typical for low grade heat recovery), the optimum leg length is found to be around 250 μm, and a power density of over 100 mW/cm$^2$ is obtained at this optimized leg length.[141] This is significantly higher than existing organic TEG prototypes (and higher than that shown in Figure 33 where $F$ = 0.25) indicating that printing close-packed devices

could be beneficial for achieving high performance. Note that this is an upper limit on performance since the practically achievable fill factor is dictated by the printing method.

## 5.3 Space Filling Curves as Interconnect Patterns

In addition to redesigning printed thermoelectric devices by using close-packed layouts for the n- and p-type legs, new interconnect patterns to connect these legs can also be printed. One potential group of patterns that can be utilized as interconnects are space filling curves. Mathematically, space filling curves are defined as mapping functions from points on a unit interval of [0, 1] to the entire two-dimensional unit square; Hilbert curves and Peano curves are two such examples. Recently, it was shown that these curves provide ideal surface conformations and improved elastic mechanics for stretchable electronics.[147]

Of particular interest for thermoelectric applications are Hilbert curves as interconnect patterns as they not only allow for good surface conformation (which is beneficial for wearable devices),[147] but also self-localize (which is beneficial for maintaining a uniform temperature across all the TE legs). A Hilbert curve of order $p$ describes how $4^p$ points are connected. To fabricate a device or module, thermoelectric legs can be positioned in place of these points, and they can be wired together based on the Hilbert pattern. Moreover, a hexagonal layout for positioning TE legs can also accompany the Hilbert curve interconnects, thus allowing for much higher fill factors, as shown in Figure 43. One major benefit of using space filling curves as interconnect patterns in TE modules is that they result in fractal geometries with self-similarity characteristics that allow a module to be divided into sub-modules. Although in theory all space filling curves allow for dividing into sub-modules, the geometry of the resulting sub-modules differ and are dependent on the chosen curve. For instance, following the Hilbert pattern, a module

can be divided into *M* groups of identical parts (*i.e.*, sub-modules) that are connected in parallel, with each consisting of *N* legs wired in series (*i.e.*, *M*x*N* total number of legs). This is advantageous for a number of reasons, as outlined in the following section.

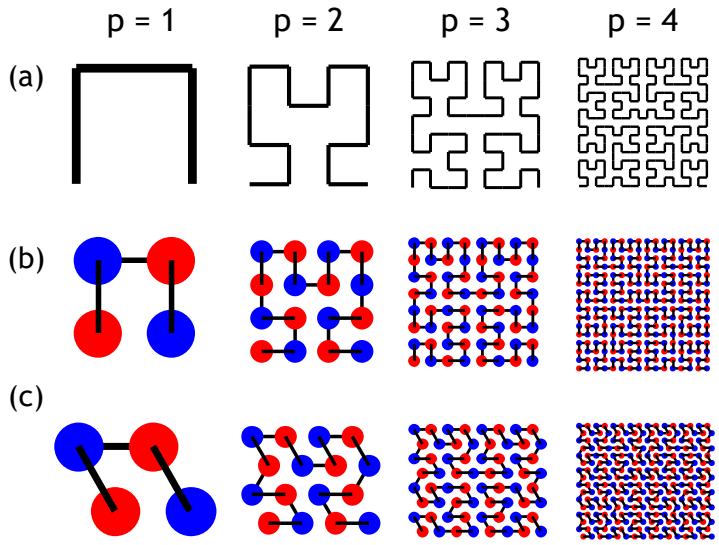


**Figure 43 – From left to right: (a) Hilbert curves of order *p* = one, two, three, and four, which have 4, 16, 64, and 256 legs respectively. (b) Hilbert interconnect patterns can be used to connect TE legs electrically in series where red and blue circles represent n- and p-type materials, respectively. (c) TE legs connected by a Hilbert curve can also be arranged in a hexagonal close-packed layout, thus increasing the fill factor.**

### *5.3.1 Hilbert Patterns Enable Facile Load Matching*

As an illustration of one advantage of these fractal patterns, consider a thermoelectric module containing 1024 legs wired with a Hilbert curve of the fifth order. This can be divided into eleven combinations of *M* and *N* (denoted by (M,N)), as (1,1024), (2,512), (4,256), (8,128), (16,64), (32,32), (64,16), (128,8), (256,4), (512,2), and (1024,1); four of these combinations are shown in Figure 44. Following the concept of tessellating a device into sub-modules, an initial module can be printed such that all legs are connected in series (*i.e.*, (1, *M*x*N*) combination), and then based on the end application, it can be

divided into a desired number of sub-modules connected in parallel. This opens up avenues to tailor the module such that it is load matched to the application; electrical impedance matching[105,107,148] is essential to obtain maximum power from the module (as shown in Figure 39 for the radial device). This is an advantage for printable thermoelectric devices, as these modules are no longer reliant on power conditioning circuits (*e.g.*, DC-DC converters or boost converters) to match the impedance of the module to the application.

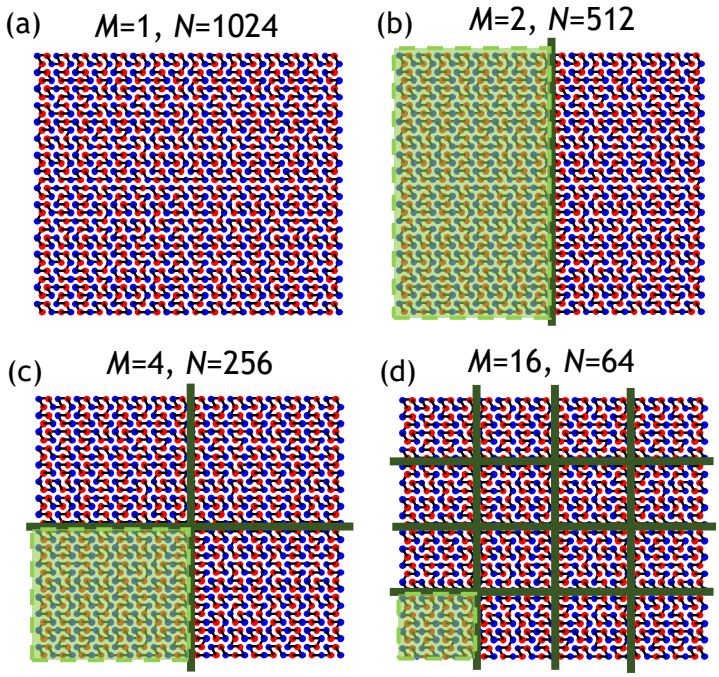


**Figure 44 – The fractal nature of Hilbert curve allows for dividing a thermoelectric module into identical sub-modules that can be readily connected along lines of symmetry in either series, parallel, or a combination thereof. A total of 1024 legs can be connected in eleven different configurations; four examples of these configurations include (a) one module with all legs in series, (b) two parallel sub-modules, with each having 512 legs in series, (c) four parallel sub-modules, with each having 256 legs in series, and (d) sixteen parallel sub-modules, with each having 64 legs in series.**

These wiring rules and interconnect patterns can be extended to close-packed configurations with a large number of legs, as would be the case for organic thermoelectric devices. As an illustration of this concept, a cell is defined based on a four-leg basis (two

p-type legs and two n-type legs) rather than the traditional two-leg basis that is widely used for TE devices. Using this basis, there are four possible unique arrangements of these close-packed legs, resulting in four types of cells as shown in Figure 45. The total number of cells in a module are restricted to multiples of four, resulting in a total number of legs of $4^n$ where $n$ is the order of the Hilbert curve (*e.g.*, $n$ = 1,2,3,…). This allows connecting adjacent cells using a Hilbert curve rather than wiring individual legs. From a macroscopic perspective, the placement pattern of legs appears more random than the traditional serpentine alternating p-n placement used widely, but it does contain deeper order. For instance, a Hilbert curve of order 2 can be used to connect 16 cells comprising 64 thermoelectric legs in total, as shown in Figure 45. The voltage output from this configuration is $V = N\,(2\,S_{p\text{-}n})\,\Delta T$ using the four-leg basis.

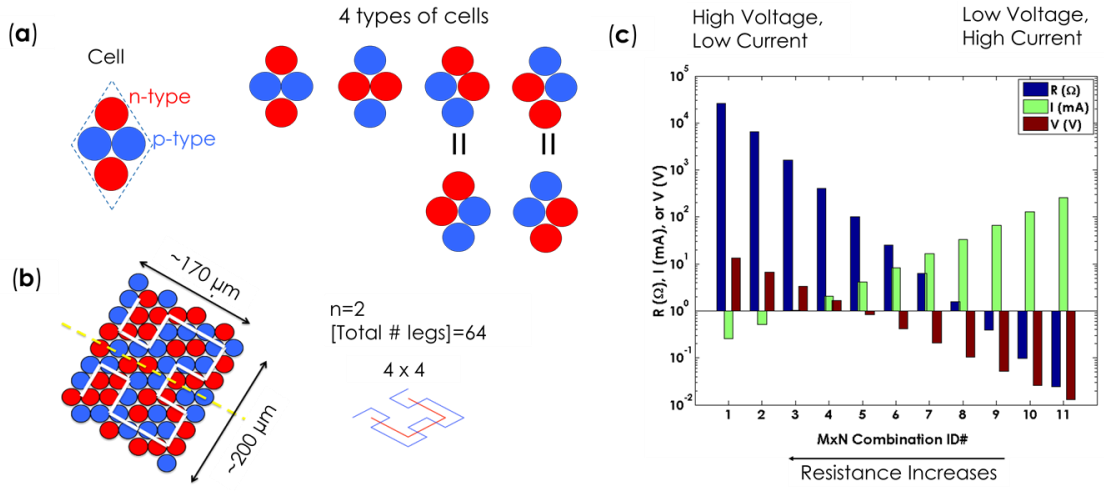


**Figure 45 – (a) A four-leg basis consisting of two n-type and two p-type legs close-packed to form a cell, and the four resulting unique cell configurations, (b) a Hilbert curve of order two connecting eight cells in series to form a TE module, and (c) various combinations of *N* cells in series and *M* groups in parallel for load matching to a range of applications. *M*x*N* combination ID#s from 1 to 11 refer to the following (*M*,*N*) designators, respectively: (1,1024), (2,512), (4,256), (8,128), (16,64), (32,32), (64,16), (128,8), (256,4), (512,2), and (1024,1).**

For a larger number of legs, the module can be tessellated into *N* cells connected in series and *M* groups connected in parallel to obtain several different resistance values, as shown in Figure 45. This in turn yields a TE device that can be electrically impedance matched (also called load matching) to various applications by changing the combinations of *M* and *N*.[141]

### *5.3.2 Hilbert Patterns Enable Uniform Temperatures*

In wearable and flexible thermoelectric devices, the temperature difference may not be uniformly distributed across all the legs (*i.e.*, all legs may not be thermally in parallel). This can lead to a lower device performance as some legs are inactive. In this regard, among all the space-filling curves, the sub-module geometries that are obtained from Hilbert curves result in better utilization of heat because the mapping is localized. Hilbert curves ensure that the closely-spaced points in 1D stay closer together in 2D as well (*i.e.*, they preserve the locality of points).[149] Figure 46 illustrates this concept by graphically comparing two TE modules that have equal fill factors and close-packed positioning of p-n leg pairs, but have different interconnect patterns – one uses the Hilbert curve and the other uses a Peano curve. The number of TE legs that can be connected using a Hilbert curve of order *n* and a Peano curve of order *m* are $4^n$ and $3^{m+1}$, respectively. Therefore, to have a similar number of legs for the modules, a Hilbert curve of order 5 is compared to a Peano curve of order 5, which have 1024 and 729 legs, respectively. Following the cutting lines shown in green in Figure 46, four sub-modules (each having 256 legs) are obtained using the Hilbert curve, and three sub-modules (each having 243 legs) are obtained using the Peano curve. Although the number of legs in the Hilbert sub-module is larger, its geometry provides a better localization for the connected legs by keeping them closer

together. This ensures that all the legs in the sub-module remain thermally in parallel, which is beneficial for device performance. This is another key benefit of using the Hilbert interconnect pattern for TE devices.[141]

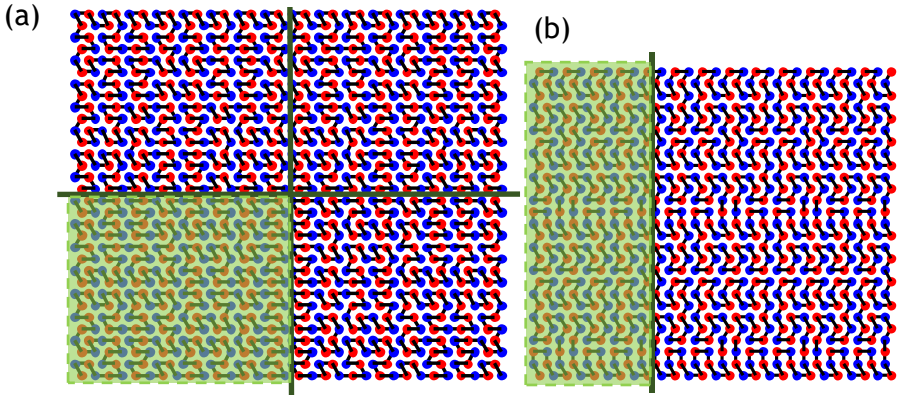


**Figure 46 – (a) The sub-module based on Hilbert curve provides a better localization for the connected TE legs than (b) the one based on Peano curve. The two depicted TE modules have equal fill factors and legs are positioned in a hexagonal close-packed layout. The highlighted areas represent the sub-modules in each system based on the mathematical mapping. Both Hilbert and Peano curves are of the fifth order, resulting in 1024 and 729 total TE legs, respectively.**

## 5.4 Conclusions

The light-weight and flexible nature of polymers makes them suitable for wearable thermoelectric applications. Furthermore, the solution processability of these materials enables new fabrication techniques (such as printing), beyond those developed for inorganic semiconductors. In this chapter, I have demonstrated that by positioning n- and p-type legs in a close-packed hexagonal layout and wiring them based on a Hilbert space-filling curve pattern, better module performance can be achieved. In particular, the close-packed layout increases the fill factor, and the fractal nature of the Hilbert curve pattern allows for tessellation into sub-modules for load-matching to a variety of end applications. Furthermore, the tessellations are naturally more tolerant to non-uniform temperature

distributions as sub-modules are localized in a Hilbert mapping, which is beneficial for wearable electronics. These concepts can be readily implemented in devices that are based on the existing organic TE materials via roll-to-roll printing techniques for large-scale deployment at a low cost for energy harvesting applications at a low cost. Although these concepts were motivated for printable organic TE modules, the hexagonal packing and Hilbert interconnect wiring extend to printable inorganic TE modules as well.[130,134,135,150]

# CHAPTER 6. CONCLUSIONS AND OUTLOOK

Thermoelectric generators enable direct conversion of waste heat into electricity. The realization of commercial thermoelectric devices depends on the simultaneous improvement and optimization of material properties, device design, and material and manufacturing costs. Thermoelectric materials based on conducting polymers are poised to meet these requirements and have recently garnered extensive research interest. A fully functioning thermoelectric device requires both a p-type (hole transporting) and an n-type (electron transporting) material. While high performance p-type polymers have been demonstrated, a scarcity of high performance n-type materials has been a roadblock to realize practical organic thermoelectric devices. To address this, the organic thermoelectrics community has largely focused on long chain-conjugated polymers that have a high negative Seebeck coefficient and low electrical conductivities. As a result, most efforts have been devoted to developing n-type dopants to enhance $\sigma$ through doping studies. However, this approach results in the inherent $S$-$\sigma$ tradeoff that plagues inorganic TEs and renders most n-type polymers air sensitive (de-doping occurs over time when exposed to ambient conditions), thereby making them unsuitable for devices.

In this dissertation, my approach has been to start with a conducting polymer, *i.e.*, metallo-organic polymers such as the NiETT that does not require extrinsic doping, and then make systematic enhancements in thermoelectric properties. In chapters 2 and 3, I have shown that by modifying the synthesis and film processing, the electronic properties of this polymer can be tuned to attain a power factor larger than 10 $\mu W/m\text{-}K^2$, while maintaining its solution processability and air stability (constant TE properties when stored

under ambient conditions). I have also shown that annealing NiETT/PVDF films simultaneously enhances *S* and $\sigma$ owing to morphological and compositional changes, and this has not been reported previously. Specifically, with sodium as the counterion, sub-stoichiometric amounts of Ni(II) and using iodine as the oxidant, the power factor of NiETT/PVDF films approaches 25 μW/m-K$^2$ upon annealing; this represents a significant improvement compared to literature reports of 0.5 μW/m-K$^2$. These systematic enhancements result in one of the highest reported conductivities for an n-type solution processed thin film (~50 S/cm). Furthermore, the observations and insight gained from the ETT study can be extended to other metallo-organic polymers such as the Ni-tetrathiooxalate or NiTTO. This is also a coordinated polymer that is easier to control synthetically as it is polymerized electrochemically. I have obtained preliminary results on thin films of these polymers, which have not been investigated before. Based on the lessons learned from the NiETT studies, a counterion and annealing study are currently underway to demonstrate another n-type polymer with a power factor larger than 10 μW/m-K$^2$, that does not require extrinsic doping and remains stable when stored in ambient conditions.

The development of these n-type polymers is encouraging, but there is also a need for system-level design and optimization for realistic polymer-based thermoelectric devices. This is discussed in chapters 4 and 5 where I have demonstrated two new device designs that are tailored for polymers by leveraging their low thermal conductivity and solution processability. The radial device operates under natural convection alone and eliminates the need for a cold-side heat exchanger, which is a major contributor to the overall system cost. This is enabled by designing around a characteristic thermal length of ~ 4 cm that results in a 10x improvement in power density (100 μW/cm$^2$ – 1 mW/cm$^2$)

compared to a traditional flat plate device when using state-of-the-art material properties. The radial architecture also allows for easy coupling to existing pipes for recovering waste heat and converting it into electricity. Another application area for polymers is body heat harvesting that benefits from their lightweight and flexible nature. For this, thin film TEGs are suitable, but the lower Seebeck coefficient of polymers necessitates the use of a large number of legs (>2000) compared to inorganic devices for the same voltage output. To address this, I have shown that a close-packed layout yields high fill factors (this can be achieved by printing) and consequently large voltage or power densities, while reducing the interconnect resistance. Furthermore, by using a new interconnect pattern based on the Hilbert space filling curve, fractal sub-modules are created that enable facile load matching to various end applications. This is promising for textile-integrated devices, and a prototype demonstration of these concepts on commercial fabrics is currently underway for body heat harvesting. Both the radial TEG and the wearable thin film TEG are new device concepts that are specifically designed for polymers, and offer advantages compared to the traditional flat-plate device that is best suited for inorganic thermoelectric materials.

The advances in n-type polymers presented herein coupled with these new device design concepts could enable the realization of low cost and large-scale organic thermoelectric modules for a variety of energy harvesting applications.

# APPENDIX A. ADDITIONAL INFORMATION ON ETT

## A.1 Evaluation of Inert Binders for ETT Films

To establish the optimal binder/matrix to disperse ETT powders in, two types of film-forming polymers were considered: *(i)* electrically insulating binders and *(ii)* n-type conjugated polymers based on naphthalene diimides (NDIs). The ETT:binder ratio was fixed at 4:1 by weight, and the K(NiETT) exposed to air oxidation for 30 minutes (see section 2.3) was used for all films. The resulting thermoelectric properties of thin films is shown in Table 8 and the different n-type polymers studied are shown in Figure 47.

**Table 8 – Different film forming polymers used in a 4:1 ratio of ETT:binder (w/w).**

| Polymer/Solvent | $\sigma$ (S/cm) | $S$ (μV/K) | $S^2\sigma$ (μW/m-K$^2$) |
|---|---|---|---|
| PVDF/DMSO | 50 | -28 | 4 |
| PMMA/Toluene | 0.001 | -53 | < 0.001 |
| PVA/Water | 0.13 | -55 | 0.04 |
| NDI-1/Toluene | 0.05 | -75 | 0.03 |
| NDI-2/Toluene | 0.03 | -116 | 0.04 |
| NDI-3/Toluene | 0.02 | -113 | 0.02 |

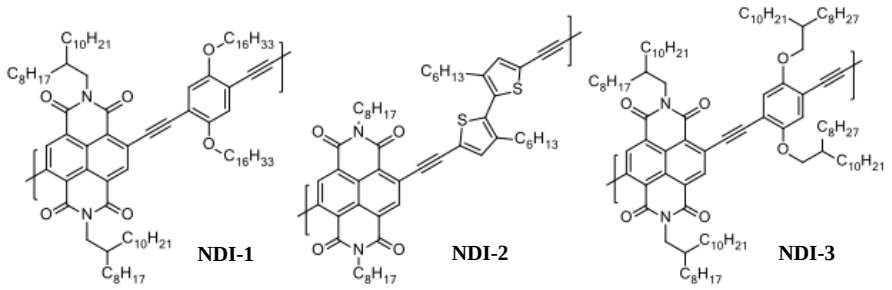


**Figure 47 – N-type polymers investigated as binders are substituted NDI polymers.**

The advantage of using an n-type polymer as the binder instead of PVDF is that we can leverage its high negative thermopower. As a result, ETTs dispersed in the NDI-based polymers show high thermopowers compared to PVDF films. However, PVDF is the best suited matrix for dispersing ETTs as evidenced by the power factor that is largely due to the high conductivity.

## A.2 TGA Data for K(NiETT) Powders

The TGA curves for 24-hour and 30-minute samples are shown in Figure 48. Both samples show an initial 2-4 % weight loss for an isothermal hold at 50 °C. The 30-minute sample appears to be more thermally stable than 24-hour sample indicating that the longer exposure time may result in additional functionalities that are less stable.

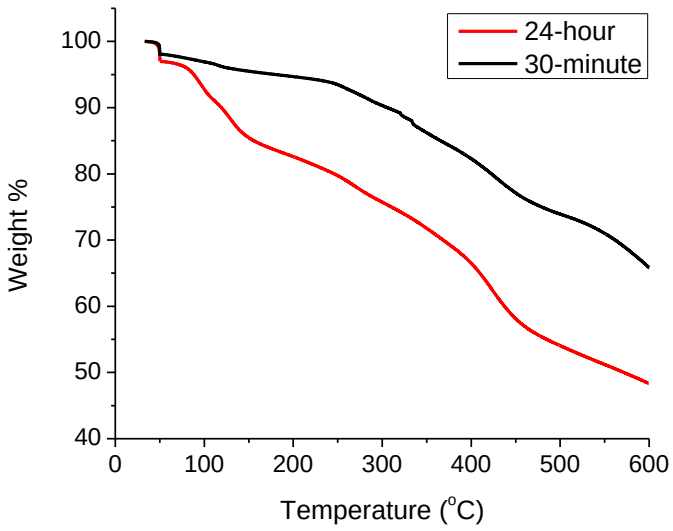


**Figure 48 – TGA mass loss data for K(NiETT) powder samples air-oxidized for 30 minutes and 24 hours.**

## A.3 S2p Elemental Scans from XPS

S2p scans for the iodine-oxidized NiETT samples with different counterions are shown in Figure 49.

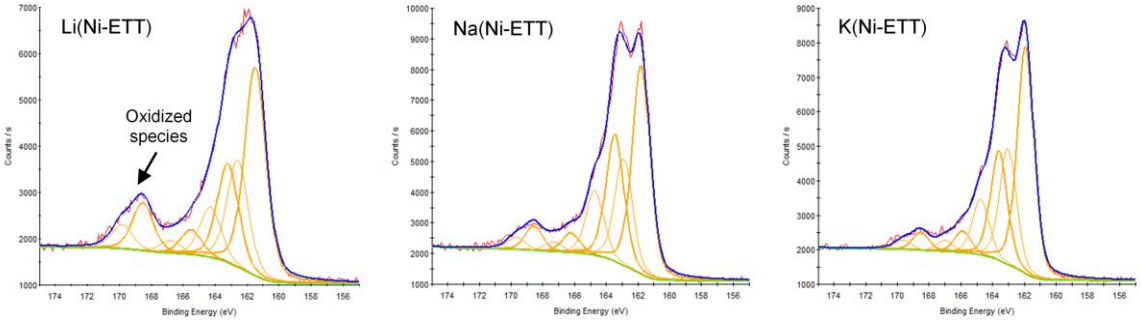


**Figure 49 – S2p peak deconvolution for samples obtained by varying the counterion for iodine-oxidized NiETT powders.**

Figure 50 shows the S2p scans for Na(NiETT) samples with varying oxidant equivalents. The variations in the S2p peaks across all samples shown in these two figures is indicative of a ligand-centered oxidation process for Na(NiETT).

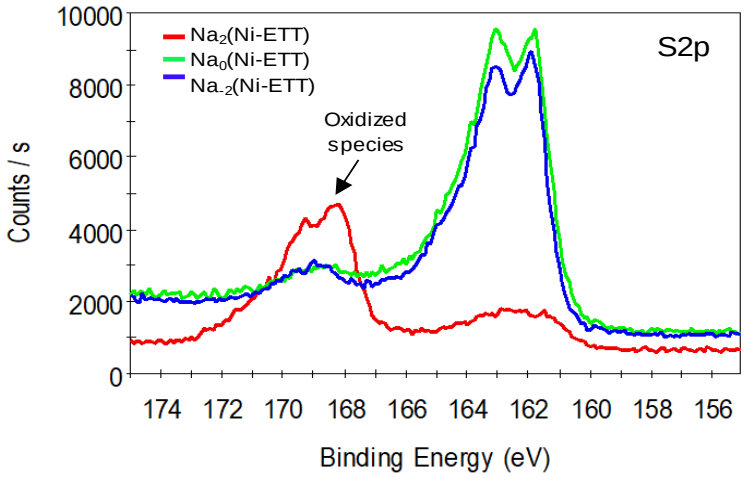


**Figure 50 – Peak comparison (S2p) for oxidation study of Na(NiETT) powder samples.**

## A.4 Ni2p Elemental Scans from XPS

$$\%\ Ni\ \text{Incorporation} = \frac{(Mass\ Percent\ Ni\ [\%]) \times (Mass\ of\ NiETT\ [mg])}{(Ni(II)OAc_2\ [mmol]) \times (Atomic\ Mass\ Ni\ [\frac{mg}{mmol}])}$$

Table 9 shows the Ni2p deconvolution into three statistically valid peaks. The XPS scans across all samples (different counterions, different nickel amounts, different oxidant amounts) are identical indicating that the Ni2p binding environment remains the same with these synthesis modifications. Figure 51 shows the deconvolution curves.

**Table 9 – Representative Ni2p peak deconvolution for Na(NiETT).**

| Peak position (eV) | FWHM (eV) | Atomic % |
|---|---|---|
| 853.38 | 1.8 | 57.44 |
| 855.08 | 3.2 | 27.92 |
| 859.6 | 3.5 | 14.64 |

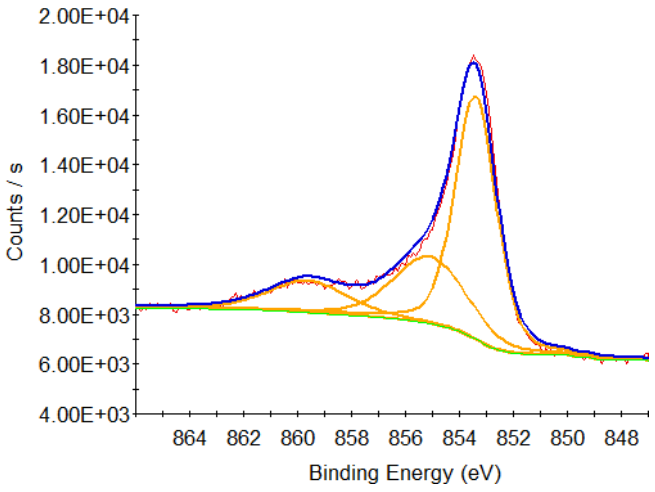


**Figure 51 – Ni2p peak deconvolution for Na(NiETT) powder samples.**

# APPENDIX B. RADIAL DEVICE DESIGN DERIVATIONS

## B.1 Geometry Matching and *Module ZT* to *Material zT*

The thermoelectric module figure-of-merit is defined for one p-n couple. For a device with $N$ pairs of legs connected electrically in series with minor modifications:

$$ZT = \frac{\left(NS_p - NS_n\right)^2 T}{\left(NK_{TE}\right)\left(NR_{TE}\right)} = \frac{S_{p-n}{}^2 T}{K_{TE} R_{TE}} \tag{17}$$

under the approximations that there is no parallel leakage heat loss (*i.e.*, $K_{||} = 0$ and $K_T = K_{TE}$) and the electrical contact and interconnect resistances are negligible. The above equation is a function of $K_{TE}R_{TE}$; therefore, the minimum value of $K_{TE}R_{TE}$ is sought to maximize the efficiency.

$$K_{TE}R_{TE} = \frac{k_p}{\sigma_p} + \left(\frac{k_n}{\sigma_p}\right)\left(\frac{A_n L_p}{A_p L_n}\right) + \left(\frac{k_p}{\sigma_n}\right)\left(\frac{A_p L_n}{A_n L_p}\right) + \frac{k_n}{\sigma_n} \tag{18}$$

where the length, $L_i = \ln(r_{out,i} / r_{in,i})$ and the cross-sectional area, $A_i = 2\pi t_i$ (*i.e.*, $i = p$ for p-type leg) which may differ for the n- and p-type material. Minimizing above equation by taking the derivative with respect to $A_nL_p/A_pL_n$ and setting the result equal to zero yields the condition:

$$\left(\frac{A_n L_p}{A_p L_n}\right) = \left(\frac{\sigma_p k_p}{\sigma_n k_n}\right)^{1/2} \tag{19}$$

Substituting the $L_i$ and $A_i$ values yields the geometry matching condition.

$$\frac{t_n \ln\left(r_{out,p} / r_{in,p}\right)}{t_p \ln\left(r_{out,n} / r_{in,n}\right)} = \sqrt{\frac{k_p \sigma_p}{k_n \sigma_n}} \tag{20}$$

This condition minimizes the product $K_{TE}R_{TE}$

$$\left(K_{TE}R_{TE}\right)_{min} = \left[\left(\frac{k_n}{\sigma_n}\right)^{1/2} + \left(\frac{k_p}{\sigma_p}\right)^{1/2}\right]^2 \tag{21}$$

The maximum value of $ZT$ can be expressed as

$$Z_{max}T = \frac{\left(s_p - s_n\right)^2 T}{\left[\left(\frac{k_n}{\sigma_n}\right)^{1/2} + \left(\frac{k_p}{\sigma_p}\right)^{1/2}\right]^2} \tag{22}$$

with the simplifications $k_n = k_p = k$, $\sigma_n = \sigma_p = \sigma$, and $S_p = -S_n = S$, the *material* figure-of-merit results:

$$zT = \frac{S^2 \sigma T}{k} \tag{23}$$

## B.2 Critical Radius to Maximize Heat Flux

Consider the classical radial heat transfer problem with a cylinder of inner radius $r_{in}$ and arbitrary outer radius $r_{out}$ without heat generation.[115] The steady-state heat equation and temperature distribution are:

$$\frac{1}{r}\frac{d}{dr}\left(kr\frac{dT}{dr}\right)=0 \tag{24}$$

$$T(r)=C_1\ln\left(r\right)+C_2 \tag{25}$$

To obtain the integration constants, the following boundary conditions are applied corresponding to a fixed inner surface temperature and convection along the outer surface:

$$T(r=r_{in})=T_H \tag{26}$$

$$-k\frac{dT}{dr}=h(T(r)-T_C) \tag{27}$$

This can be solved to obtain the temperature profile and temperature difference across the device for a radial geometry:

$$\Delta T_{radial}=T_1-T_2=\frac{T_H-T_C}{\left(\frac{k/h}{r\ln\left(r/r_{in}\right)}+1\right)} \tag{28}$$

A similar expression can be derived for flat-plate geometry as:

$$\Delta T_{flat-plate}=T_1-T_2=\frac{T_H-T_C}{\left(\frac{k/h}{l}+1\right)} \tag{29}$$

The heat flux (with respect to the inner cylinder) then becomes:

$$q''(r)=\frac{q(r)}{2\pi r_{in}t}=\frac{h(T_H-T_C)}{\frac{r_{in}}{r}+\frac{r_{in}}{k/h}\ln\left(\frac{r}{r_{in}}\right)} \tag{30}$$

The outer radius that maximizes this heat flux is the characteristic thermal length:

$$r = \frac{k}{h} \equiv L_T \tag{31}$$

This is analogous to the concept of a critical insulation thickness[115] with critical radius being the characteristic thermal length, $L_T$.

## B.3 Thermal Impedance Matching

Consider a radial TEG operating under a thermally impedance matched condition, (*i.e.*, the thermal resistance or conductance) of the TE module is matched to that of the cold-side heat exchanger. Assume negligible resistance of the hot-side heat exchanger and identical material properties for the p-type and n-type. This is written as:

$$\frac{\ln\left(r_{out} / r_{in}\right)}{2\pi k_{eff}\left(t_p + t_n\right)} = \frac{1}{h\left[2\pi r_{out}\left(t_p + t_n\right)\right]} \tag{32}$$

where $k_{eff}$ is the effective thermal conductivity of the TE material, and can be simplified to obtain the following:

$$\ln\left(\frac{r_{out}}{r_{in}}\right) = \left(\frac{1}{r_{out}}\right)\frac{k_{eff}}{h} \equiv \left(\frac{1}{r_{out}}\right)L_T \tag{33}$$

Figure 52 shows the thermal conductance of the hot- and cold-side heat exchangers, conductance of the TE material, and the parallel leakage conductance from the substrate and separator as a function of leg length. As the leg length increases, the cold-side conductance also increases while the TE and leakage conductance decrease. The cold-side and TE conductance are matched at $L_{match}$ = 1.7 cm, which corresponds to the thermal impedance matching condition for a realistic device. This agrees reasonably well (within

20%) with the approximate result derived from a purely thermal model. This is expected in the low *zT* limit for polymers considered in this model, which is well approximated by the thermal network.

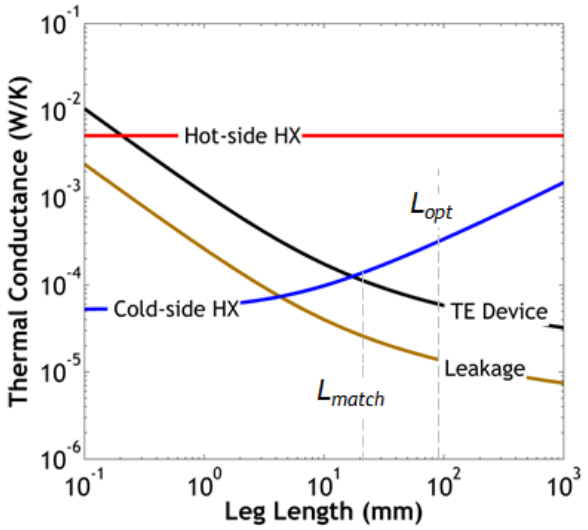


**Figure 52 – Thermal conductance as a function of leg length showing hot- and cold-side heat exchanger conductances ($K_H$ and $K_C$ respectively), conductance of the TE material ($K_{TE} = K_p + K_n$), and leakage conductance from the substrate and separator ($K_{\|}$). Dashed lines correspond to analytical leg lengths for thermal impedance matching and maximum power.**

### B.4 Optimum leg length to maximize power density

Consider a device with unmatched conductances for the TE material and heat exchangers when operating with natural convection. Rewriting the power equation as:

$$P \approx \pi\left(t\sigma {S_{p-n}}^2 \left(T_H - T_C\right)^2\right)\left(\frac{m}{(1+m)^2}\right)\left(\frac{\ln(r_{out}/r_{in})}{\left(\ln(r_{out}/r_{in}) + \left(L_T/r_{out}\right)\right)^2}\right) \tag{34}$$

Define non-dimensional quantities $\tilde{r} = r_{out} / r_{in}$ and $\tilde{l} = L_T / r_{in}$; minimize the denominator containing geometry terms in the above equation to obtain the leg length that maximizes power density.

$$\frac{d}{d\tilde{r}}\left( \frac{\ln \tilde{r}}{\left[ \ln \tilde{r} + \left( \tilde{l} / \tilde{r} \right) \right]^2} \right) = 0 \tag{35}$$

Apply the quotient chain rule and simplify the expression to obtain the following:

$$\tilde{l} = \tilde{r} \ln \tilde{r} - 2\tilde{l} \ln \tilde{r} \tag{36}$$

Plug-in the non-dimensional quantities and simplify to obtain the optimum leg length that maximizes power density:

$$\ln\left( \frac{r_{out}}{r_{in}} \right) = \left( \frac{1}{r_{out} - 2L_T} \right) L_T \tag{37}$$

## B.5 Convection Heat Transfer

The long horizontal cylinder correlation is used to evaluate the convective heat transfer coefficient[115] for natural/free convection for the cold-side heat exchanger:

$$\overline{Nu_D} = \left\{ 0.60 + \frac{0.387 Ra_D^{1/6}}{\left[ 1 + \left( 0.559 / Pr \right)^{9/16} \right]^{8/27}} \right\}^2 \tag{38}$$

where $\overline{Nu_D}$ is the average Nusselt number, $Ra_D$ is the Rayleigh number, and $Pr$ is the Prandtl number. For air as the working fluid, all these properties are calculated at a mean temperature.

# APPENDIX C. WEARABLE DEVICE DESIGN DERIVATIONS

## C.1 Power Density and Optimum Leg Length

To assess the increase in power density that can potentially be obtained using the close-packed layout of p- and n-type legs, a numerical model was developed. As an illustration, properties of dedoped PEDOT:PSS[19] ($S$ = 72 μV/K, $\sigma$ = 890 S/cm, and $k$ = 0.33 W/m-K) was used as the p-type material, and a fictitious n-type material with identical properties except for the sign of the Seebeck coefficient was used. The leg length is the design variable to optimize device geometry and performance. All input parameters used in this model are listed in Table 10.

**Table 10 – Input parameters used for power and optimum leg length calculations**

| Parameter | Value |
|---|---|
| Hot side temperature | 400 K |
| Cold side temperature | 300 K |
| TE Leg diameter | 20 μm |
| Fill Factor | $\pi/2\sqrt{3}$ |
| Electrical contact resistance | $1\text{x}10^{-10}$ Ω-m$^2$ |
| Thickness of interconnects (copper) | 25.4 μm |
| Thermal conductivity of interconnects (copper) | 400 W/m-K |
| Thickness of Kapton film (polyimide) | 75 μm |
| Thermal conductivity of Kapton (polyimide) | 0.45 W/m-K |
| Electrical conductivity of interconnects (copper) | $1.7 \times 10^{-8}$ Ω-m |
| Heat transfer coefficient for hot- and cold-side | 5000 W/m$^2$-K |
| Air thermal conductivity | 0.03 W/m-K |

## C.2 Fill Factor for a 2D Hexagonal Close-Packed Structure

Figure 53 shows a 2D hexagonal close-packed structure. The fill factor, *F* for such a layout can be calculated using the parallelogram shown. All the circles (*i.e.*, TE legs) shown in the figure have a diameter equal to *D*. The calculation can be carried out as follows:

$$F = \frac{\pi D^2/4}{D \times D \times \sin(2\pi/3)} = \frac{\pi}{2\sqrt{3}} \approx 90.6\ \%$$

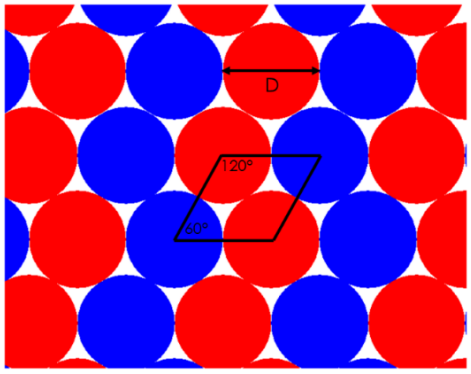


**Figure 53 – The 2D hexagonal close-packed structure.**

# REFERENCES


1 Bell, L. E. Cooling, Heating, Generating Power, and Recovering Waste Heat with Thermoelectric Systems. *Science* **321**, 1457 (2008).

2 Zebarjadi, M., Esfarjani, K., Dresselhaus, M. S., Ren, Z. F. & Chen, G. Perspectives on thermoelectrics: from fundamentals to device applications. *Energy & Environmental Science* **5**, 5147-5162, doi:10.1039/C1EE02497C (2012).

3 Rowe, D. *Thermoelectrics Handbook*. (CRC Press, 2006).

4 Baranowski, L. L., Snyder, G. J. & Toberer, E. S. Concentrated solar thermoelectric generators. *Energy & Environmental Science* **5**, 9055-9067, doi:10.1039/C2EE22248E (2012).

5 Telkes, M. Solar Thermoelectric Generators. *Journal of Applied Physics* **25**, 765-777, doi:doi:http://dx.doi.org/10.1063/1.1721728 (1954).

6 Waste Heat Recovery Systems - Technology Assessments. (U.S. Department of Energy, 2015).

7 Sales, B. C. Electron Crystals and Phonon Glasses: A New Path to Improved Thermoelectric Materials. *MRS Bulletin* **23**, 15-21, doi:10.1557/S0883769400031419 (2013).

8 Snyder, G. J. & Toberer, E. S. Complex thermoelectric materials. *Nature Materials* **7**, 105, doi:10.1038/nmat2090 (2008).

9 Mahan, G. D. in *Solid State Physics* Vol. 51 (ed Henry; Spaepen Ehrenreich, Frans ) 81–157 (Academic Press, 1997).

10 Mahan, G. D. & Sofo, J. O. The best thermoelectric. *Proceedings of the National Academy of Sciences* **93**, 7436 (1996).

11 Zhao, L.-D. *et al.* High Thermoelectric Performance via Hierarchical Compositionally Alloyed Nanostructures. *Journal of the American Chemical Society* **135**, 7364-7370, doi:10.1021/ja403134b (2013).

12 Zhao, L.-D. *et al.* Ultralow thermal conductivity and high thermoelectric figure of merit in SnSe crystals. *Nature* **508**, 373-377, doi:10.1038/nature13184 (2014).

13 Faleev, S. V. & Léonard, F. Theory of enhancement of thermoelectric properties of materials with nanoinclusions. *Physical Review B* **77**, 214304 (2008).

14 Bubnova, O. & Crispin, X. Towards polymer-based organic thermoelectric generators. *Energy & Environmental Science* **5**, 9345-9362, doi:10.1039/C2EE22777K (2012).

15 Yee, S. K., Coates, N. E., Majumdar, A., Urban, J. J. & Segalman, R. A. Thermoelectric power factor optimization in PEDOT:PSS tellurium nanowire hybrid composites. *Physical Chemistry Chemical Physics* **15**, 4024-4032, doi:10.1039/C3CP44558E (2013).

16 Zhang, Q., Sun, Y., Xu, W. & Zhu, D. Organic Thermoelectric Materials: Emerging Green Energy Materials Converting Heat to Electricity Directly and Efficiently. *Advanced Materials* **26**, 6829-6851, doi:10.1002/adma.201305371 (2014).

17 Poehler, T. O. & Katz, H. E. Prospects for polymer-based thermoelectrics: state of the art and theoretical analysis. *Energy & Environmental Science* **5**, 8110-8115, doi:10.1039/C2EE22124A (2012).

18 Bubnova, O. *et al.* Optimization of the thermoelectric figure of merit in the conducting polymer poly(3,4-ethylenedioxythiophene). *Nat Mater* **10**, 429-433, doi:10.1038/nmat3012 (2011).

19 Kim, G. H., Shao, L., Zhang, K. & Pipe, K. P. Engineered doping of organic semiconductors for enhanced thermoelectric efficiency. *Nat Mater* **12**, 719-723, doi:10.1038/nmat3635 (2013).

20 Hiroshige, Y., Ookawa, M. & Toshima, N. Thermoelectric figure-of-merit of iodine-doped copolymer of phenylenevinylene with dialkoxyphenylenevinylene. *Synthetic Metals* **157**, 467-474, doi:http://dx.doi.org/10.1016/j.synthmet.2007.05.003 (2007).

21 Kim, D., Kim, Y., Choi, K., Grunlan, J. C. & Yu, C. Improved Thermoelectric Behavior of Nanotube-Filled Polymer Composites with Poly(3,4-ethylenedioxythiophene) Poly(styrenesulfonate). *ACS Nano* **4**, 513-523, doi:10.1021/nn9013577 (2010).

22 Lu, B.-Y. *et al.* Thermoelectric Performances of Free-Standing Polythiophene and Poly(3-Methylthiophene) Nanofilms. *Chinese Physics Letters* **27**, 057201 (2010).

23 Sun, Y. *et al.* Organic Thermoelectric Materials and Devices Based on p- and n-Type Poly(metal 1,1,2,2-ethenetetrathiolate)s. *Advanced Materials* **24**, 932-937, doi:10.1002/adma.201104305 (2012).

24 Culebras, M., Gomez, C. M. & Cantarero, A. Enhanced thermoelectric performance of PEDOT with different counter-ions optimized by chemical reduction. *Journal of Materials Chemistry A* **2**, 10109-10115, doi:10.1039/C4TA01012D (2014).

25 Yao, Q., Wang, Q., Wang, L. & Chen, L. Abnormally enhanced thermoelectric transport properties of SWNT/PANI hybrid films by the strengthened PANI

molecular ordering. *Energy & Environmental Science* **7**, 3801-3807, doi:10.1039/C4EE01905A (2014).

26 Mott, N. F. D., E. A. *Electronic Processes in Non-Crystalline Materials*. 2nd edn, (Oxford University Press, 1979).

27 Mott, N. F. (ed O. Madelung) 22-45 (Springer Berlin Heidelberg, 1969).

28 Noriega, R. *et al.* A general relationship between disorder, aggregation and charge transport in conjugated polymers. *Nature Materials* **12**, 1038, doi:10.1038/nmat3722 (2013).

29 Abdalla, H., Zuo, G. & Kemerink, M. Range and energetics of charge hopping in organic semiconductors. *Physical Review B* **96**, 241202 (2017).

30 Russ, B., Glaudell, A., Urban, J. J., Chabinyc, M. L. & Segalman, R. A. Organic thermoelectric materials for energy harvesting and temperature control. *Nature Reviews Materials* **1**, 16050, doi:10.1038/natrevmats.2016.50 (2016).

31 Kang, S. D. & Snyder, G. J. Charge-transport model for conducting polymers. *Nature Materials* **16**, 252, doi:10.1038/nmat4784 (2016).

32 Glaudell, A. M., Cochran, J. E., Patel, S. N. & Chabinyc, M. L. Impact of the Doping Method on Conductivity and Thermopower in Semiconducting Polythiophenes. *Advanced Energy Materials* **5**, 1401072, doi:10.1002/aenm.201401072 (2015).

33 Kaiser, A. B. & Skakalova, V. Electronic conduction in polymers, carbon nanotubes and graphene. *Chemical Society Reviews* **40**, 3786-3801, doi:10.1039/C0CS00103A (2011).

34 Kaiser, A. B. Thermoelectric power and conductivity of heterogeneous conducting polymers. *Physical Review B* **40**, 2806-2813 (1989).

35 Chaikin, P. M. & Beni, G. Thermopower in the correlated hopping regime. *Physical Review B* **13**, 647-651 (1976).

36 Hill, R. M. Variable-range hopping. *physica status solidi (a)* **34**, 601-613, doi:10.1002/pssa.2210340223 (1976).

37 Baranovskii, S. D., Zvyagin, I. P., Cordes, H., Yamasaki, S. & Thomas, P. Percolation Approach to Hopping Transport in Organic Disordered Solids. *physica status solidi (b)* **230**, 281-288, doi:10.1002/1521-3951(200203)230:1<281::AID-PSSB281>3.0.CO;2-W (2002).

38 See, K. C. *et al.* Water-Processable Polymer−Nanocrystal Hybrids for Thermoelectrics. *Nano Letters* **10**, 4664-4667, doi:10.1021/nl102880k (2010).

39 He, M. *et al.* Thermopower enhancement in conducting polymer nanocomposites via carrier energy scattering at the organic-inorganic semiconductor interface. *Energy & Environmental Science* **5**, 8351-8358, doi:10.1039/C2EE21803H (2012).

40 Tong, T. & Majumdar, A. Reexamining the 3-omega technique for thin film thermal characterization. *Review of Scientific Instruments* **77**, 104902, doi:doi:http://dx.doi.org/10.1063/1.2349601 (2006).

41 Schmidt, A. J., Cheaito, R. & Chiesa, M. A frequency-domain thermoreflectance method for the characterization of thermal properties. *Review of Scientific Instruments* **80**, 094901, doi:doi:http://dx.doi.org/10.1063/1.3212673 (2009).

42 Regner, K. T., Majumdar, S. & Malen, J. A. Instrumentation of broadband frequency domain thermoreflectance for measuring thermal conductivity accumulation functions. *Review of Scientific Instruments* **84**, 064901, doi:doi:http://dx.doi.org/10.1063/1.4808055 (2013).

43 Feser, J. P. & Cahill, D. G. Probing anisotropic heat transport using time-domain thermoreflectance with offset laser spots. *Review of Scientific Instruments* **83**, 104901, doi:10.1063/1.4757863 (2012).

44 Cahill, D. G. Thermal conductivity measurement from 30 to 750 K: the 3ω method. *Review of Scientific Instruments* **61**, 802-808, doi:10.1063/1.1141498 (1990).

45 Dames, C. & Chen, G. 1ω, 2ω, and 3ω methods for measurements of thermal properties. *Review of Scientific Instruments* **76**, 124902, doi:10.1063/1.2130718 (2005).

46 Liu, J. *et al.* Simultaneous measurement of thermal conductivity and heat capacity of bulk and thin film materials using frequency-dependent transient thermoreflectance method. *Review of Scientific Instruments* **84**, 034902, doi:http://dx.doi.org/10.1063/1.4797479 (2013).

47 Malen, J. A. *et al.* Optical Measurement of Thermal Conductivity Using Fiber Aligned Frequency Domain Thermoreflectance. *Journal of Heat Transfer* **133**, 081601-081601, doi:10.1115/1.4003545 (2011).

48 Van Der Pauw, L. J. A method of measuring specific resistivity and hall effect of disks of arbitrary shape. *Philips Res. Rep.* **13**, 1-9 (1958).

49 Bahk, J.-H. F., Tela; Shakouri, Ali. in *Annual Review of Heat Transfer* (Begell House, Inc., 2013).

50 Sun, Y. *et al.* Flexible n-Type High-Performance Thermoelectric Thin Films of Poly(nickel-ethylenetetrathiolate) Prepared by an Electrochemical Method. *Advanced Materials* **28**, 3351-3358, doi:10.1002/adma.201505922 (2016).

51 Fukumaru, T., Fujigaya, T. & Nakashima, N. Development of n-type cobaltocene-encapsulated carbon nanotubes with remarkable thermoelectric property. *Scientific Reports* **5**, 7951, doi:10.1038/srep07951 (2015).

52 Menke, T., Ray, D., Meiss, J., Leo, K. & Riede, M. In-situ conductivity and Seebeck measurements of highly efficient n-dopants in fullerene C60. *Applied Physics Letters* **100**, 093304, doi:10.1063/1.3689778 (2012).

53 Inabe, T. *et al.* Electronic structure of alkali metal doped C60 derived from thermoelectric power measurements. *Physical Review Letters* **69**, 3797-3799 (1992).

54 Wang, Z. H. *et al.* Electronic transport properties of KxC70 thin films. *Physical Review B* **48**, 10657-10660 (1993).

55 Schlitz, R. A. *et al.* Solubility-Limited Extrinsic n-Type Doping of a High Electron Mobility Polymer for Thermoelectric Applications. *Advanced Materials* **26**, 2825-2830, doi:10.1002/adma.201304866 (2014).

56 Russ, B. *et al.* Power Factor Enhancement in Solution-Processed Organic n-Type Thermoelectrics Through Molecular Design. *Advanced Materials* **26**, 3473-3477, doi:10.1002/adma.201306116 (2014).

57 Shi, K. *et al.* Toward High Performance n-Type Thermoelectric Materials by Rational Modification of BDPPV Backbones. *Journal of the American Chemical Society* **137**, 6979-6982, doi:10.1021/jacs.5b00945 (2015).

58 Huang, D. *et al.* Conjugated-Backbone Effect of Organic Small Molecules for n-Type Thermoelectric Materials with ZT over 0.2. *Journal of the American Chemical Society* **139**, 13013-13023, doi:10.1021/jacs.7b05344 (2017).

59 Yuan, D. *et al.* Efficient Solution-Processed n-Type Small-Molecule Thermoelectric Materials Achieved by Precisely Regulating Energy Level of Organic Dopants. *ACS Applied Materials & Interfaces* **9**, 28795-28801, doi:10.1021/acsami.7b07282 (2017).

60 Huang, D. *et al.* Bismuth Interfacial Doping of Organic Small Molecules for High Performance n-type Thermoelectric Materials. *Angewandte Chemie International Edition* **55**, 10672-10675, doi:10.1002/anie.201604478 (2016).

61 Wang, S. *et al.* Thermoelectric Properties of Solution-Processed n-Doped Ladder-Type Conducting Polymers. *Advanced Materials* **28**, 10764-10771, doi:10.1002/adma.201603731 (2016).

62 Zuo, G., Li, Z., Wang, E. & Kemerink, M. High Seebeck Coefficient and Power Factor in n-Type Organic Thermoelectrics. *Advanced Electronic Materials* **4**, 1700501, doi:10.1002/aelm.201700501 (2018).

63 Jiao, F. *et al.* Inkjet-printed flexible organic thin-film thermoelectric devices based on p- and n-type poly(metal 1,1,2,2-ethenetetrathiolate)s/polymer composites through ball-milling. *Philosophical Transactions of the Royal Society A: Mathematical, Physical and Engineering Sciences* **372**, 20130008 (2014).

64 Yoshioka, N., Nishide, H., Inagaki, K., Inagaki, K. & Tsuchida, E. Electrical conductive and magnetic properties of conjugated tetrathiolate nickel polymers. *Polymer Bulletin* **23**, 631-636, doi:10.1007/BF01033109 (1990).

65 Vogt, T. *et al.* A LAXS (large angle x-ray scattering) and EXAFS (extended x-ray absorption fine structure) investigation of conductive amorphous nickel tetrathiolato polymers. *Journal of the American Chemical Society* **110**, 1833-1840, doi:10.1021/ja00214a028 (1988).

66 Vicente, R., Ribas, J., Cassoux, P. & Valade, L. Synthesis, characterization and properties of highly conducting organometallic polymers derived from the ethylene tetrathiolate anion. *Synthetic Metals* **13**, 265-280, doi:http://dx.doi.org/10.1016/0379-6779(86)90188-8 (1986).

67 Holdcroft, G. E. & Underhill, A. E. Preparation and electrical conduction properties of polymeric transition metal complexes of 1,1,2,2-ethenetetrathiolate ligand. *Synthetic Metals* **10**, 427-434, doi:http://dx.doi.org/10.1016/0379-6779(85)90200-0 (1985).

68 Poleschner, H., John, W., Hoppe, F., Fanghänel, E. & Roth, S. Tetrathiafulvalene. XIX. Synthese und Eigenschaften elektronenleitender Poly-Dithiolenkomplexe mit Ethylentetrathiolat und Tetrathiafulvalentetrathiolat als Brückenliganden. *Journal für Praktische Chemie* **325**, 957-975, doi:10.1002/prac.19833250612 (1983).

69 Q. Sun, S., Zhang, B., J. Wu, P. & B. Zhu, D. Crystal structure of bis(tetraethylammonium) bis[4,5-disulfanyl-1,3-dithiol-2-onato(2-)]nickelate(II) and spectroscopic and electrical properties of related oxidized complexes. *Journal of the Chemical Society, Dalton Transactions*, 277-282, doi:10.1039/A604434D (1997).

70 Sheng, P. *et al.* A novel cuprous ethylenetetrathiolate coordination polymer: Structure characterization, thermoelectric property optimization and a bulk thermogenerator demonstration. *Synthetic Metals* **193**, 1-7, doi:http://dx.doi.org/10.1016/j.synthmet.2014.03.024 (2014).

71 Stepien, L., Roch, A., Tkachov, R. & Gedrange, T. in *Thermoelectrics for Power Generation - A Look at Trends in the Technology* (eds Sergey Skipidarov & Mikhail Nikitin) Ch. 03 (InTech, 2016).

72 Oshima, K., Asano, H., Shiraishi, Y. & Toshima, N. Dispersion of carbon nanotubes by poly(Ni-ethenetetrathiolate) for organic thermoelectric hybrid materials. *Jpn J Appl Phys* **55** (2016).

73 Toshima, N. *et al.* Novel Hybrid Organic Thermoelectric Materials: Three-Component Hybrid Films Consisting of a Nanoparticle Polymer Complex, Carbon Nanotubes, and Vinyl Polymer. *Advanced Materials* **27**, 2246-2251 (2015).

74 Asano, H., Sakura, N., Oshima, K., Shiraishi, Y. & Toshima, N. Development of ethenetetrathiolate hybrid thermoelectric materials consisting of cellulose acetate and semiconductor nanomaterials. *Jpn J Appl Phys* **55** (2016).

75 Sheng, P. *et al.* Optimization of the thermoelectric properties of poly[Cux(Cu-ethylenetetrathiolate)]. *Synthetic Metals* **188**, 111-115, doi:10.1016/j.synthmet.2013.12.004 (2014).

76 Menon, A. K. *et al.* Metallo-organic n-type thermoelectrics: Emphasizing advances in nickel-ethenetetrathiolates. *Journal of Applied Polymer Science* **134**, 44402, doi:10.1002/app.44402 (2017).

77 Avantage Software (Thermo Scientific).

78 Wagner, C. D. & Muilenberg, G. E. *Handbook of x-ray photoelectron spectroscopy: a reference book of standard data for use in x-ray photoelectron spectroscopy*. (Physical Electronics Division, Perkin-Elmer Corp., 1979).

79 Database, N. X.-r. P. S. <http://srdata.nist.gov/xps/Default.aspx> (

80 Liu, S.-G., Liu, Y.-Q. & Zhu, D.-B. Preparation and spectral properties of new molecular conductors based on anion salt. *Synthetic Metals* **89**, 187-191, doi:10.1016/s0379-6779(97)81216-7 (1997).

81 Ratner, B. D. & Castner, D. G. in *Surface Analysis – The Principal Techniques* 47-112 (John Wiley & Sons, Ltd, 2009).

82 Briggs, D. *Surface Analysis of Polymers by XPS and Static SIMS*. (Cambridge University Press, 1998).

83 Mueller-Westerhoff, U. T., Vance, B. & Ihl Yoon, D. The synthesis of dithiolene dyes with strong near-IR absorption. *Tetrahedron* **47**, 909-932, doi:http://dx.doi.org/10.1016/S0040-4020(01)80932-7 (1991).

84 Shiozaki, H., Nakazumi, H., Morikawa, T., Sato, Y. & Kitao, T. XPS study of bis(1,2-diaryl-1,2-ethylenedithiolato)nickels. *Bulletin of the Chemical Society of Japan* **63**, 646-648, doi:10.1246/bcsj.63.646 (1990).

85 Best, S. A. *et al.* X-ray photoelectron spectra of inorganic molecules. 18. Observations on sulfur 2p binding energies in transition metal complexes of sulfur-containing ligands. *Inorganic Chemistry* **16**, 1976-1979, doi:10.1021/ic50174a030 (1977).

86 Mekhalif, Z., Riga, J., Pireaux, J. J. & Delhalle, J. Self-Assembled Monolayers of n-Dodecanethiol on Electrochemically Modified Polycrystalline Nickel Surfaces. *Langmuir* **13**, 2285-2290, doi:10.1021/la960528a (1997).

87 Tortech, L., Mekhalif, Z., Delhalle, J., Guittard, F. & Géribaldi, S. Self-assembled monolayers of semifluorinated thiols on electrochemically modified polycrystalline nickel surfaces. *Thin Solid Films* **491**, 253-259, doi:http://dx.doi.org/10.1016/j.tsf.2005.06.090 (2005).

88 Liu, S.-G., Liu, Y.-Q. & Zhu, D.-B. A study on the electrical switching mechanism in [TBA]x[Ni(dmid)2] thin film materials by XPS. *Synthetic Metals* **86**, 2265-2266, doi:10.1016/s0379-6779(97)81120-4 (1997).

89 Pan, Y. *et al.* Annealing induced electrical conductivity jump of multi-walled carbon nanotube/polypropylene composites and influence of molecular weight of polypropylene. *Journal of Polymer Science Part B: Polymer Physics* **48**, 2238-2247, doi:10.1002/polb.22106 (2010).

90 Jiang, F., Zhang, L., Jiang, Y., Lu, Y. & Wang, W. Effect of annealing treatment on the structure and properties of polyurethane/multiwalled carbon nanotube nanocomposites. *Journal of Applied Polymer Science* **126**, 845-852, doi:10.1002/app.36955 (2012).

91 Nandi, P. N., Deshpande, D. A. & Kher, V. G. Thermogravimetric analysis of hexa- and heptahydrate crystals and packed powder of nickel sulfate. *Thermochimica Acta* **32**, 143-149, doi:https://doi.org/10.1016/0040-6031(79)85102-3 (1979).

92 Hall, D. S., Lockwood, D. J., Bock, C. & MacDougall, B. R. Nickel hydroxides and related materials: a review of their structures, synthesis and properties. *Proceedings of the Royal Society A: Mathematical, Physical and Engineering Science* **471** (2015).

93 Uzelac, E. J. & Rasmussen, S. C. Thiophene-Extended Nickel Thiazoledithiolene: π-Extended Fused-Ring Metal Dithiolenes with Stabilized Frontier Orbitals. *European Journal of Inorganic Chemistry* **2017**, 3878-3883, doi:10.1002/ejic.201700702 (2017).

94 Tomaszewicz, E. & Kotfica, M. Mechanism and kinetics of thermal decomposition of nickel(II) sulfate(VI) hexahydrate. *Journal of Thermal Analysis and Calorimetry* **77**, 25-31, doi:10.1023/B:JTAN.0000033184.32714.7f (2004).

95 Wolfe, R. M. W., Menon, A. K., Marder, S. R., Reynolds, J. R., Yee, S. K. . Simultaneous Enhancement in Thermoelectric Properties of NiETT Films by Annealing. *Submitted* (2018).

96 Matienzo, J., Yin, L. I., Grim, S. O. & Swartz, W. E. X-ray photoelectron spectroscopy of nickel compounds. *Inorganic Chemistry* **12**, 2762-2769, doi:10.1021/ic50130a005 (1973).

97 Nesbitt, H. W., Legrand, D. & Bancroft, G. M. Interpretation of Ni2p XPS spectra of Ni conductors and Ni insulators. *Physics and Chemistry of Minerals* **27**, 357-366, doi:10.1007/s002690050265 (2000).

98 Matienzo, L. J., Swartz, W. E. & Grim, S. O. X-ray photoelectron spectroscopy of tetrahedral and square planar nickel(II) compounds. *Inorganic and Nuclear Chemistry Letters* **8**, 1085-1091, doi:https://doi.org/10.1016/0020-1650(72)80198-3 (1972).

99 Stickle, W. F., Reynolds, J. R. & Jolly, C. A. Surface characterization of electrically conducting nickel tetrathiooxalate/poly(vinyl alcohol) composites. *Langmuir* **7**, 2460-2463, doi:10.1021/la00059a011 (1991).

100 Sun, S., Wu, P., Zhu, D., Ma, Z. & Shi, N. Synthesis, electrical properties of [Ni(dmit)2]− complexes and X-ray crystal structure of [EDA][Ni(dmit)2] (dmit = 1,3-dithiol-2-thione-4,5-dithiolate). *Inorganica Chimica Acta* **268**, 103-107, doi:https://doi.org/10.1016/S0020-1693(97)05728-9 (1998).

101 Menon, A. K., Wolfe, R. M. W., Marder, S. R., Reynolds, J. R., Yee, S. K. Systematic Power Factor Enhancement in n-type NiETT/PVDF Composite Films. *Submitted* (2018).

102 Bergman, D. J. & Levy, O. Thermoelectric properties of a composite medium. *Journal of Applied Physics* **70**, 6821-6833, doi:10.1063/1.349830 (1991).

103 Søndergaard, R. R., Hösel, M., Espinosa, N., Jørgensen, M. & Krebs, F. C. Practical evaluation of organic polymer thermoelectrics by large-area R2R processing on flexible substrates. *Energy Science & Engineering* **1**, 81-88, doi:10.1002/ese3.8 (2013).

104 Wei, Q., Mukaida, M., Kirihara, K., Naitoh, Y. & Ishida, T. Polymer thermoelectric modules screen-printed on paper. *RSC Advances* **4**, 28802-28806, doi:10.1039/C4RA04946B (2014).

105 Menon, A. K. & Yee, S. K. Design of a polymer thermoelectric generator using radial architecture. *Journal of Applied Physics* **119**, 055501, doi:10.1063/1.4941101 (2016).

106 Menon, A. K., Meek, O., Eng, A. J. & Yee, S. K. Radial thermoelectric generator fabricated from n- and p-type conducting polymers. *Journal of Applied Polymer Science* **134**, 44060, doi:10.1002/app.44060 (2017).

107 Yee, S. K., LeBlanc, S., Goodson, K. E. & Dames, C. $ per W metrics for thermoelectric power generation: beyond ZT. *Energy & Environmental Science* **6**, 2561-2571, doi:10.1039/C3EE41504J (2013).

108 Gao, M. & Rowe, D. M. Ring-structured thermoelectric module. *Semiconductor Science and Technology* **22**, 880 (2007).

109 Boniche, I. & Arnold, D. P. Micromachined Radial Thermoelectric Modules for Power Generation Using Hot Gas Streams. *Microelectromechanical Systems, Journal of* **20**, 512-521, doi:10.1109/JMEMS.2011.2112336 (2011).

110 Angrist, S. *Direct Energy Conversion*. (Allyn and Bacon, Inc., 1965).

111 LeBlanc, S., Yee, S. K., Scullin, M. L., Dames, C. & Goodson, K. E. Material and manufacturing cost considerations for thermoelectrics. *Renewable and Sustainable Energy Reviews* **32**, 313-327, doi:http://dx.doi.org/10.1016/j.rser.2013.12.030 (2014).

112 Chen, G. Theoretical efficiency of solar thermoelectric energy generators. *Journal of Applied Physics* **109**, 104908, doi:http://dx.doi.org/10.1063/1.3583182 (2011).

113 Yazawa, K. & Shakouri, A. Optimization of power and efficiency of thermoelectric devices with asymmetric thermal contacts. *Journal of Applied Physics* **111**, 024509, doi:http://dx.doi.org/10.1063/1.3679544 (2012).

114 Heikes, R. R. & Ure, R. W. *Thermoelectricity: science and engineering*. (Interscience Publishers, 1961).

115 Incropera, F., DeWitt, D., Bergman, T. & Lavine, A. *Fundamentals of Heat and Mass Transfer*. (John Wiley & Sons, 2006).

116 Mayer, P. M. & Ram, R. J. Optimization of Heat Sink–Limited Thermoelectric Generators. *Nanoscale and Microscale Thermophysical Engineering* **10**, 143-155, doi:10.1080/10893950600643063 (2006).

117 Baranowski, L. L., Jeffrey Snyder, G. & Toberer, E. S. Effective thermal conductivity in thermoelectric materials. *Journal of Applied Physics* **113**, 204904, doi:http://dx.doi.org/10.1063/1.4807314 (2013).

118 Zhou, Z. G., Zhu, D. S., Huang, Y. S. & Wang, C. Heat Sink Matching for Thermoelectric Generator. *Advanced Materials Research* **383-390**, 6122-6127, doi:10.4028/www.scientific.net/AMR.383-390.6122 (2012).

119 Thermacore. <http://www.thermacore.com/products/copper-water.aspx> (

120 Kim, S. J., We, J. H. & Cho, B. J. A wearable thermoelectric generator fabricated on a glass fabric. *Energy & Environmental Science* **7**, 1959-1965, doi:10.1039/C4EE00242C (2014).

121 Jiang, Q. *et al.* Paper: An effective substrate for the enhancement of thermoelectric properties in PEDOT:PSS. *Journal of Polymer Science Part B: Polymer Physics* **52**, 737-742, doi:10.1002/polb.23482 (2014).

122 Yu, C., Murali, A., Choi, K. & Ryu, Y. Air-stable fabric thermoelectric modules made of N- and P-type carbon nanotubes. *Energy & Environmental Science* **5**, 9481-9486, doi:10.1039/C2EE22838F (2012).

123 Meng, C., Liu, C. & Fan, S. A Promising Approach to Enhanced Thermoelectric Properties Using Carbon Nanotube Networks. *Advanced Materials* **22**, 535-539, doi:10.1002/adma.200902221 (2010).

124 Menon, A. K. & Yee, S. K. in *ASME 2015 International Mechanical Engineering Congress & Exposition.* (ASME).

125 Bahk, J.-H., Fang, H., Yazawa, K. & Shakouri, A. Flexible thermoelectric materials and device optimization for wearable energy harvesting. *Journal of Materials Chemistry C* **3**, 10362-10374, doi:10.1039/C5TC01644D (2015).

126 Leonov, V. in *Wearable Monitoring Systems* 27-49 (Springer, 2011).

127 Torfs, T., Leonov, V. & Vullers, R. Pulse oximeter fully powered by human body heat. *Sens. Transducers J* **80**, 1230-1238 (2007).

128 Vullers, R., van Schaijk, R., Doms, I., Van Hoof, C. & Mertens, R. Micropower energy harvesting. *Solid-State Electronics* **53**, 684-693 (2009).

129 Navone, C., Soulier, M., Plissonnier, M. & Seiler, A. Development of (Bi, Sb) 2 (Te, Se) 3-based thermoelectric modules by a screen-printing process. *Journal of electronic materials* **39**, 1755-1759 (2010).

130 We, J. H., Kim, S. J. & Cho, B. J. Hybrid composite of screen-printed inorganic thermoelectric film and organic conducting polymer for flexible thermoelectric power generator. *Energy* **73**, 506-512 (2014).

131 Cao, Z., Koukharenko, E., Tudor, M., Torah, R. & Beeby, S. in *Journal of Physics: Conference Series.* 012031 (IOP Publishing).

132 Suemori, K., Hoshino, S. & Kamata, T. Flexible and lightweight thermoelectric generators composed of carbon nanotube–polystyrene composites printed on film substrate. *Applied Physics Letters* **103**, 153902 (2013).

133 Cao, Z., Koukharenko, E., Torah, R., Tudor, J. & Beeby, S. in *Journal of Physics: Conference Series.* 012016 (IOP Publishing).

134 Kim, M. K. *et al.* in *2013 Transducers & Eurosensors XXVII: The 17th International Conference on Solid-State Sensors, Actuators and Microsystems (TRANSDUCERS & EUROSENSORS XXVII).* 1376-1379 (IEEE).

135 Lu, Z. *et al.* Fabrication of flexible thermoelectric thin film devices by inkjet printing. *Small* **10**, 3551-3554 (2014).

136 Drahi, E., Gupta, A., Blayac, S., Saunier, S. & Benaben, P. Characterization of sintered inkjet-printed silicon nanoparticle thin films for thermoelectric devices. *physica status solidi (a)* **211**, 1301-1307 (2014).

137 Madan, D. *et al.* Enhanced performance of dispenser printed MA n-type Bi2te3 composite thermoelectric generators. *ACS applied materials & interfaces* **4**, 6117-6124 (2012).

138 Madan, D. *et al.* Dispenser printed circular thermoelectric devices using Bi and Bi0.5Sb1.5Te3. *Applied Physics Letters* **104**, 013902 (2014).

139 Madan, D., Wang, Z., Chen, A., Wright, P. K. & Evans, J. W. High-Performance Dispenser Printed MA p-Type Bi0. 5Sb1. 5Te3 Flexible Thermoelectric Generators for Powering Wireless Sensor Networks. *ACS applied materials & interfaces* **5**, 11872-11876 (2013).

140 Gao, M., Li, L. & Song, Y. Inkjet printing wearable electronic devices. *Journal of Materials Chemistry C* **5**, 2971-2993 (2017).

141 Gordiz, K., Menon, A. K. & Yee, S. K. Interconnect patterns for printed organic thermoelectric devices with large fill factors. *Journal of Applied Physics* **122**, 124507, doi:10.1063/1.4989589 (2017).

142 Jo, S., Kim, M., Kim, M. & Kim, Y. Flexible thermoelectric generator for human body heat energy harvesting. *Electronics letters* **48**, 1013-1015 (2012).

143 Sevilla, G. A. T., Inayat, S. B., Rojas, J. P., Hussain, A. M. & Hussain, M. M. Flexible and Semi-Transparent Thermoelectric Energy Harvesters from Low Cost Bulk Silicon (100). *Small* **9**, 3916-3921 (2013).

144 Orrill, M. & LeBlanc, S. Printed thermoelectric materials and devices: Fabrication techniques, advantages, and challenges. *Journal of Applied Polymer Science* **134**, 44256 (2016).

145 Koplow, M., Chen, A., Steingart, D., Wright, P. K. & Evans, J. W. in *Medical Devices and Biosensors, 2008. ISSS-MDBS 2008. 5th International Summer School and Symposium on.* 322-325 (IEEE).

146 Watkins, C., Shen, B. & Venkatasubramanian, R. in *ICT 2005. 24th International Conference on Thermoelectrics, 2005.* 265-267 (IEEE).

147 Fan, J. A. *et al.* Fractal design concepts for stretchable electronics. *Nature communications* **5** (2014).

148 Yazawa, K. & Shakouri, A. Cost-Efficiency Trade-off and the Design of Thermoelectric Power Generators. *Environmental Science & Technology* **45**, 7548-7553, doi:10.1021/es2005418 (2011).

149 Moon, B., Jagadish, H. V., Faloutsos, C. & Saltz, J. H. Analysis of the clustering properties of the Hilbert space-filling curve. *IEEE Transactions on knowledge and data engineering* **13**, 124-141 (2001).

150 Ankireddy, K. *et al.* Electrical Conductivity, Thermal Behavior, and Seebeck Coefficient of Conductive Films for Printed Thermoelectric Energy Harvesting Systems. *Journal of Electronic Materials* **45**, 5561-5569, doi:10.1007/s11664-016-4780-2 (2016).